Notch-dependent and -independent transcription are modulated by tissue movements at gastrulation

Julia Falo-Sanjuan[1], Sarah J. Bray[1]*,

1 Department of Physiology, Development and Neuroscience, University of Cambridge, Downing Street, Cambridge CB2 3DY, UK

* Correspondence: sjb32@cam.ac.uk

Abstract

Cells sense and integrate external information from diverse sources that include mechanical cues. Shaping of tissues during development may thus require coordination between mechanical forces from morphogenesis and cell-cell signalling to confer appropriate changes in gene expression. By live-imaging Notch-induced transcription in real time we have discovered that morphogenetic movements during *Drosophila* gastrulation bring about an increase in activity-levels of a Notch responsive enhancer. Mutations that disrupt the timing of gastrulation resulted in concomitant delays in transcription up-regulation that correlated with the start of mesoderm invagination. As a similar gastrulation-induced effect was detected when transcription was elicited by the

intracellular domain NICD, it cannot be attributed to forces exerted on Notch receptor activation. A Notch independent *vnd* enhancer also exhibited a modest gastrulation-induced activity increase in the same stripe of cells. Together, these observations argue that gastrulation-associated forces act on the nucleus to modulate transcription levels. This regulation was uncoupled when the complex linking the nucleoskeleton and cytoskeleton (LINC) was disrupted, indicating a likely conduit. We propose that the coupling between tissue level mechanics, arising from gastrulation, and enhancer activity represents a general mechanism for ensuring correct tissue specification during development and that Notch dependent enhancers are highly sensitive to this regulation.

Introduction

Cells continuously sense and respond to their environment. This occurs via signalling pathways that detect and respond to external stimuli, such as morphogen gradients or direct cell-surface ligands. During development, information routed through these pathways feeds into networks of transcription factors that coordinate cell fates to pattern and regulate differentiation. At the same time, cells are exposed to mechanical forces from changes in tissue movements, deformations and stiffness. In order for tissues to develop and function correctly, there must be mechanisms that couple cell signaling with the mechanical environment. Indeed, there is evidence that changes in cell morphology can impact on gene expression ***(Alam et al. 2016; Guilluy et al. 2014)***, but this has been little explored in the context of developmental signaling.

Notch is a key developmental signalling pathway that transmits information between cells in contact. Prior to ligand binding, the ADAM10 cleavage site in Notch is hidden by the negative regulatory region (NRR). To reveal this site, ligand binding exerts a force on the receptor, leading to a displacement of the NRR ***(Gordon et al. 2007; Gordon et al. 2015)***. A second cleavage by γ-secretase then releases the intracellular domain, NICD, which forms a complex with a DNA-binding transcription factor and a co-activator to regulate transcription of target genes. In many developmental processes, Notch activation occurs contemporaneously with morphological changes which could modulate pathway activity so that signaling and tissue rearrangements are coordinated

(Paolini et al. 2021; Han et al. 2021; Engel-Pizcueta and Pujades 2021; Lloyd-Lewis et al. 2019). For example, cell shape or tension changes in the neighbouring cells could impact on the forces exerted on the receptor to alter the amount of cleavage *(Shaya et al. 2017).* Alternatively, mechanical forces could alter the transcriptional output from Notch activation, by changing transport through nuclear pores or altering chromatin compaction *(Boumendil et al. 2019; Gozalo et al. 2020).*

To distinguish whether morphological events exert an influence on signaling, it is important to monitor the outputs in real-time when the changes are occurring. We have been investigating the onset of Notch activity in the *Drosophila* embryo using the MS2-MCP system to monitor the transcriptional response live. Notch activity initiates in a stripe of cells flanking the mesoderm, the mesectoderm (MSE), in the last cycle prior to gastrulation (nuclear cycle 14, nc14), and remains active throughout gastrulation. These cells divide after gastrulation, change their polarity and form a boundary that separates the flanking neuroectoderm *(Yu et al. 2021).* They subsequently form the midline of the central nervous system, giving rise to specific neuronal and glial progeny *(Wheeler et al. 2008)* under the control of the Notch regulated *single-minded* gene, which is essential for cell division after gastrulation, acquisition of their midline fate and proper axonal connectivity *(Nambu et al. 1990; Nambu et al. 1991; Hummel et al. 1999).* Defects in the establishment of the mesectoderm boundary result in mixing of the left and right neuroectoderm as well as later effects on midline development *(Yu et al. 2021).* A notable feature of the transcriptional profiles from two Notch-responsive enhancers, *sim* and *m5/m8*, is that they undergo a transition approximately 50 min into nc14, when transcription levels increase approximately two-fold *(Falo-Sanjuan et al. 2019).* This transition occurs as the embryo undergoes gastrulation, making it plausible that mechanical forces or tissue reorganization at this stage are responsible for the increase in transcription, and may contribute to the integrity of boundary formation *(*Numbu1990*; Yu et al. 2021).*

Gastrulation initiates towards the end of nc14, approximately 3h post fertilization. During this process, the apical surface of the most ventral subset of mesoderm (ME) cells constricts and cells shorten along their apico-basal axis *(Leptin and Grunewald*

1990; Sweeton et al. 1991). This occurs in response to apical re-localization of Myosin II (MyoII), which is controlled by a GPCR (G-Protein Coupled Receptor) cascade *(Sweeton et al. 1991; Manning et al. 2013; Parks and Wieschaus 1991; Barrett et al. 1997; Kolsch et al. 2007; Dawes-Hoang et al. 2005).* As a consequence, the 'ventral furrow' is formed, which invaginates bringing the remainder of the mesoderm cells with it *(Leptin and Grunewald 1990; Sweeton et al. 1991).* Studies of the forces generated indicate that, although the force to invaginate the furrow is produced autonomously in the mesoderm by pulses of acto-myosin contractions *(Martin et al. 2009),* the mechanical properties of tissues adjacent to it, such as the MSE and neuroectoderm (NE), also change and may be important to allow invagination to occur *(Rauzi et al. 2015).*

We set out to investigate whether there is a causal relationship between morphological events occurring at gastrulation and the change in levels of Notch dependent transcription, using live imaging. Strikingly, we found a strong correlation between the start of mesoderm invagination and the time at which transcription levels increased. This change in transcription was delayed or absent when gastrulation was perturbed using different genetic mutations and manipulations. A Notch independent enhancer exhibited similar, albeit more modest effect, suggesting that the mechanism involves a more general feature. Furthermore, the Notch intracellular fragment, NICD, was also subject to similar regulation. The results indicate therefore that the mechanical context has a significant impact on the transcriptional outcome of Notch signaling but argue that this operates downstream of receptor activation and also affects other developmental enhancer(s). This type of coordination between tissue forces, developmental signalling and nuclear activity is thus likely to be of general importance for shaping tissues and organs as they form.

Results

Notch dependent transcription increases at gastrulation

During early *Drosophila* embryogenesis, Notch is active in the mesectoderm (MSE), a stripe of cells that border the mesoderm *(Nambu et al. 1990; Morel and*

Schweisguth 2000; Morel et al. 2003). Activity commences midway through nc14 and continues during gastrulation, persisting in most MSE cells until they divide to form the precursors of the midline *(Martín-Bermudo et al. 1995; Cowden and Levine 2002; Falo-Sanjuan et al. 2019).* Measuring transcription live, using the MS2 system, reveals that there is a striking increase in the mean levels of transcription produced by Notch responsive enhancers during gastrulation. This increase occurs approximately 20 minutes after transcription initiates, which corresponds to 50 min after the start of nuclear cycle 14 (nc14). At this point, the transcription levels from two distinct Notch responsive mesectodermal enhancers, *m5/m8* and *sim* *(Zinzen et al. 2006; Hong et al. 2013),* almost double in magnitude (Figure 1**AB**, *Falo-Sanjuan et al. 2019*). The change in magnitude occurs with different promoter combinations and with reporters inserted into different genomic positions (Figure 1 - supplement 1**AC**, *Falo-Sanjuan et al. 2019*), arguing it is a feature of the transcriptional response driven by the Notch responsive enhancers. However, there was no coordinated transition in levels when the profiles from all cells were aligned by activity onset in the MSE (Figure 1 - supplement 1**BD**), arguing that the increase is not dependent on the length of time that the enhancers have been active and thus may be related to a specific developmental event/time.

The observed increase in the mean transcriptional activity was not due to an increase in the number of active cells (Figure 1**D**), but rather to a change in the profiles within individual nuclei. This differed in magnitude from nucleus to nucleus. Thus, when *m5/m8* transcription profiles from individual nuclei were analyzed, a clear, circa 2-fold, transition in levels was detected in 30-45% of the MSE nuclei (Figure 1**C**). Others did not show such a major increase in levels, but several still manifest an inflection in the bursting at the equivalent time (Figure 1**C**).

The transition in levels occurs whilst the embryo undergoes gastrulation (**Video 1**), a process that starts midway through nc14 and lasts approximately 20 min. Gastrulation begins when the most ventral mesodermal cells constrict their apical surface to initiate ME invagination and results in the convergence of the two MSE stripes at the midline (Figure 1**GF**, *Leptin and Grunewald 1990; Sweeton et al. 1991.* Given the

large scale morphogenetic movements involved, it is possible that these influence the transcriptional activity. We therefore asked whether any of the changes that take place at gastrulation are correlated with the transition in transcription from the Notch responsive enhancers, by analyzing all the time-course data previously obtained from Notch responsive reporters (combining different enhancers, promoters and landing sites, n = 56 videos, ***Falo-Sanjuan et al. 2019***). On an embryo-by-embryo basis, we examined the relationship between the transcription transition-point and three different features during gastrulation: start of apical constriction, start of mesoderm invagination (defined as when mesectoderm cells first start to move ventrally) and the end of gastrulation (when all mesoderm cells have invaginated). Of the three, the highest correlation (both in terms of R^2 and both events occurring at similar timepoints) was with the start of mesoderm invagination (Figure 1**G**). This increase was not due to changes in the Z position of the nuclei that occurred during this period. The extent of nuclear movement with respect to the plane of imaging depends on the precise orientation of the embryo. Taking advantage of this variation between embryos, we measured the change in Z position for each in relation to the fold increase in transcription levels and found no correlation (R^2 coefficient of 0, Figure 1 - supplement 1**E**). Nevertheless, because there is a temporal correlation with gastrulation, a plausible model is that the tissue level morphogenetic movements from gastrulation are responsible for the increase in transcription levels.

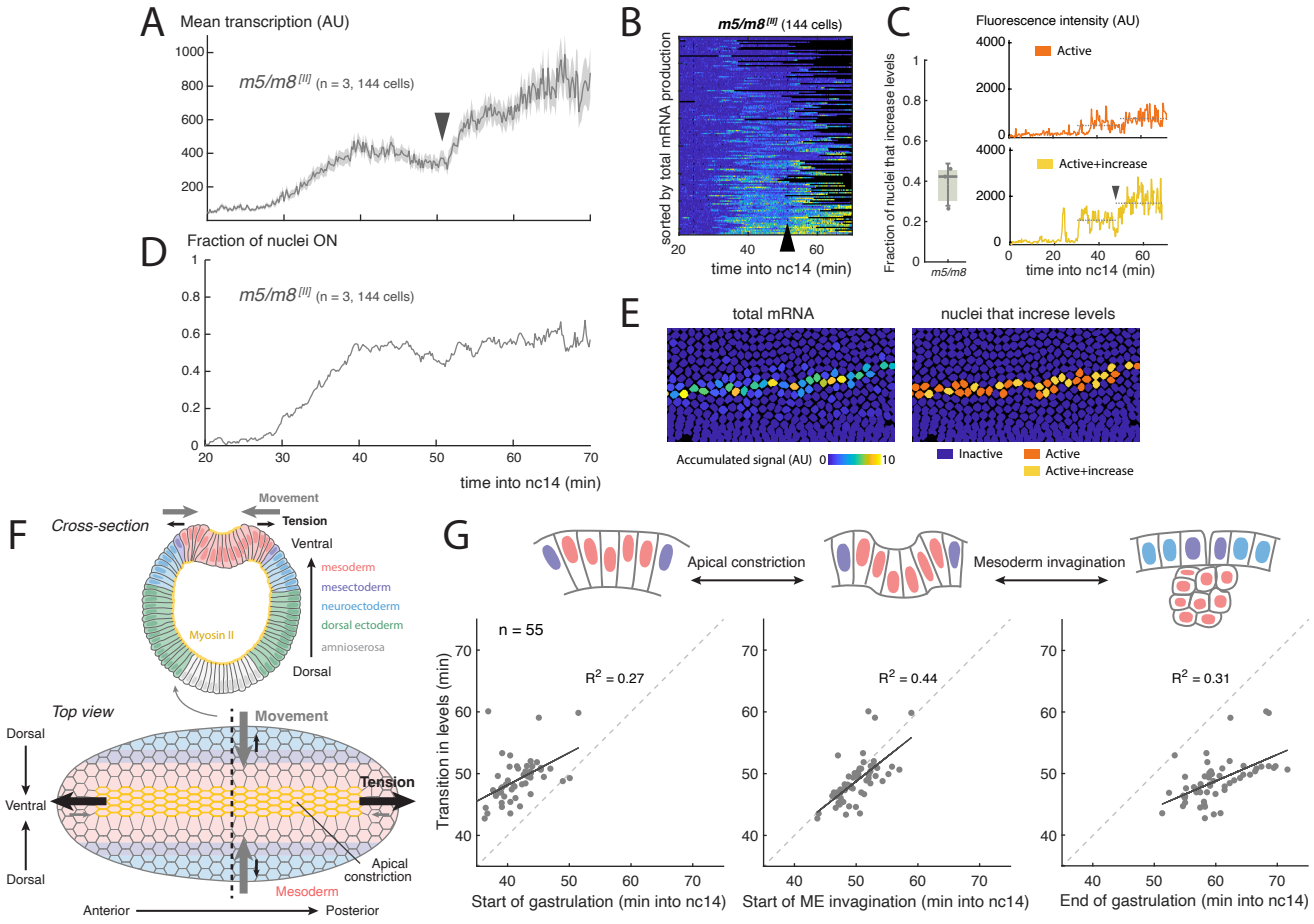

Figure 1. Increase in Notch-dependent transcription occurs at gastrulation. A) Mean profile of activity of the Notch responsive *m5/m8 [II]* enhancer during nc14. **B**) Heatmap showing *m5/m8 [II]* activity in all MSE cells over time, arrowhead indicates the transition point. **C**) Proportion of active cells in each embryo that increase levels of *m5/m8 [II]* transcription at gastrulation (left; median, Q1/Q3 and SD shown) and examples of individual *m5/m8 [II]* transcription traces with ~2x increase (yellow) or inflection only (orange). Dotted lines indicate mean transcription levels in the 15 minutes before and after gastrulation. **D**) Fraction of tracked nuclei that are actively transcribing during nc14. **E**) Still frame showing tracked nuclei color-coded for the total transcription produced by each nuclei (left) and by whether they exhibit ~2x increase in levels (right). **F**) Schematic drawing of the forces generated during gastrulation. A cross-section with the different regions along the dorso-ventral axis (top) and top view from the ventral side (bottom) are shown. The most ventral part of the mesoderm (red-shaded) localizes Myosin II (yellow) apically, which generates apical constrictions and leads to tension generated towards the anterior and posterior ends of the embryo, producing ventral movement from the mesoderm, mesectoderm and neuroectoderm cells. **G**) Correlation between the time at which mean levels of transcription increase in an embryo and the timing of 3 events during gastrulation. Each dot indicates an embryo from a collection of different Notch responsive enhancers, promoters and landing sites (n = 55 videos). Panels **A**-**G** were obtained by re-analyzing data from *Falo-Sanjuan et al. 2019.* Panel **F** has been adapted from Figure 6B from *Martin 2020* and Figure 1 from *Leptin 1999.*

Events at gastrulation modulate Notch dependent transcription

To investigate whether morphological changes at gastrulation bring about the transition in Notch dependent transcription, we used a combination of approaches to disrupt gastrulation while live-imaging transcription from *m5/m8* $^{[II]}$, an insertion of the reporter on the second chromosome that responds robustly to Notch activity ***(Falo-Sanjuan et al. 2019).*** Gastrulation is coordinated by a signalling cascade that controls Myosin contractility, which in turn produces apical constriction of mesoderm cells to drive invagination (Figure 2**A**) ***(Dawes-Hoang et al. 2005; Kolsch et al. 2007).*** First, we performed germline RNAi knockdowns (KD) to eliminate maternally-encoded proteins that act in the signaling cascade, namely α-Catenin (α-Cat), a key component of Adherens Junctions (AJ), Concertina (Cta) and RhoGEF2, which are the Gα and GEF (Guanine nucleotide Exchange Factor) of the signaling cascade ***(Parks and Wieschaus 1991; Barrett et al. 1997)*** (Figure 2**A**). Apical relocalization of Armadillo (an AJ component) and RhoGEF2 is required for gastrulation ***(Kolsch et al. 2007)*** and Armadillo is required for apical myosin relocalization ***(Dawes-Hoang et al. 2005).*** We used *α-Cat RNAi* rather than *Arm RNAi* because it produced a much stronger KD. RNAi depletion produced morphological phenotypes consistent with those previously described, except in the case of RhoGEF2 ***(Parks and Wieschaus 1991; Barrett et al. 1997; Dawes-Hoang et al. 2005),*** where the depleted embryos were viable and lacked obvious gross morphological defects, such as extra folds, suggesting a lower knock-down efficiency (Figure 2 - supplement 1**A**).

Of the three tested, α-Cat KD led to the most severe disruption of gastrulation, mesoderm cells failed to invaginate and divided externally (Figure 2 - supplement 1**ABC**, **Video 2**). Strikingly, no increase in *m5/m8* $^{[II]}$-directed transcription occurred in these embryos. Instead, the mean levels decreased after the initial activation, at the time when the increase in levels normally occurs, and then plateaued at a lower level (Figure 2**B**, Figure 2 - supplement 2**B**). This was because few individual nuclei exhibited any increase in levels in these embryos (Figure 2 - supplement 2**A**). Other reporters that also exhibited increased levels during gastrulation, namely *sim* $^{[II]}$ and *m5/m8* $^{[III]}$, were similarly affected by α-Cat depletion (Figure 2 - supplement 3) We

note the mean levels of transcription from *m5/m8* [II] reporter were not significantly reduced prior to gastrulation by α-Cat depletion, unlike those from *m5/m8* [III] and the endogenous *E(spl)m8-HLH* gene that both showed decreased levels also during cellularization ***(Falo-Sanjuan and Bray 2021)***. The difference likely arises because this *m5/m8* [II] insertion achieves maximal transcription at lower levels of Notch activity, based on its response in different contexts, and that α-Cat depletion reduces, but does not fully compromise, Notch activity ***(Falo-Sanjuan and Bray 2021)***.

Depletion of either Cta or RhoGEF2 resulted in a slowing of gastrulation. Cta depletion also caused variable delays in the start of mesoderm invagination (Figure 2 - supplement 1**BC**, **Video 3**). In neither genotype was there a normal increase in transcription at the time of gastrulation. The mean levels remained similar to those prior to gastrulation and, on an individual nucleus basis, very few exhibited any marked change in levels (Figure 2**D**, Figure 2 - supplement 2**CD**). Although there was no clear increase detected, the profiles retained an inflection point, when there was a transition between the early 'peak' levels and the later activity, manifest as a small dip in levels between the two phases. To assess whether this transition point was related to gastrulation events, the time when the transition occurred was plotted against the mile-stones for each embryo individually. The strongest correlation was with the start of mesoderm invagination (coefficient of $R^2 = 0.7$, Figure 2**C**), as it was for the increase in levels that occurs in wild-type embryos.

We next evaluated the consequences from mutations affecting the zygotically required gene *folded gastrulation* (*fog*), which encodes the ligand for the GPCR in the cascade regulating gastrulation ***(Costa et al. 1994; Dawes-Hoang et al. 2005)***. *fog*$^{-}$ hemizygous embryos exhibited a delayed start of mesoderm invagination and slowed gastrulation overall (Figure 2 - supplement 1**BC**, **Video 2**). In these embryos, levels of transcription increased, although less than in normal embryos (Figure 2**F**, Figure 2 - supplement 2**EF**). Notably, there was a significant 10 min delay in the time at which levels increased, from approximately 50 min to 60 min into nc14 (Figure 2**F**). This time-point also correlated well ($R^2 = 0.78$) with the start of mesoderm invagination when analyzed on an embryo-by embryo basis (Figure 2**E**), similar to the transition-point

in the RNAi depleted embryos.

We note other genetic manipulations that do not affect gastrulation do not alter the increase of *m5/m8* $^{[II]}$ activity at the time of gastrulation (Figure 2 - supplement 4), although some affect other features of the response, such as an overall reduction in mean levels. This further supports that the observed effects are specific to gastrulation and not an indirect consequence of the manipulations performed.

Based on these genetic experiments, the increase in Notch-dependent transcription levels is perturbed or delayed in conditions where gastrulation is blocked or slowed down. We hypothesize therefore that normal 'fast' gastrulation is required for the increase in levels and, since we observe a consistent correlation between the start of mesoderm invagination and the transition in transcription levels, it is likely that this is the causal step.

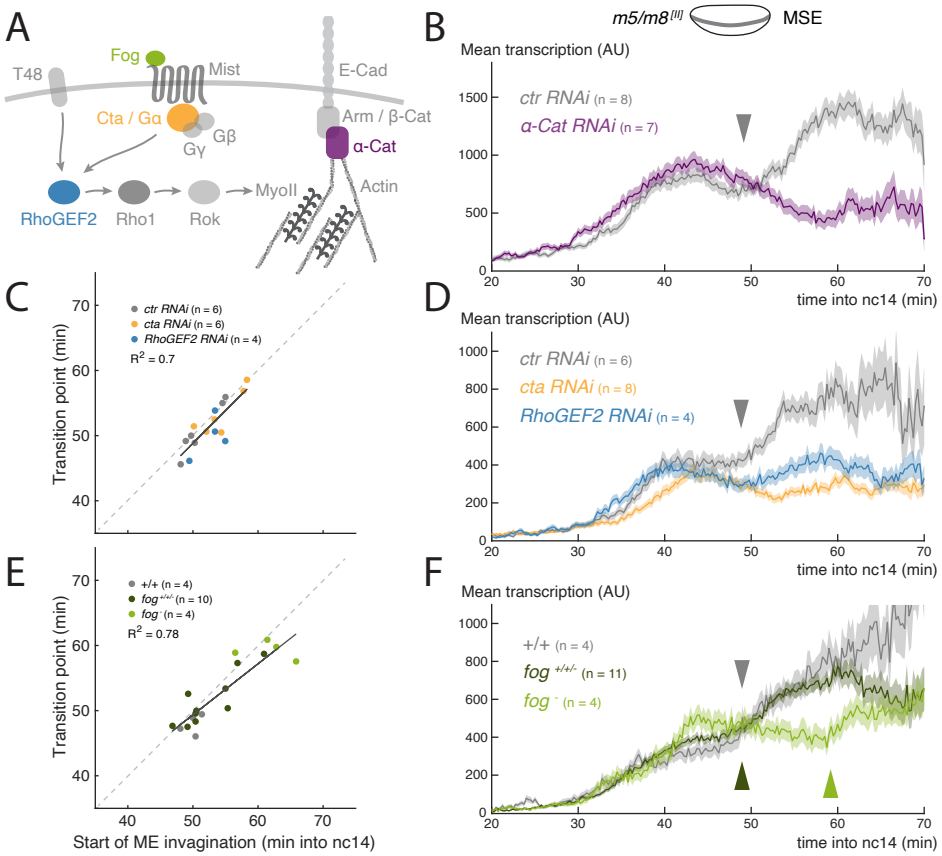

Figure 2. Disruption of gastrulation correlates with changes in the transition in Notch dependent transcription. **A**) Simplified scheme of the signalling cascade that controls MyoII contractility during *Drosophila* gastrulation. **B**) Mean profile of *m5/m8* [II] activity in *α-Cat* RNAi embryos compared to control embryos. **C**) Correlation between the start of invagination and transition in levels of transcription in each embryo, in *cta*, *RhoGEF2* and control RNAi embryos. **D**) Mean profile of *m5/m8* [II] activity in *cta*, *RhoGEF2* and control RNAi embryos. **E**) Correlation between the start of invagination and transition in levels of transcription in each embryo, in *fog* mutant embryos compared to control embryos and other non *fog* hemizygous embryos obtained from the same cross. **F**) Mean profile of *m5/m8* activity in *fog* mutant embryos compared to control embryos and other non *fog* hemizygous embryos obtained from the same cross. The transition in levels is delayed approximately 10 min in *fog* mutants (arrowheads). Mean transcription profiles show mean and SEM (shaded area) of MS2 fluorescent traces from all cells combined from multiple embryos (n embryo numbers indicated in each). R^2 coefficients are calculated after pooling all points shown the same plot together. The transition point was only considered when a clear change in mean levels of transcription in an individual embryo could be observed, therefore the number of points in **C** and **E** could be smaller than the total number of embryos collected for each condition.

Gastrulation also modulates Notch independent transcription

There are several different types of mechanisms that could explain a causal link between gastrulation and Notch-dependent transcription levels. As Notch activation involves a pulling force from Delta in adjacent cells *(Gordon et al. 2015)*, one model is that increased cell surface tensions from the morphogenetic movements at

gastrulation lead to increased Notch cleavage and NICD release. An alternative model is that the forces bring about a change in nuclear properties that consequently impact on transcription. For example, these could include changes in nuclear import, chromatin reorganization or chromatin mobility.

To distinguish these possibilities we took two approaches. First, we generated a transcriptional reporter using a Notch-independent enhancer from the *ventral nervous system defective* (*vnd*) gene. Unlike many of the other embryonic enhancers studied to date, the *vnd early embryonic enhancer* (*vndEEE*) is reported to be active throughout nc14 and to drive expression in a band of cells that overlap the MSE ***(Stathopoulos et al. 2002)***. As predicted, a new MS2 reporter containing this enhancer, referred to here as *vnd*, was active from the beginning of nc14 throughout gastrulation and recapitulated the spatial pattern of *vnd* (**Video 4**). After a peak of transcription at the start of nc14, the mean levels of *vnd* transcription from all the active nuclei exhibited no increase in levels at gastrulation. Indeed, the overall mean decreased at this time. However, when the nuclei were separated according to their expression domain, an increase in mean levels was detectable specifically in MSE nuclei at around 50 min into nc14, similar to the *m5/m8* enhancer (Figure 3**A**). No increase was detected in the other, NE domain (Figure 3**B**). The proportion of nuclei that exhibited a clear increase in levels when considered individually was, however, considerably lower than for *m5/m8* (16% of MSE nuclei and 2% of NE nuclei, Figure 3**C**). These results suggest that the activity of Notch independent as well as Notch dependent enhancers are affected at the time of gastrulation, albeit the effect is more modest for Notch independent activity, and that this property is limited to the mesectodermal cells.

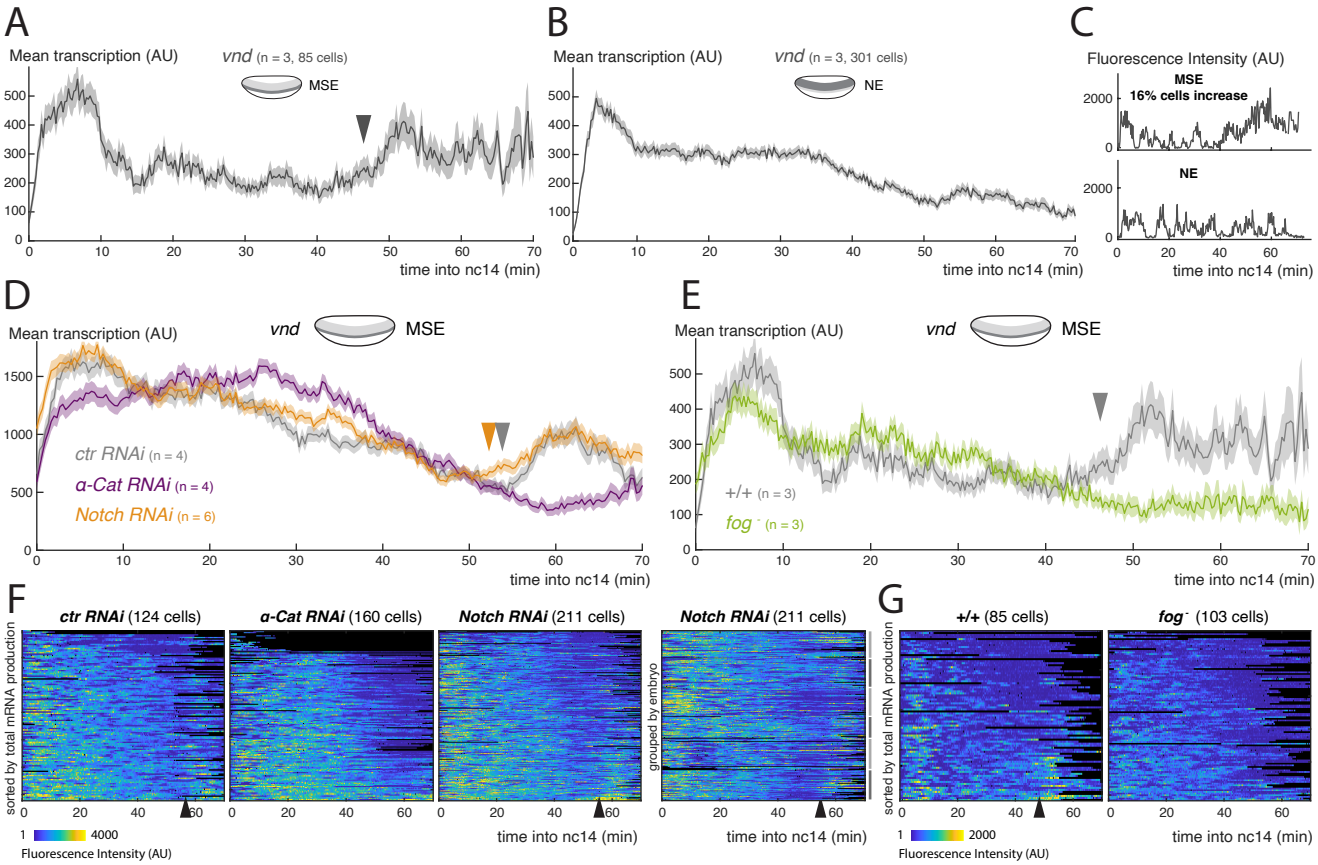

Figure 3. Activity of the Notch-independent *vnd* enhancer is modulated by gastrulation. **A**) Mean profile of transcription from *vnd* in MSE nuclei. **B**) Mean profile of transcription of *vnd* in NE nuclei. **C**) Examples of *vnd* transcription traces from MSE and NE, with (upper) and without (lower) a marked increase at the time of gastrulation. **D**) Mean profile of transcription from *vnd* in MSE nuclei in *α-Cat* and *Notch* RNAi compared to control embryos. **E**) Mean profile of transcription from *vnd* in MSE nuclei in *fog* mutant embryos compared to control embryos. **F**) Heatmaps showing *vnd* activity in all MSE cells over time in *α-Cat*, *Notch* and control RNAi embryos, sorted by total mRNA production (first 3 plots) and *Notch* RNAi grouped by embryo. **G**) Heatmaps showing *vnd* activity in all MSE cells over time in *fog*$^-$ embryos compared to controls, sorted by total mRNA production. Mean transcription profiles show mean and SEM (shaded area) of MS2 fluorescent traces from all cells combined from multiple embryos (n embryo numbers indicated in each). Arrowheads indicate increase in the mean levels of transcription.

We next investigated whether the increase in *vnd* activity in MSE nuclei was also linked to gastrulation, by measuring transcription in α-Cat depleted and *fog* mutant embryos. Neither genotype showed an increase in transcription in MSE cells (Figure 3**D-G**), instead the levels remained at a plateau similar to that in the NE nuclei (Figure 3**B**). Thus it appears that *vnd* transcription in MSE nuclei is also augmented due to gastrulation, in a similar manner to *m5/m8*-directed transcription. As there is no evidence that *vnd* is regulated by Notch *(Markstein et al. 2004)*, this implies

that gastrulation exerts effects on transcription independent of any effects on Notch activation. To verify that the modulation of *vnd* is not Notch dependent, we used an RNAi line to deplete Notch levels. As predicted, this treatment greatly reduced transcription from *m5/m8* $^{[II]}$ (Figure 3 - supplement 1**AB**). In contrast, there was no change in the timing of either the transition or the increase in levels from the *vnd* enhancer in any of the *Notch RNAi* embryos (Figure 3**DF**). Together the results indicate that gastrulation also modulates the activity of a Notch independent *vnd* enhancer, suggesting that a general, rather than a Notch-specific, mechanism is involved.

Regulation of Notch dependent transcription by gastrulation occurs downstream of pathway activation

The results with the *vnd* enhancer suggest that the gastrulation-induced changes in *m5/m8* transcription do not arise from increased Notch cleavage. As a second approach to investigate at which level of the pathway this modulation occurs, we examined whether gastrulation exerted any effects on transcription levels when the intracellular fragment NICD was expressed ectopically. To do so, we used an *eve2* transgene to direct expression of NICD in an orthogonal stripe overlapping the MSE, which is sufficient to drive ectopic transcription from *m5/m8* ***(Kosman and Small 1997; Cowden and Levine 2002; Falo-Sanjuan et al. 2019).*** The mean profile of *m5/m8* $^{[II]}$ transcription in MSE nuclei that were exposed to NICD had two peaks, the first shortly after the onset of NICD expression and the second during gastrulation. The transition between the two, the 'trough', slightly preceded the onset of mesoderm invagination. Thus the second 'peak' was initiated at the start of mesoderm invagination, characteristic of the gastrulation-induced increase in transcription in normal conditions. As MSE nuclei will be exposed to endogenous Notch signalling as well as the ectopic NICD, we also examined the profiles in the bordering NE nuclei. These exhibited a similar trough in levels prior to gastrulation, although the subsequent activity did not achieve the same levels as in the MSE nuclei (Figure 4 - supplement 1**B**). Together, these data support the model that gastrulation has an effect on *m5/m8* transcription that is independent of any influence on Notch cleavage.

To further verify that gastrulation-dependent changes occur independent from Notch cleavage, we monitored the transition in transcription levels elicited by NICD in embryos where the endogenous Notch was depleted by RNAi. No transcription was detected outside the domain of the *eve2* stripe (Figure 4 - supplement 1**A**, **Video 5**), confirming that Notch depletion was successful. Strikingly, the MSE nuclei within the stripe where NICD was expressed exhibited the same profile of activity in the *Notch RNAi* depleted embryos to those from control embryos with intact Notch. In particular, the levels of transcription increased at the time of gastrulation and to the same degree (Figure 4**AC**). Thus, the transition in transcription levels at gastrulation occurs even in the absence of full length Notch, arguing the effects are downstream of receptor cleavage.

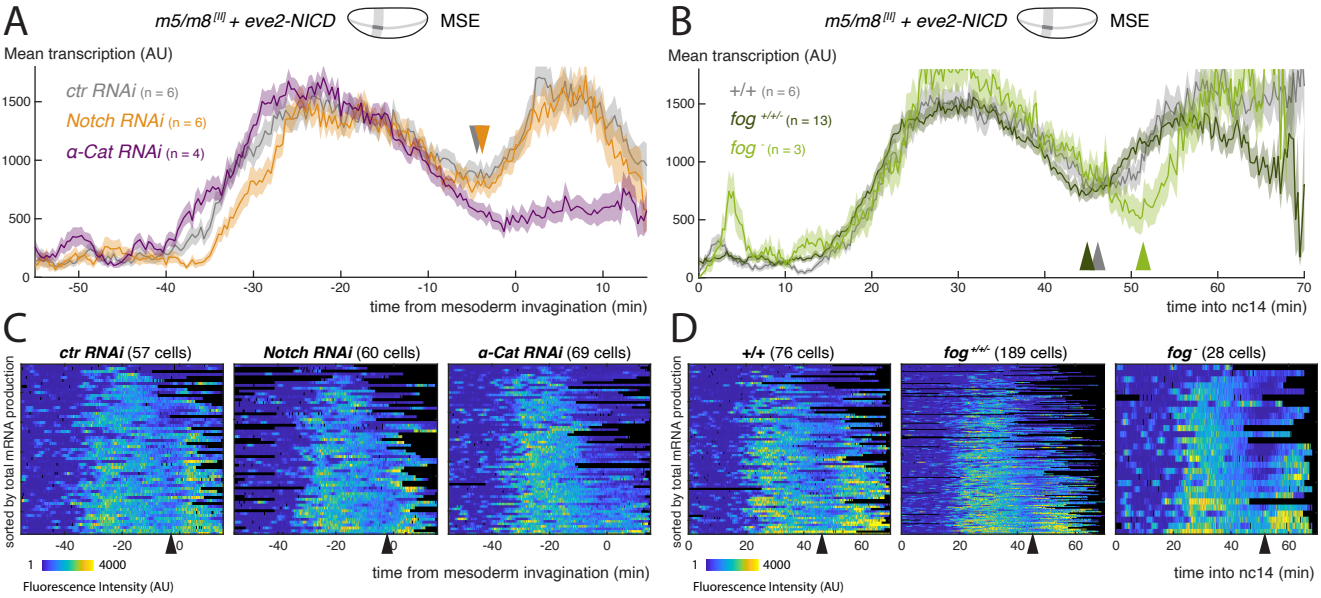

Figure 4. Modulation of Notch dependent transcription occurs downstream of pathway activation. **A**) Mean profile of transcription from *m5/m8* [II] in MSE nuclei, aligned by the time of ME invagination, in *α-Cat* and *Notch* RNAi compared to control embryos in the presence of ectopic NICD (produced by *eve2-NICD*). **B**) Mean profile of *m5/m8* [II] transcription in MSE nuclei with ectopic NICD in homozygous *fog* mutants compared to control or heterozygous embryos from the same cross (*fog*$^{+/+/-}$). **C**) Heatmaps showing *m5/m8* [II] activity in MSE cells within *eve2-NICD* domain, aligned by the time of ME invagination, in *α-Cat*, *Notch* and control RNAi embryos. **D**) Heatmaps showing *m5/m8* [II] activity in MSE cells within *eve2-NICD* domain over time in *fog*$^{-}$ embryos compared to control or heterozygous embryos obtained from the same cross (*fog*$^{+/+/-}$). Mean transcription profiles show mean and SEM (shaded area) of MS2 fluorescent traces from all cells combined from multiple embryos (n embryo numbers indicated in each). Arrowheads indicate an increase in the mean levels of transcription.

To investigate whether the transition in transcription that occurs in the presence of NICD is directly related to gastrulation, we examined it in embryos where gastrulation

was disrupted by α-Cat depletion or the *fog* allele, as above. In the α-Cat depleted embryos, where gastrulation was completely disrupted, there was no second 'peak' of transcription from *m5/m8* $^{[II]}$. Instead the levels remained at low levels from the time when mesoderm invagination would normally occur (Figure 4**AC**). *fog* mutant embryos, in which gastrulation was delayed and slowed down, retained a second peak of *m5/m8* $^{[II]}$ transcription, but its onset was delayed in both MSE and NE nuclei (Figure 4**BD**, Figure 4 - supplement 1**BC**). Notably, on an embryo by embryo basis, the delayed transition-point in the MSE correlated with the start of mesoderm invagination (R^2 coefficient of 0.62) (Figure 4 - supplement 1**D**).

Altogether, the results suggest that the mechanics of gastrulation have an input into transcription in the MSE, that brings about an increase in the levels of mRNA produced. Because the effects on the *m5/m8* enhancer are more marked than those on *vnd*, Notch-dependent processes may be more sensitive. Furthermore, the consequences are strongest in MSE cells, suggesting that gastrulation exerts differential impacts across the ectoderm, which might be related to the gradients of forces and cell deformation that have been measured ***(Fuse et al. 2013; Rauzi et al. 2015).*** Indeed, only a subset of mesectoderm cells exhibit a marked increase in transcription levels, suggesting there may be specific properties that are involved. We therefore re-analyzed videos from embryos expressing the cell membrane marker Gap43-mCherry and *m5/m8* $^{[II]}$ transcription ***(Falo-Sanjuan and Bray 2021),*** to track cell membranes over time and measure their properties (Figure 5 - supplement 1**A**, **Video 6**). We found no difference in the area of mesectodem cells that exhibited increased *m5/m8* $^{[II]}$ transcription compared to their neighbours where there was no marked increase (Figure 5 - supplement 1**B**) nor in the eccentricity or length of their contact with mesoderm cells. A feed-forward loop between mechanical forces and Fog has been previously described, which involves inhibition of Fog endocytosis and could also be affecting Notch signalling by regulation of endocytosis ***(Pouille et al. 2009).*** However, as the step-change in transcription is affected by the loss of Fog and α-Cat, and also affects *vnd* and NICD-dependent transcription, the mechanism appears to involve a step subsequent to the alteration of endocytosis.

Disruption of LINC complex alters the profile of *m5/m8* transcription

Amongst mechanisms that could be responsible for the gastrulation-related increase in transcriptional activity in MSE nuclei, one hypothesis is that forces from cell rearrangements are transmitted through the cytoskeleton to the nucleus via the Linker of Nucleoskeleton and Cytoskeleton (LINC) complex (Figure 5**A**, ***Crisp et al. 2006***). In several other contexts LINC is integral for transducing nuclear mechanical signals to confer changes in both gene expression and chromatin organization ***(Hamouda et al. 2020)***. We therefore set out to test the impact from disrupting components of the LINC complex on the transcription profile of *m5/m8* $^{[II]}$. Of the three conditions tested, only maternal knockdown of *klarsicht* (*klar*), which encodes a KASH protein, was successful, producing embryos with strongly reduced *klar* mRNA (Figure 5 - supplement 2**A**). Depletion of mRNA encoding SUN protein Klaroid (Koi) was unsuccessful and *Lamin C* mRNA knockdown produced no viable embryos. We therefore focused on the effects produced by *klar* mRNA depletion. Klar is known to influence lipid bodies in the embryo and *klar* mutant embryos are more transparent than controls ***(Supatto et al. 2009)***. Consistently, *klar RNAi* embryos exhibited higher fluorescent intensity signals (control embryos had 15.8% lower RFP and 11% lower GFP signals, Figure 5 - supplement 2**DE**). We thus compensated the quantified MS2 signal in *klar RNAi* embryos for increased clearing by 11% (Figure 5 - supplement 2**F**).

If the LINC complex was involved in transcription modulation, we would expect its disruption to result in similar flat transcription levels to those seen when gastrulation is perturbed. Indeed, Klar disruption did yield flatter levels of *m5/m8* $^{[II]}$ transcription. The early phase of transcription was slightly elevated and there was no subsequent transition or reduction in the late phase (Figure 5**B**, Figure 5 - supplement 2**B**). As there was no distinct transition at the time of mesoderm invagination, this suggests there is an uncoupling of the transcription profiles from the gastrulation movements caused by LINC complex disruption. However, as these embryos exhibited longer and less robust gastrulation (Figure 5**C**, Figure 5 - supplement 2**C**) it is not possible to fully rule out that the lack of a normal increase in transcription are the result of these indirect effects on gastrulation. Nevertheless, given the key role played by Klar in linking the

cytoskeleton to the nucleus, it is highly plausible that the change in profile from the *klar* mRNA knock-down occurs because the gastrulation movements have become uncoupled from transcription.

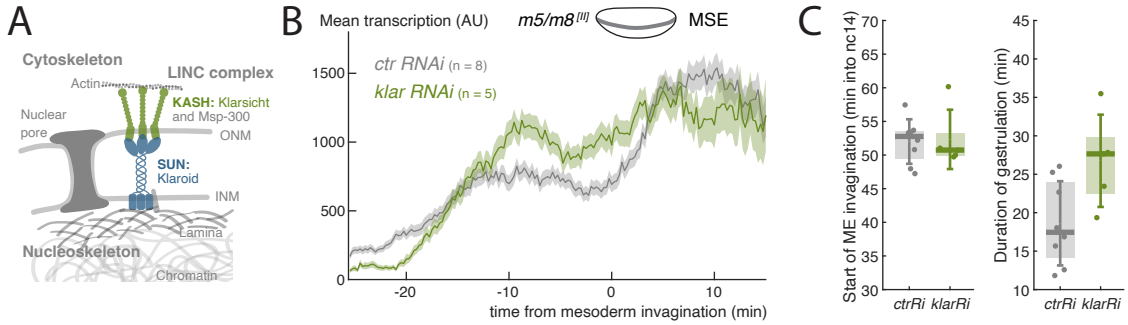

Figure 5. LINC complex disruption decouples gastrulation progression and changes in transcription. A) Scheme depicting LINC complex that connects cytoskeleton and nucleoskeleton, *Drosophila* KASH and SUN proteins Klarsicht and Klaroid are highlighted. **B**) Mean profile of transcription from *m5/m8* [II] in *klar* RNAi compared to control embryos. **C**) Onset of ME invagination (left) and duration of gastrulation in *klar* and control RNAi embryos. Boxplots show median, Q1/Q3 quartiles and SD. Control embryos are the same as shown in Figure 2**B** and Figure 2 - supplement 1**B**.

Changes in nuclear properties at gastrulation

We set out to explore mechanisms to explain how gastrulation alters transcription, via the LINC complex. We considered two possibilities. One is that it brings about a change in nuclear import properties, as has previously been reported *(Uzer et al. 2018; Jahed et al. 2016)*. This could involve a general change in nuclear import or a specific change in nuclear levels of key transcription factors including Twist, which is required for activity of both *m5/m8* and *vnd*. Indeed the levels of Twist are regulated by mechanical forces in some contexts *(Farge 2003; Desprat et al. 2008)*. A second possibility is that the force on the nucleus results in changes in chromatin compaction or accessibility, rendering the target loci more accessible to NICD complexes or to transcription machinery.

We first investigated whether there were any general changes in the nuclear import properties by analyzing the nuclear levels, and nuclear exclusion, of fluorescently-tagged molecules of different dimensions including fluorescently-tagged dextrans of two molecular weights (70kDa and 40kDa), as well as several tagged variants of GFP, with and without a nuclear localization signal (nls). None of these exhibited any change in

nuclear levels at the time of gastrulation, (Figure 6 - supplement 1**AB**), including 70kDa-FITC dextran which exhibited the highest nuclear exclusion (Figure 6 - supplement 1**A**), consistent with previous data ***(Hampoelz et al. 2016).*** Likewise, there were no gastrulation-related changes in nuclear levels of several core transcriptional regulators, including subunits of Mediator complex (Med4, Med17, Skd, Figure 6 - supplement 1**C**) and the histone acetylase CBP/P300 (Nejire) (Figure 6 - supplement 1**D**). These results argue that there is not a general change in the permeability of nuclear pores that can account for the increase in transcription at gastrulation.

We next investigated whether nuclear levels of Twist change at the time of gastrulation. To do so, we used a Twist-LlamaTag fusion ***(Bothma et al. 2018)***, so that nuclear levels of newly-encoded Twist could be detected via a ubiquitously expressed GFP, without the delay from protein folding that occurs when visualizing fluorescent proteins directly (Figure 6**C**). The measurements showed that Twist levels increase in the mesoderm throughout nc14. However, no clear change or additional increase in nuclear levels occurred in mesectoderm cells at the time of gastrulation (Figure 6**AB**, **Video 7**). These results argue that changes in Twist import/levels are not responsible for the observed effects of gastrulation on transcription and are consistent with our previous observation that mutating all Twist binding sites in *m5/m8* $^{[II]}$ does not prevent the increase ***(Falo-Sanjuan et al. 2019).*** We note also that nuclear levels of Su(H)-GFP increased continuously throughout nc14 in a similar manner to Twist, with no step-wise change at the time of gastrulation, while H-GFP remained constant (Figure 6 - supplement 1**D**). Overall, these observations suggest that changes in nuclear import, either general or of specific transcription factors, are not responsible for the increased transcriptional activity occurring during gastrulation.

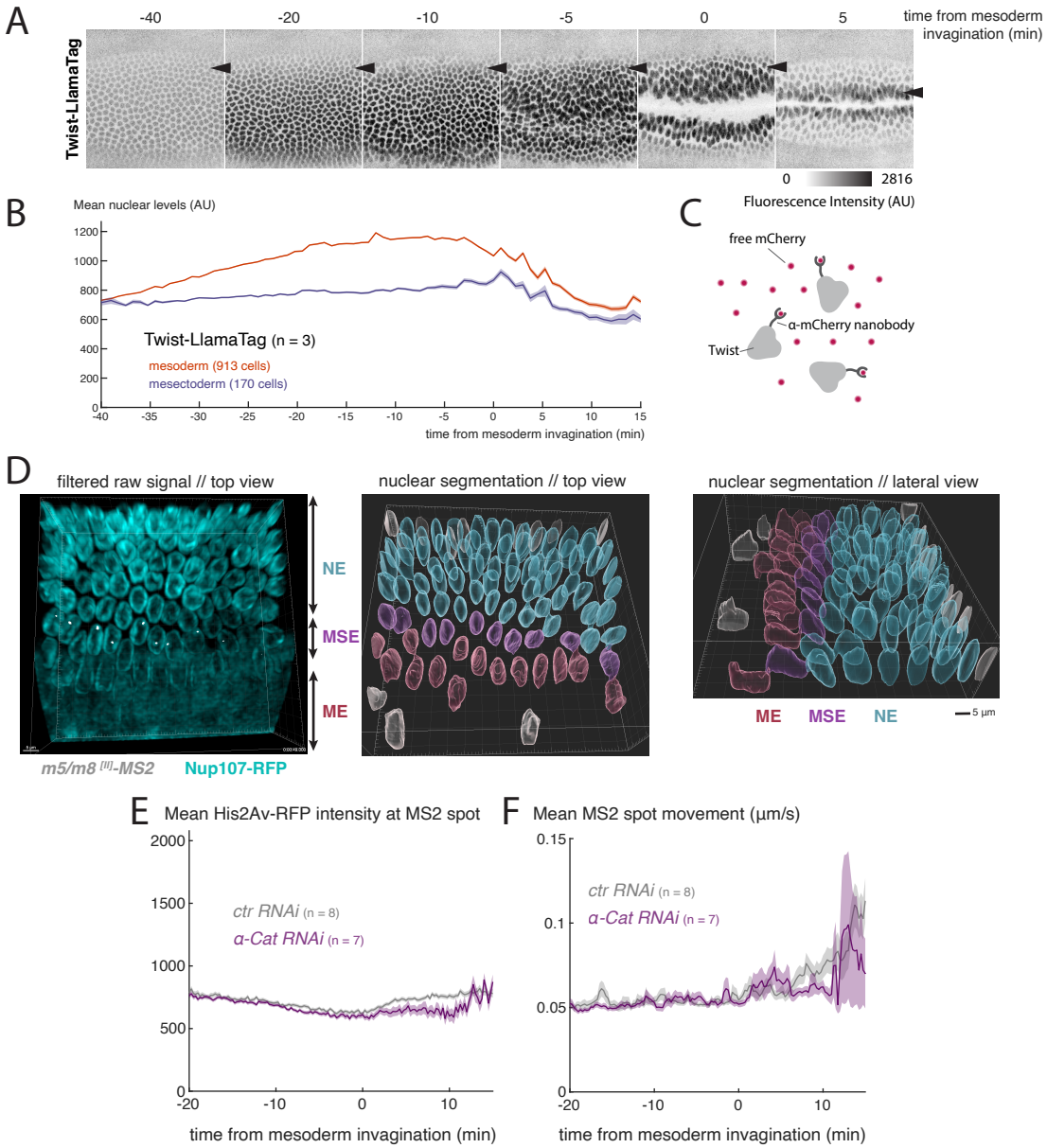

Figure 6. Nuclear levels of Twist and chromatin properties during gastrulation. **A**) Still images from a video of an embryo expressing endogenous Twist fused to LlamaTag, which binds mCherry and allows to visualize nuclear levels of zygotically produced Twist (see **C**). Arrowhead indicates the position of the mesectoderm, note that the Twist levels remain lower in these nuclei than in the central mesoderm. **B**) Quantification of nuclear levels of Twist in mesoderm and mesectoderm during gastrulation. **C**) LlamaTag approach: Twist is fused to an anti-mCherry nanobody (LlamaTag) that binds free and already fluorescent mCherry that has been maternally loaded in the embryo. **D**) Still of the start of mesoderm invagination from a video of an embryo expressing the nuclear membrane marker Nup107-RFP (cyan) and MCP-GFP (grey) to quantify *m5/m8* ^{II} transcription and mark mesectoderm nuclei (left) and segmented nuclei color-coded based on the different cell populations defined from MS2 signal (ME: mesoderm, MSE: mesectoderm, NE: neuroectoderm). Center panel show view from the top and right panel shows lateral view. **E**) Quantification of average His2Av-RFP intensity around the MS2 spot, as a proxy of chromatin compaction, over time in control and *α-Cat RNAi* embryos. **F**) Quantification of the average MS2 spot movement (distance moved relative to the nucleus centroid / time) over time in control and *α-Cat RNAi* embryos. **B**, **E** and **F** show mean and SEM (shaded area) from all cells combined from multiple embryos (n embryo numbers indicated in each). In **F**, values were smoothed over time using a median filter of 8 frames (2 minutes).

Mesectoderm cells tilt and change shape during gastrulation ***(Leptin 1999; Rauzi et al. 2015).*** To investigate the possibility that cellular deformation induced by gastrulation leads to changes in the nucleus we first imaged a nuclear membrane marker (Nup107-RFP) while monitoring transcription with MS2 system and quantified morphological properties of the nucleus. We found that, during gastrulation, mesoderm nuclei decrease the longest axis and increase the second (*i.e. they become shorter and wider* and mesectoderm nuclei do so to a greater extent than those in the neuroectoderm but less than those in the mesoderm (Figure 6**D**, Figure 6 - supplement 2). The shape-changes could explain the increased sensitivity of the mesectoderm nuclei to gastrulation, because changes in nuclear shape can bring about changes in chromatin organization or accessibility ***(Guilluy et al. 2014; Versaevel et al. 2012).*** It is challenging to quantify chromatin organization and accessibility a small cell population in living embryos in a time-resolved manner but we used two different quantifications to probe this question. As a proxy for chromatin compaction, we measured the levels of His2Av-RFP at the site of transcription indicated by the MS2 spot. We were unable to detect any change in intensity at the time of gastrulation or across conditions (Figure 6**E**, Figure 6 - supplement 3**A**), suggesting there is no large scale change in chromatin density. Similarly, we used the movement of the MS2 spots to quantify relative mobility of the transcribing locus over time, because chromatin mobility is thought to be associated with its accessibility and activity ***(Gu et al. 2018).*** We observed that there was increased movement of the MS2 transcription puncta during gastrulation (Figure 6**F**, Figure 6 - supplement 3**B**), suggesting that there is an increase in the local accessibility. However, it was difficult to resolve whether this change was a key factor in the gastrulation mediated effects on transcription as the movements became highly erratic in the conditions that impacted gastrulation.

Discussion

Morphogenetic processes integrate with programs of transcriptional regulation during animal development, but little is known about crosstalk between mechanics and transcription, particularly in a native *in vivo* context. Here we have investigated a role of gastrulation in modulating transcription levels in *Drosophila* embryos, where it could

help to form a straight midline boundary. Using the MS2 system to quantitatively image transcription live, a clear transition in the mean levels of transcription from the Notch responsive *m5/m8* enhancer could be detected, and to a lesser degree from the Twist and Dorsal responsive *vnd* enhancer. This transition correlated with the start of mesoderm invagination and was delayed or absent in embryos where gastrulation was perturbed by different manipulations. In conditions where there was a delay, such as in *fog* mutants, the transition in levels was correlated with a delay in mesoderm invagination. We propose that the coupling of the gastrulation movements to the transcription of key targets in the mesectoderm is important to co-ordinate the establishment of a robust and straight boundary at the midline of the embryo.

A plausible link between mechanics and Notch activity, to explain the increase in expression of Notch-regulated enhancers, would be that force is required for Notch cleavage ***(Gordon et al. 2015)***. By increasing membrane tension or cell contacts, the morphogenetic movements associated with gastrulation could enhance the levels of NICD released. Two observations make this scenario an unlikely explanation for the effects on transcription at mesoderm invagination. First, bypassing the need for force-mediated activation by ectopically expressing NICD in embryos depleted of full length Notch did not prevent the gastrulation-dependent transition in levels. Indeed, it appears that the elevated transcription at gastrulation may be able to overcome any intrinsic attenuation mechanism that switches off NICD induced transcription ***(Viswanathan et al. 2021)***. Second, an unrelated enhancer, *vnd*, also exhibited an increase in levels at the time of gastrulation that was correspondingly perturbed in *fog* mutants or α-Cat depleted embryos. Altogether, our results argue in favour of a model where the cell movements associated with gastrulation have a direct impact on transcription in the nucleus, rather than altering the levels of Notch activation *per se*.

A common feature of both *m5/m8* and *vnd* enhancers is that their activity in MSE cells is more profoundly influenced by gastrulation than elsewhere in the embryo. This could be due to differences in the context of transcription factors and other regulators present in the MSE cells, that make them more sensitive, or to variations in the magnitude of the mechanical forces exerted by gastrulation. In favor of the latter,

ectoderm cells are thought to have different mechanical properties to the mesoderm and the lateral cells, which contribute to the normal progression of gastrulation ***(Rauzi et al. 2015)***. We therefore hypothesize that transcription levels can be modulated by the forces exerted on cells, and that this effect may be specific to certain classes of enhancers. Here we have found that although both *m5/m8* and *vnd* enhancers show characteristics of such regulation, the Notch dependent *m5/m8* appears the more sensitive. We propose that mechanisms acting at the level of the nucleus will be responsible for transmitting this force-mediated regulation.

To exert effects on nuclear functions, the mechanical changes induced by gastrulation need to be transmitted to the nucleus. The mechanotransduction cascade is thought to involve the cytoskeleton and the LINC complex ***(Chang et al. 2015)***. Along with myosin, the LINC complex is proposed to transmit information about substrate stiffness to the transcriptional machinery ***(Alam et al. 2016)***. A similar mechanism could be involved in the gastrulating embryo to transduce mechanical information at the cell level to changes in transcription, based on the fact that coupling between transcription and gastrulation was no longer evident when the LINC complex was depleted. Although the fact that there are also changes in gastrulation under these conditions make it difficult to conclude that there is a direct effect of the LINC complex, the results are nevertheless consistent with the model. We explored two downstream mechanisms that could ultimately be responsible for increased transcriptional activity. The first was a change in nuclear import, either a general increase in permeability of nuclear factors or a more specific effect on key transcription factors such as Twist. No change in general nuclear import properties were detected and, although a gradual increase in Twist was detected, there was no step change at gastrulation that could account for the sharp increase in transcription. The second was a change in chromatin accessibility. We used some simple methods to probe chromatin compaction and mobility, which indicated that the chromatin becomes more mobile at gastrulation. Higher resolution approaches at the single cell level would be needed to ascertain whether these changes are indeed influenced by gastrulation. Finally, it is also possible that subtle changes in several different of these processes are required to bring about the step-change in transcription,

and that each alone makes only a minor contribution.

There is increasing evidence that substrate stiffness and mechanical forces can influence cell fate decisions ***(Alam et al. 2016; Wei et al. 2015; Roy et al. 2018; Muncie et al. 2020).*** Our data showing a connection between gastrulation and transcription levels support the suggestion that there are mechanisms connecting the mechanical properties experienced by cells with the transcriptional output. In the mesectoderm, these effects may be important to ensure that a robust and straight boundary is positioned at the midline. Such a connectivity, between forces and transcription levels, is likely to be of major significance in building tissues and organs, to ensure that the correct structure and shape are adopted in the context of the developing organism.

Methods

Fly strains and genetics

The MS2 reporter *m5/m8* $^{[II]}$ (*m5/m8-peve-24xMS2-lacZ-SV40*[25C]), inserted in the landing site attP40-25C in the second chromosome ***(Bischof et al. 2013)***, other reporters used in Figure 1 and the *eve2-FRT-STOP-FRT-NICD*[51D] construct used to ectopically express NICD have been previously described ***(Falo-Sanjuan et al. 2019).*** *vnd-MS2* (*vndEEE-peve-24xMS2-lacZ-SV40*) was generated by replacing *m5/m8* for the *vndEEE* enhancer, as defined by ***Stathopoulos et al. 2002***, using primers *GGGAAGCTTGGGTAAGCACAAGGATTCC* and *GGGACCGGTCGAATAAGCTGCAAGGAGATC* with *Hind*III and *Age*I sites. The resulting plasmid was inserted in the same attP landing site (attP40-25C) as *m5/m8* by φC31 mediated recombination ***(Bischof et al. 2013).*** Full genotypes of used lines are detailed in **Table** 1.

Table 1. Full genotypes and sources of used *Drosophila* lines

Name (Chr)	Full genotype	Source
His2Av::RFP (III)	w[*];P{w[+mC]=His2Av-mRFP1}III.1	BDSC #23650
His2Av::RFP; nos-MCP::GFP	y[1] w[*]; P{w[+mC]=His2Av-mRFP1}II.2; P{w[+mC]=nos-MCP.EGFP}2	BDSC #60340
His2Av::iRFP, nos-MCP::mCherry (II)	yw; nos-MCP-NoNLS-mCherry, Histone-iRFP	*Eck et al. 2020; Liu et al. 2021*
nos-MCP::mCherry (III)	yw;; nos-MCP-NoNLS-mCherry	*Liu et al. 2021*
vasa-mCherry (III)	yw; pCasper-vasa-mCherry	*YJ. Kim, J. Zhao, HG. Garcia, unpublished results*
Gap43::mCherry (I)	Pw[+mC]=sqhp-Gap43::mCherry	*Izquierdo et al. 2018*
Nup107::RFP (III)	w[*]; wg[Sp-1]/CyO; P{w[+mC]=mRFP-Nup107.K}7.1	BDSC #35517
αTub-Gal4::VP16 (II)	w[*]; P{w[+mC]=matalpha4-GAL-VP16}V2H	BDSC #7062
ovo-FLP (I)	P{w[+mC]=ovo-FLP.R}M1A, w[*]	BDSC #8727
betaTub85D-FLP (I)	P{ry[+t7.2]=betaTub85D-FLP}1; ry[506]	BDSC #7196
m5/m8-MS2 (II)	w; P{w[+mC]=m5/m8-peve-24xMS2-lacZ-SV40}attP40	*Falo-Sanjuan et al. 2019*
vnd-MS2 (II)	w; P{w[+mC]=vndEEE-peve-24xMS2-lacZ-SV40}attP40	This study
eve2-NICD (II)	w; P{w[+mC]=2xeve2*-FRT-STOP-FRT-NICD-eve3'UTR}attP51D	*Falo-Sanjuan et al. 2019*
Twi-RedLlamaTag (II)	y[1] w[1118]; Twi-JB10 / CyO;	*Bothma et al. 2018*
fog[S4] (I)	y[1] fog[S4]/FM7c	BDSC #2100
w RNAi Valium22 (III)	y[1] sc[*] v[1]; P{y[+t7.7] v[+t1.8]=TRiP.GL00094}attP2	BDSC #35573
α-Cat RNAi Valium20 (III)	y[1] sc[*] v[1] sev[21]; P{y[+t7.7] v[+t1.8]=TRiP.HMS00317}attP2	BDSC #33430
cta RNAi Valium20 (II)	y[1] sc[*] v[1]; P{y[+t7.7] v[+t1.8]=TRiP.HMC03421}attP40	BDSC #51848
RhoGEF2 RNAi Valium20 (III)	y[1] sc[*] v[1]; P{y[+t7.7] v[+t1.8]=TRiP.HMS01118}attP2	BDSC #34643
Notch RNAi Valium20 (III)	y[1] v[1]; P{y[+t7.7] v[+t1.8]=TRiP.HMS00009}attP2	BDSC #33616
zld RNAi Valium20 (II)	y[1] sc[*] v[1]; P{y[+t7.7] v[+t1.8]=TRiP.HMS02441}attP40	BDSC #42016
grh RNAi Valium22 (III)	y[1] sc[*] v[1]; P{y[+t7.7] v[+t1.8]=TRiP.GL01069}attP2	BDSC #36890
klar RNAi Valium20 (III)	y[1] sc[*] v[1] sev[21]; P{y[+t7.7] v[+t1.8]=TRiP.HMS01612}attP2	BDSC #36721
koi RNAi Valium20 (II)	y[1] sc[*] v[1] sev[21]; P{y[+t7.7] v[+t1.8]=TRiP.HMS02172}attP40	BDSC #40924
lamC RNAi Valium20 (II)	y[1] sc[*] v[1] sev[21]; P{y[+t7.7] v[+t1.8]=TRiP.HMC04816}attP40	BDSC #57501
zld::GFP (III)	w[1118]; PBac{y[+mDint2] w[+mC]=zld-GFP.FPTB}VK00033 / TM3, Sb[1]	BDSC #51350
Su(H)::GFP (III)	M{Su(H).WT.EGFP}attP86F	*Gomez-Lamarca et al. 2018*
H::GFP (II)	M{H.WT.EGFP}51D	*Gomez-Lamarca et al. 2018*
nej::venus	w[1118] PBac{602.P.SVS-1}nejCPTI000727	Kyoto #115119
Med4::GFP	PBac{fTRG00975.sfGFP-TVPTBF}VK00002	VDRC #v318702
Med17:GFP	PBac{fTRG00979.sfGFP-TVPTBF}VK00002	VDRC #v318704
skd::venus	w[1118]; PBac{681.P.FSVS-1}skdCPTI001170	Kyoto #115130
vasa-eGFP (III)	yw; pCasper-vasa-eGFP	*Kim et al. 2021*
hs-FLP ;; ubi-nls::GFP, FRT80E	Pry[+t7.2]=hsFLP22, y[1] w[*]; Kr[If-1]/CyO; Pw[+mC]=Ubi-GFP(S65T)nls3L PBacw[+mC]=WHND-MLRQ[f00651]	BDSC #76329
nos-nls::PCP::GFP		*Courtesy from Tim Weil and Liz Gavis*

fog mutant background

To test expression from *m5/m8* and *vnd* in the *fog* mutant background, third chromosome recombinants *His2av-RFP, nos-MCP-GFP* **(Falo-Sanjuan et al. 2019)** were combined with a *fog* null allele (*fog[S4]*, BDSC #2100). Control embryos were obtained by crossing *His2av-RFP, nos-MCP-GFP* females with *m5/m8* or *vnd* males. Hemizygous *fog* mutant embryos were obtained by crossing *fog[S4] / FM6* ;; *His2av-RFP , nos-MCP-GFP* with *m5/m8* or *vnd* males and they were recognized by the presence of ectopic folds after gastrulation and embryonic lethality. Other embryos obtained from the same cross were grouped together and labelled *fog* $^{+/+/-}$. To combine the *fog* background with ectopic NICD produced by *eve2-NICD*, *fog[S4]* was combined with *eve2-FRT-STOP-FRT-NICD* and crossed with *ovo-FLP* ;; *His2av-RFP , nos-MCP-GFP*. F1 females containing all transgenes were crossed with *m5/m8-MS2* males; and induce removal of the FRT-STOP-FRT cassette in the germline so that NICD is produced in the *eve2* pattern in F2 embryos. Controls for this experiment were obtained by crossing *eve2-FRT-STOP-FRT-NICD* with *ovo-FLP* ;; *His2av-RFP , nos-MCP-GFP* and F1 females with *m5/m8-MS2* males.

Maternal KD

The maternal driver *αTub-Gal4::VP16* (BDSC # 7062) was combined with *His2av-RFP, nos-MCP-GFP* to generate *αTub-Gal4::VP16* ; *His2Av-RFP*, *nos-MCP-GFP*. To knock down genes from the maternal germline, this was crossed with with UASp-RNAi lines detailed in **Table** 1 or *UASp-w-RNAi* as control (BDSC #35573). Females *αTub-Gal4::VP16 / +* ; *His2Av-RFP*, *nos-MCP-GFP / UASp-RNAi* or *αTub-Gal4::VP16 / UASp-RNAi* ; *His2Av-RFP*, *nos-MCP-GFP / +* were crossed with *m5/m8-MS2* or *vnd-MS2* to obtain the experimental embryos. To combine this with ectopic NICD, *m5/m8*, *eve2-FRT-STOP-FRT-NICD* recombinants **(Falo-Sanjuan et al. 2019)** had been previously crossed with *βTub-FLP* and males *βTub-FLP* / Y ; *m5/m8*,*eve2-FRT-STOP-FRT-NICD / +*, which induce FRT-STOP-FRT removal in the germline, crossed with females in which germline KD occurs. In this way, the resulting embryos express both MS2 and *eve2-NICD*, and candidate genes have been maternally knocked down. To quantify the degree of maternal Klar and Koi KD, *αTub-Gal4::VP16* was

crossed with the same lines and F2 embryos were collected for RT-qPCR. Levels of Zld KD were checked using a Zld-GFP line. Other RNAi lines have been previously used *(Falo-Sanjuan and Bray 2021; Garcia De Las Bayonas et al. 2019; Wingen et al. 2017; Zraly et al. 2021)* or produced a very strong phenotype.

Crosses performed for each experiment are detailed in **Table** 2.

Table 2. Crosses to obtain embryos used in each experiment

Cross	Figure
♀ *His2Av::RFP* ; *nos-MCP::GFP* x ♂ *m5/m8-peve-MS2-lacZ-SV40*[attP40,II] ***(Falo-Sanjuan et al. 2019)***	Figure 1, Figure 1 - supplement 1
♀ *His2Av::RFP* ; *nos-MCP::GFP* x ♂ *m5/m8-peve-MS2-lacZ-SV40*[attP2,III] ***(Falo-Sanjuan et al. 2019)***	Figure 1 - supplement 1
♀ *His2Av::RFP* ; *nos-MCP::GFP* x ♂ *sim-peve-MS2-lacZ-SV40*[attP40,II] ***(Falo-Sanjuan et al. 2019)***	Figure 1 - supplement 1
♀ *His2Av::RFP* ; *nos-MCP::GFP* x ♂ *m5/m8-pm7-MS2-lacZ-SV40*[attP40,II] ***(Falo-Sanjuan et al. 2019)***	Figure 1 - supplement 1
♀ *His2Av::RFP* ; *nos-MCP::GFP* x ♂ *m5/m8-psimE-MS2-lacZ-SV40*[attP40,II] ***(Falo-Sanjuan et al. 2019)***	Figure 1 - supplement 1
♀ *αTub-Gal4::VP16* / + ; *His2Av::RFP*, *nos-MCP::GFP* / *UASp-w RNAi* ♂ *m5/m8-peve-MS2-lacZ-SV40*[attP40,II]	Figure 2, Figure 2 - supplement 1, Figure 2 - supplement 2, Figure 2 - supplement 4, Figure 3 - supplement 1, Figure 5, Figure 5 - supplement 2, Figure 6, Figure 6 - supplement 3
♀ *αTub-Gal4::VP16* / + ; *His2Av::RFP*, *nos-MCP::GFP* / *UASp-α-Cat RNAi* ♂ *m5/m8-peve-MS2-lacZ-SV40*[attP40,II]	Figure 2, Figure 2 - supplement 1, Figure 2 - supplement 2, Figure 6
♀ *His2Av::RFP*, *nos-MCP::GFP* (III) x ♂ *m5/m8-peve-MS2-lacZ-SV40*[attP40,II]	Figure 2, Figure 2 - supplement 1, Figure 2 - supplement 2, Figure 6 - supplement 3
♀ *fog[S4]* / FM6 ;; *His2Av::RFP*, *nos-MCP::GFP* x ♂ *m5/m8-peve-MS2-lacZ-SV40*[attP40,II]	Figure 2, Figure 2 - supplement 1, Figure 2 - supplement 2, Figure 6 - supplement 3
♀ *αTub-Gal4::VP16* / *UASp-cta RNAi* ; *His2Av::RFP*, *nos-MCP::GFP* / + ♂ *m5/m8-peve-MS2-lacZ-SV40*[attP40,II]	Figure 2, Figure 2 - supplement 1, Figure 2 - supplement 2, Figure 6 - supplement 3
♀ *αTub-Gal4::VP16* / + ; *His2Av::RFP*, *nos-MCP::GFP* / *UASp-RhoGEF2 RNAi* ♂ *m5/m8-peve-MS2-lacZ-SV40*[attP40,II]	Figure 2, Figure 2 - supplement 1, Figure 2 - supplement 2, Figure 6 - supplement 3
♀ *αTub-Gal4::VP16* / + ; *His2Av::RFP*, *nos-MCP::GFP* / *UASp-w RNAi* ♂ *m5/m8-peve-MS2-lacZ-SV40*[attP2,III] ***(Falo-Sanjuan and Bray 2021)***	Figure 2 - supplement 3
♀ *αTub-Gal4::VP16* / + ; *His2Av::RFP*, *nos-MCP::GFP* / *UASp-α-Cat RNAi* ♂ *m5/m8-peve-MS2-lacZ-SV40*[attP2,III] ***(Falo-Sanjuan and Bray 2021)***	Figure 2 - supplement 3
♀ *αTub-Gal4::VP16* / + ; *His2Av::RFP*, *nos-MCP::GFP* / *UASp-w RNAi* ♂ *sim-peve-MS2-lacZ-SV40*[attP40,II]	Figure 2 - supplement 3
♀ *αTub-Gal4::VP16* / + ; *His2Av::RFP*, *nos-MCP::GFP* / *UASp-α-Cat RNAi* ♂ *sim-peve-MS2-lacZ-SV40*[attP40,II]	Figure 2 - supplement 3
♀ *αTub-Gal4::VP16* / *UASp-zld RNAi* ; *His2Av::RFP*, *nos-MCP::GFP* / + ♂ *m5/m8-peve-MS2-lacZ-SV40*[attP40,II]	Figure 2 - supplement 4
♀ *αTub-Gal4::VP16* / + ; *His2Av::RFP*, *nos-MCP::GFP* / *UASp-grh RNAi* ♂ *m5/m8-peve-MS2-lacZ-SV40*[attP40,II]	Figure 2 - supplement 4
♀ x ♂ *αTub-Gal4::VP16* / + ; *zld::GFP* / *UASp-w RNAi*	Figure 2 - supplement 4
♀ x ♂ *αTub-Gal4::VP16* / *UASp-zld RNAi* ; *zld::GFP* / +	Figure 2 - supplement 4

Table 2 (continued). Crosses to obtain embryos used in each experiment

Cross	Figure
♀ *His2Av::RFP*, *nos-MCP::GFP* (III) x ♂ *vndEEE-peve-MS2-lacZ-SV40*[attP40,II]	Figure 3, Figure 3 - supplement 1
♀ *αTub-Gal4::VP16* / + ; *His2Av::RFP*, *nos-MCP::GFP* / *UASp-w RNAi* ♂ *vndEEE-peve-MS2-lacZ-SV40*[attP40,II]	Figure 3, Figure 3 - supplement 1
♀ *αTub-Gal4::VP16* / + ; *His2Av::RFP*, *nos-MCP::GFP* / *UASp-α-Cat RNAi* ♂ *vndEEE-peve-MS2-lacZ-SV40*[attP40,II]	Figure 3, Figure 3 - supplement 1
♀ *αTub-Gal4::VP16* / + ; *His2Av::RFP*, *nos-MCP::GFP* / *UASp-Notch RNAi* ♂ *m5/m8-peve-MS2-lacZ-SV40*[attP40,II]	Figure 3 - supplement 1
♀ *αTub-Gal4::VP16* / + ; *His2Av::RFP*, *nos-MCP::GFP* / *UASp-Notch RNAi* ♂ *vndEEE-peve-MS2-lacZ-SV40*[attP40,II]	Figure 3, Figure 3 - supplement 1
♀ *fog[S4]* / FM6 ;; *His2Av::RFP*, *nos-MCP::GFP* x ♂ *vndEEE-peve-MS2-lacZ-SV40*[attP40,II]	Figure 3, Figure 3 - supplement 1
♀ *ovo-FLP* / + ; *eve2-FRT-STOP-FRT-NICD* / + ; *His2Av::RFP*, *nos-MCP::GFP* / + ♂ *m5/m8-peve-MS2-lacZ-SV40*[attP40,II]	Figure 4, Figure 4 - supplement 1
♀ *ovo-FLP* / *fog[S4]* ; *eve2-FRT-STOP-FRT-NICD* / + ; *His2Av::RFP*, *nos-MCP::GFP* / + ♂ *m5/m8-peve-MS2-lacZ-SV40*[attP40,II]	Figure 4, Figure 4 - supplement 1
♀ *αTub-Gal4::VP16* / + ; *His2Av::RFP*, *nos-MCP::GFP* / *UASp-w RNAi* ♂ *βTub85D-FLP* ; *m5/m8-peve-MS2-lacZ-SV40*, *eve2-FRT-STOP-FRT-NICD* / +	Figure 4, Figure 4 - supplement 1
♀ *αTub-Gal4::VP16* / + ; *His2Av::RFP*, *nos-MCP::GFP* / *UASp-Notch RNAi* ♂ *βTub85D-FLP* ; *m5/m8-peve-MS2-lacZ-SV40*, *eve2-FRT-STOP-FRT-NICD* / +	Figure 4, Figure 4 - supplement 1
♀ *αTub-Gal4::VP16* / + ; *His2Av::RFP*, *nos-MCP::GFP* / *UASp-α-Cat RNAi* ♂ *βTub85D-FLP* ; *m5/m8-peve-MS2-lacZ-SV40*, *eve2-FRT-STOP-FRT-NICD* / +	Figure 4, Figure 4 - supplement 1
♀ *αTub-Gal4::VP16* / + ; *His2Av::RFP*, *nos-MCP::GFP* / *UASp-klar RNAi* ♂ *m5/m8-peve-MS2-lacZ-SV40*[attP40,II]	Figure 5
♀ x ♂ *αTub-Gal4::VP16* / + ; *UASp-w RNAi* / + (for qPCR)	Figure 5 - supplement 2
♀ x ♂ *αTub-Gal4::VP16* / *UASp-koi RNAi* ; + / + (for qPCR)	Figure 5 - supplement 2
♀ x ♂ *αTub-Gal4::VP16* / + ; *UASp-klar RNAi* / + (for qPCR)	Figure 5 - supplement 2
♀ *Gap43::mCherry* ; *nos-MCP::GFP* x ♂ *m5/m8-peve-MS2-lacZ-SV40*[attP40,II] ***(Falo-Sanjuan and Bray 2021)***	Figure 5 - supplement 1
♀ x ♂ *His2Av::iRFP*, *nos-MCP::mCherry* / CyO ; *nos-MCP::mCherry*, *vasa-eGFP*	Figure 6 - supplement 1
♀ x ♂ *ubi-nls::GFP*, FRT80E	Figure 6 - supplement 1
♀ x ♂ *nos-nls::PCP::GFP*	Figure 6 - supplement 1
♀ x ♂ *His2Av::RFP* / + (dextran injected)	Figure 6 - supplement 1
♀ x ♂ *med4-GFP*	Figure 6 - supplement 1
♀ x ♂ *med30-GFP*	Figure 6 - supplement 1
♀ x ♂ *skd-venus*	Figure 6 - supplement 1
♀ *His2Av::iRFP*, *nos-MCP::mCherry* / CyO ; *nos-MCP::mCherry*, *Su(H)::GFP* ♂ *m5/m8-peve-MS2-lacZ-SV40*[attP40,II]	Figure 6 - supplement 1
♀ x ♂ *H::GFP* ; *His2Av::RFP*	Figure 6 - supplement 1
♀ x ♂ *nej-venus*	Figure 6 - supplement 1
♀ *Vasa-mCherry* (III) x ♂ *Twi-JB10/CyO*	Figure 6
♀ *Nup107::RFP*, *nos-MCP::GFP* x ♂ *m5/m8-peve-MS2-lacZ-SV40*[attP40,II]	Figure 6, Figure 6 - supplement 2

Live imaging

Embryos were collected on apple juice agar plates with yeast paste, dechorionated in bleach and mounted in Voltalef medium (Samaro) between a semi-permeable membrane and a coverslip. The ventral side of the embryo was facing the coverslip. Videos were acquired in a Leica SP8 confocal using a 40x apochromatic 1.3 objective, zoom x2 and 400x400px size (providing an XY resolution of 0.36 µm/px), 12 bit depth, 400 Hz image acquisition frequency and pinhole of 4 airy units. 27, 29 or 32 x 1 µm slices were collected, with total acquisition time of 15-20s per frame, depending on the experiment. Different genetic conditions are only compared in the same plot if the same microscope and settings were used.

To image embryos in which nuclear levels of different factors were going to be quantified, multiple embryos were acquired at once using the multi-position setting in the microscope and a final time resolution of 1 or 1.5 min, which also helped reduce bleaching. Depending on the condition only GFP or GFP and His2Av-RFP were imaged.

Dextrans injection

Embryos obtained from crossing *His2Av-RFP / +* females and males were dechorionated, glued with heptane glue to a coverslip, and covered with Voltalef medium (Samaro). Injections were performed on pre-nc10 embryos only using pulled glass needles and dextrans diluted in injection buffer (0.1mM sodium phosphate buffer, 5mM KCl, ***Sharrock et al. 2021***) at a concentration of 0.125 mg/ml for Dextran-40kDa-FITC (Sigma-Aldrich FD40S) and 0.25 mg/ml for Dextran-70kDa-FITC (Sigma-Aldrich 46945).

mRNA extraction and qPCR

RT-qPCR quantification of maternal KD was performed as previously described ***(Falo-Sanjuan and Bray 2021).*** Embryos were dechorionated in bleach and early embryos (pre-nc10) / eggs were selected in Voltalef medium. Pools of 15-20 embryos of each genotype were transferred to eppendorf tubes and dissociated in TRI Reagent (Sigma) with a plastic pestle. mRNA was extracted by adding chloroform, 10 min

centrifugation at 4C and let to precipitate with isopropanol overnight. DNA was then pelleted by 10 min centrifugation at 4C, washed in 70% ethanol, dried and resuspended in DEPC-treated water. Approximately 2 µg of RNA from each sample were DNAse treated with the DNA-free™ DNA Removal Kit (Invitrogen) in the presence of RiboLock RNase Inhibitor (Thermo Scientific). 1 µg of DNA-free RNA was then used for reverse transcription using M-MLV Reverse Transcriptase (Promega) in the presence of RiboLock. RT-qPCR was performed using SYBR Green Mastermix (Sigma) and primers detailed in **Table** 3.

Table 3. Primers used for qPCR

Primer	*Sequence*
klar FWD 1	*GTCTTGCCAAGACATGGATG*
klar REV 1	*GGCTGGTCGACTGAATCTTG*
koi FWD 1	*AGCTGGAGACCACACAAAAC*
koi REV 1	*CGTCTTGGGAGTTTTGTTCC*
koi FWD 2	*GGAACAAAACTCCCAAGACG*
koi REV 2	*TCTGCTGGACCATGTAGTTG*
RpII215 FWD	*GACTCGACTGGAATTGCACC*
RpII215 FWD	*TCTTCATCGGGATACTCGCC*

Image analysis

Tracking nuclei and MS2 quantification

Videos were analyzed using custom MATLAB (MATLAB R2020a, MathWorks) scripts that have been previously described ***(Falo-Sanjuan et al. 2019; Falo-Sanjuan and Bray 2021).***

Briefly, the His2Av-RFP signal was used to segment and track the nuclei in 3D. Each 3D stack was first filtered using a 3D median filter of 3 and increasing the contrast based on the intensity profile of each frame to account for bleaching. This was followed by Fourier transform log filter to enhance round objects ***(Garcia et al. 2013)***, and segmentation by applying a fixed intensity threshold, which was empirically determined. Filters to fill holes in objects, exclusion based on size and 3D watershed accounting

for anisotropic voxel sizes *(Mishchenko 2015)* were used to remove miss-segmented nuclei and split merged nuclei. The final segmented stack was obtained by filtering by size again and and thickening each object. Lastly, each nuclei in the segmented stack was labelled and the position of each centroid (in X, Y and Z) was calculated for tracking.

Nuclei were tracked in 3D by finding the nearest object (minimum Euclidean distance between two centroids in space) in the previous 2 frames which was closer than 6 µm. If no object was found, that nucleus was kept with a new label. If more than one object was 'matched' with the same one in one of the previous 2 frames, both were kept with new labels.

After tracking, the positions of all pixels from each nucleus in each frame were used to measure the maximum fluorescence value in the GFP channel, which was used as a proxy of the spot fluorescence. Note that when a spot cannot be detected by eye this method detects only background, but the signal:background ratio is high enough that the subsequent analysis allows to classify confidently when the maximum value is really representing a spot.

Tracking cell membranes and quantification of cell properties

Videos from embryos expressing the membrane marker Gap43-mCherry *(Izquierdo et al. 2018)* combined with the MS2 system to measure *m5/m8* $^{[II]}$ transcription from *Falo-Sanjuan and Bray 2021* were reanalyzed to correlate cell properties with transcription. First, videos were locally-projected to corrected for the curvature of the embryo using the Fiji plugin LocalZProjector *(Herbert et al. 2021).* All slices from the MCP-GFP channel were used to obtain a maximum projection whereas 3 medial-apical slices (4 µm) from the Gap43-mCherry were used to obtain a maximum intensity projection. Membranes were segmented using TissueAnalyzer *(Aigouy et al. 2016)* and MS2 spots were segmented using the Weka Segmentation Tool *(Arganda-Carreras et al. 2017),* both in Fiji. The following analysis was carried out in Matlab, where cells and spots were independently tracked and then spots were assigned to cells based on what cell each spot most commonly overlapped with. Cells assigned to

MS2 spots were used to define the mesectoderm stripes and cells located in between them were labelled as mesoderm. Mesectoderm cells were then classified as 'active' or 'active+increasing' based on their transcription profiles and the corresponding properties for the cells assigned to them extracted and plotted. Length of contact with ME cells was calculated by adding the number of pixels intersected between each cell thickened by 1 pixel with all the ME cells also thickened by 1 pixel.

Tracking and quantification of nuclear concentrations

Depending on which factor was being analyzed, some videos expressed only the fluorescently-tagged factor of interest (if the nuclear levels were high enough to use for nuclear segmentation) or in combination with His2Av-RFP or His2Av-iRFP. In the first case (nls-GFP, nls-PCP-GFP, Med4-GFP, Med30-GFP, Skd-venus, Nej-venus and Twist-LlamaTag), nuclei were directly segmented from the channel in which nuclear levels were going to be quantified and then average nuclear intensity quantified over time. In the other cases (GFP, dextran injections, Su(H)-GFP and H-GFP), nuclei were segmented and tracked based on the His2Av signal and then average GFP/FITC intensity quantified in each nucleus. We note that because in most cases all cells in the embryo contained these factors, the signal could not be normalized to another region to account for bleaching, and therefore the fluorescent profiles might have been reduced over time due to bleaching.

Nuclear membrane segmentation and quantification of morphological parameters

Nuclear membranes tagged with Nup107-RFP ***(Katsani et al. 2008)*** were segmented in Imaris (Oxford Instruments) using the cell segmentation tool and manual correction. Cells were then classified as ME, MSE or NE by marking the overlap with MS2 signal (MSE) and cells dorsal and ventral to them. Morphological properties of the cell surfaces were extracted from Imaris and plotted in Matlab for each cell population.

Data processing and statistical analysis

MS2 data processing

Processing of MS2 data (definition of active nuclei and normalization for bleaching) has been carried out as described in our previous work ***(Falo-Sanjuan et al. 2019).*** After the fluorescent trace of each nucleus over time was obtained, only nuclei tracked for more than 10 frames were retained. Then, nuclei were classified as inactive or active. To do so, the average of all nuclei (active and inactive) was calculated over time and fitted to a straight line. A median filter of 3 (*i.e.* over a period of 45-60") was applied to each nucleus over time to smooth the trace and ON periods were considered when fluorescent values were 1.2 times the baseline at each time point. This produced an initial segregation of active (nuclei ON for at least 5 frames, *i.e.* 1.25-1.6 min) and inactive nuclei. These parameters were determined empirically on the basis that the filters retained nuclei with spots close to background levels and excluded false positives from bright background pixels, which were validated by overlaying nuclei defined by the pipeline as actively transcribing with the MS2 signal, and confirming that the two were concordant. The mean fluorescence from MCP-GFP in the inactive nuclei was then used to define the background baseline and active nuclei were segregated again in the same manner. The final fluorescence values in the active nuclei were calculated by removing the fitted baseline from the maximum intensity value for each, and normalizing for the percentage that the MCP-GFP fluorescence in inactive nuclei decreased over time to account for the loss of fluorescence due to bleaching. Nuclei active in cycles before nc14 were discarded based on the timing of their activation.

In all videos, time into nc14 was considered from the end of the 13th syncytial division. To avoid early stochastic activity, transcription was considered from 15 min into nc14 in most experiments, except for expression in the presence of maternal Gal4, in which it was considered from 30 min to exclude earlier stochastic activity induced by Gal4VP16. For *vnd*, transcription was considered all throughout nc14. The total mRNA output (in AU) was obtained by adding all the normalized transcription values for each cell in a defined time period. In plots were cells were classified as 'active' or

'active+increasing', nuclei which increase in levels were defined if the average intensity from 15 min of the start of ME invagination was higher than the average of all active nuclei at that point and at least 1.7 times higher than the average intensity in the 15 min prior to ME invagination. Using these values, most nuclei were classified in a way that matched what could be observed by looking directly at the transcription traces.

Quantifying gastrulation progression and changes in transcription levels

Start of apical constriction, start of mesoderm invagination and end of gastrulation were manually defined for each embryo from plots showing the movement of MSE cells. Transcribing nuclei in each region were selected and the average movement of their centroids in the Y axis, corresponding to the DV axis in the embryo, was calculated. This produces a plot with one or two peaks of movement. A large peak of movement is produced during ME invagination, as MSE cells move ventrally. If the embryo is mounted completely ventrally, only this peak of movement is observed. If the orientation of the embryo is tilted, the whole embryo rolls inside the vitelline membrane during apical constriction, which is detected as an earlier peak of movement of cells dorsally. After that, the second peak of movement corresponds with mesoderm invagination. The transition between the two movements, corresponds to and was used to define the start of ME invagination. Similarly, transition point in mean transcription levels was manually defined from each plot showing the mean fluorescence of selected cells, by selecting the inflection point between two different levels of transcription. Only embryos that showed a clear transition in levels were used in the correlation plots, although we note that only in most cases all embryos from each genetic condition were included.

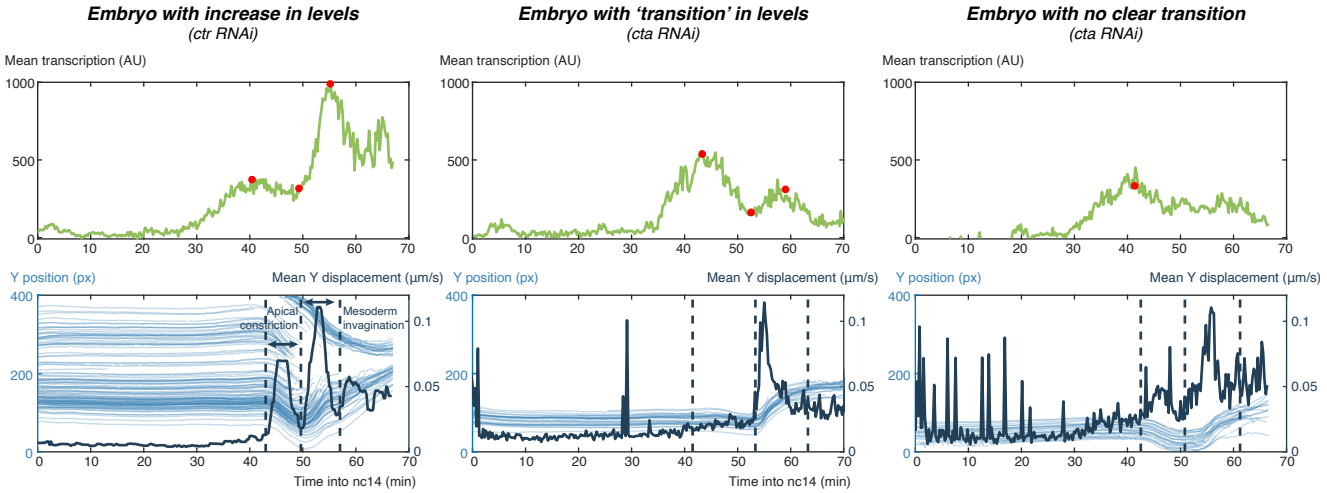

Figure 1 - supplement 2. Quantification of gastrulation progression and changes in transcription levels. Examples of three embryos in which transcription levels increase during gastrulation (left), show a transition in levels (center) or show no clear transition in levels (right). Top: mean levels of transcription from MSE nuclei with red dots indicating the manually annotated plateau and transition in levels. Bottom: plot overlaying movement of all MSE nuclei in the Y axis (left axis, light blue) with mean displacement in the Y axis, corresponding with DV movement (right axis, dark blue). The shapes of the curves in both plots were used to define the start of apical constriction, start of ME invagination and end of gastrulation (dashed lines), based on the cell movement along DV.

Quantifying histone intensity and MS2 spot movement

To quantify average histone intensity around the MS2 spot, spots were segmented using the Differential-of-Gaussians approach previously described *(Garcia et al. 2013)*. A 5x5 pixel window surrounding the MS2 spot was then extracted from the His2Av-RFP channel and the average intensity calculated.

Statistical analysis

In figures and figure legends, n number indicates number of embryos imaged for each biological condition. Where appropriate, n number next to heatmaps indicates total number of cells combining all embryos for each biological condition. Plots showing mean levels of transcription and SEM (standard error of the mean) combine all traces from multiple embryos from the same biological condition.

Reagents and software availability

The MATLAB app to track nuclei, quantify MS2 traces and define properties of gastrulation can be obtained at https://github.com/BrayLab/LiveTrx.

Videos

Video 1 - Activity of *m5/m8* during gastrulation. Video showing His2Av-RFP channel (orthogonal view, left ; and maximum intensity projection, center) and MCP-GFP channel with transcription directed by *m5/m8* $^{[II]}$ (maximum intensity projection, right) in control embryos. The top row shows orthogonal view in the His2Av-RFP channel and maximum Y projection in the MCP-GFP channel. 0.36 µm/px XY resolution, 29x1µm slices and time resolution of 15s/frame. Anterior to the left; embryo imaged from the ventral side. Time indicates minutes from the beginning of nc14. Bottom plot shows mean transcription produced by *m5/m8* $^{[II]}$ in this embryo, synchronized with the video to show the increase in activity occurs as the embryo undergoes gastrulation.

Video 2 - Effects on gastrulation of *α-Cat RNAi* and *fog* mutant background. Videos showing His2Av-RFP channel (orthogonal view, left ; and maximum intensity projection, center) and MCP-GFP channel with transcription directed by *m5/m8* $^{[II]}$ (maximum intensity projection, right) in *α-Cat RNAi* (top) and *fog*$^{-}$ (bottom) embryos. 0.36 µm/px XY resolution, 27x1µm (*α-Cat RNAi*) and 29x1µm (*fog*$^{-}$) slices and time resolution of 15s/frame. Anterior to the left; embryo imaged from the ventral side. Time indicates minutes from the beginning of nc14.

Video 3 - Effects on gastrulation of *cta* and *RhoGEF2 RNAi*. Videos showing His2Av-RFP channel (orthogonal view, left ; and maximum intensity projection, center) and MCP-GFP channel with transcription directed by *m5/m8* $^{[II]}$ (maximum intensity projection, right) in *cta* (top) and *RhoGEF2 RNAi* (bottom) embryos. 0.36 µm/px XY resolution, 29x1µm slices and time resolution of 15s/frame. Anterior to the left; embryo imaged from the ventral side. Time indicates minutes from the beginning of nc14.

Video 4 - Expression of *vnd* in control embryos. Videos showing His2Av-RFP channel (orthogonal view, left ; and maximum intensity projection, center) and MCP-GFP channel with transcription directed by *vnd* (maximum intensity projection, right) in control embryos. 0.36 µm/px XY resolution, 29x1µm slices and time resolution of 15s/frame. Anterior to the left; embryo imaged from the ventral side. Time indicates minutes from the beginning of nc14.

Video 5 - Expression of *m5/m8* $^{[II]}$ upon *eve2-NICD* expression in control, *Notch* and *α-Cat RNAi* embryos. Videos showing His2Av-RFP channel (orthogonal

view, left ; and maximum intensity projection, center) and MCP-GFP channel with transcription directed by *m5/m8* $^{[II]}$ (maximum intensity projection, right) in control (top), *Notch* (middle) and *α-Cat RNAi* (bottom) embryos. 0.36 µm/px XY resolution, 32x1µm slices and time resolution of 20s/frame. Anterior to the left; embryo imaged from the ventral side. Time indicates minutes from the beginning of nc14.

Video 6 - Analysis of cellular shape in relation to *m5/m8* activity. From left to right, video showing: (i) membranes using the marker Gap43-mCherry (maximum intensity projection of 3 µm after surface correction), (ii) transcription from *m5/m8-MS2* $^{[II]}$ (maximum intensity projection of the whole stack after surface correction), (iii) overlaid Gap43-mCherry (magenta) and MCP-GFP (grey) signal, (iv) tracked video showing cell boundaries (grey), cells classified as mesoderm (purple), mesectoderm cells that increase MS2 signal during gastrulation (yellow) and mesectoderm cells that do not increase (orange). 0.36 µm/px XY resolution, 36x1µm slices and time resolution of 20s/frame. Anterior to the left; embryo imaged from the ventral side. Time indicates minutes from the beginning of nc14.

Video 7 - Levels of nuclear Twist during nc14. Video of an embryo expressing endogenous Twist fused to a LlamaTag (anti-mCherry nanobody) that binds maternally provided and fluorescenty-matured mCherry. Inverted maximum intensity projection shown. 0.36 µm/px XY resolution, 34x1µm slices and time resolution of 45s/frame. Anterior to the left; embryo imaged from the ventral side. Time indicates minutes from the beginning of nc14.

Acknowledgments

We thank members of the Bray Lab for helpful discussions. Thanks to Yang Joon Kim, Jiaxi (Jake) Zhao for sharing unpublished flies, Tom Sharrock for advice on embryo injections, members of the Sanson, Weil and Garcia labs for providing flies and advice and to Kat Millen and the Genetics Fly Facility for injections. We acknowledge the Cambridge Advanced Imaging Centre for their support, assistance in this work and use of their microscopes. This work was supported by a Wellcome Trust Investigator Award (212207/Z/18/Z) and a Medical Research Council Programme grant (MR/T014156/1) and by a PhD studentship to J.F.-S from the Wellcome Trust (109144/Z/15/Z).

Declaration of Interests

The authors declare no competing interests.

References

Aigouy, Benoit, Umetsu, Daiki, and Eaton, Suzanne (2016). Segmentation and quantitative analysis of epithelial tissues. Methods Mol. Biol. *1478*, 227–239.

Alam, Samer G., Zhang, Qiao, Prasad, Nripesh, Li, Yuan, Chamala, Srikar, Kuchibhotla, Ram, KC, Birendra, Aggarwal, Varun, Shrestha, Shristi, Jones, Angela L., Levy, Shawn E., Roux, Kyle J., Nickerson, Jeffrey A., and Lele, Tanmay P. (2016). The mammalian LINC complex regulates genome transcriptional responses to substrate rigidity. Sci. Rep. *6*.1, 38063.

Arganda-Carreras, Ignacio, Kaynig, Verena, Rueden, Curtis, Eliceiri, Kevin W., Schindelin, Johannes, Cardona, Albert, and Seung, H. Sebastian (2017). Trainable Weka Segmentation: A machine learning tool for microscopy pixel classification. Bioinformatics *33*.15, 2424–2426.

Barrett, Kathy, Leptin, Maria, and Settleman, Jeffrey (1997). The Rho GTPase and a Putative RhoGEF Mediate a Signaling Pathway for the Cell Shape Changes in Drosophila Gastrulation. Cell *91*.7, 905–915.

Bischof, Johannes et al. (2013). A versatile platform for creating a comprehensive UAS-ORFeome library in Drosophila. Development *140*.11, 2434–42.

Bothma, Jacques P., Norstad, Matthew R., Alamos, Simon, and Garcia, Hernan G. (2018). LlamaTags: A Versatile Tool to Image Transcription Factor Dynamics in Live Embryos. Cell *173*.7, 1810–1822.e16.

Boumendil, Charlene, Hari, Priya, Olsen, Karl C.F., Acosta, Juan Carlos, and Bickmore, Wendy A (2019). Nuclear pore density controls heterochromatin reorganization during senescence. Genes Dev. *33*.3-4, 144–149.

Chang, Wakam, Worman, Howard J., and Gundersen, Gregg G. (2015). Accessorizing and anchoring the LINC complex for multifunctionality. J. Cell Biol. *208*.1, 11–22.

Costa, Michael, Wilson, Ellen T., and Wieschaus, Eric (1994). A putative cell signal encoded by the folded gastrulation gene coordinates cell shape changes during Drosophila gastrulation. Cell *76*.6, 1075–1089.

Cowden, John and Levine, Michael (2002). The Snail repressor positions Notch signaling in the Drosophila embryo. Development *129*.7, 1785–93.

Crisp, Melissa, Liu, Qian, Roux, Kyle, Rattner, J. B., Shanahan, Catherine, Burke, Brian, Stahl, Phillip D., and Hodzic, Didier (2006). Coupling of the nucleus and cytoplasm: Role of the LINC complex. J. Cell Biol. *172*.1, 41–53.

Dawes-Hoang, Rachel E., Parmar, Kush M, Christiansen, Audrey E, Phelps, Chris B, Brand, Andrea H, and Wieschaus, Eric F (2005). folded gastrulation, cell shape change and the control of myosin localization. Development *132*.18, 4165–78.

Desprat, Nicolas, Supatto, Willy, Pouille, Philippe-alexandre, Beaurepaire, Emmanuel, and Farge, Emmanuel (2008). Tissue Deformation Modulates Twist Expression to Determine Anterior Midgut Differentiation in Drosophila Embryos. Dev. Cell *15*.3, 470–477.

Eck, Elizabeth, Liu, Jonathan, Kazemzadeh-Atoufi, Maryam, Ghoreishi, Sydney, Blythe, Shelby, and Garcia, Hernan G. (2020). Quantitative dissection of transcription in development yields evidence for transcription factor-driven chromatin accessibility. Elife *9*, 1–99.

Engel-Pizcueta, Carolyn and Pujades, Cristina (2021). Interplay Between Notch and YAP/TAZ Pathways in the Regulation of Cell Fate During Embryo Development. Front. Cell Dev. Biol. *9*.August, 1–13.

Falo-Sanjuan, Julia and Bray, Sarah J (2021). Membrane architecture and adherens junctions contribute to strong Notch pathway activation. Development, 2021.05.26.445755.

Falo-Sanjuan, Julia, Lammers, Nicholas C, Garcia, Hernan G, and Bray, Sarah J (2019). Enhancer Priming Enables Fast and Sustained Transcriptional Responses to Notch Signaling. Dev. Cell *50*.4, 411–425.e8.

Farge, Emmanuel (2003). Mechanical induction of Twist in the Drosophila foregut/stomodeal primordium. Curr. Biol. *13*.16, 1365–1377.

Fuse, Naoyuki, Yu, Fengwei, and Hirose, Susumu (2013). Gprk2 adjusts Fog signaling to organize cell movements in Drosophila gastrulation. Development *140*.20, 4246–4255.

Garcia, Hernan G., Tikhonov, Mikhail, Lin, Albert, and Gregor, Thomas (2013). Quantitative Imaging of Transcription in Living Drosophila Embryos Links Polymerase Activity to Patterning. Curr. Biol. *23*.21, 2140–2145.

Garcia De Las Bayonas, Alain, Philippe, Jean-marc, Lellouch, Annemarie C, and Lecuit, Thomas (2019). Distinct RhoGEFs Activate Apical and Junctional Contractility under Control of G Proteins during Epithelial Morphogenesis. Curr. Biol. *29*.20, 3370–3385.e7.

Gomez-Lamarca, Maria J., Falo-Sanjuan, Julia, Stojnic, Robert, Abdul Rehman, Sohaib, Muresan, Leila, Jones, Matthew L., Pillidge, Zoe, Cerda-Moya, Gustavo, Yuan, Zhenyu, Baloul, Sarah, Valenti, Phillippe, Bystricky, Kerstin, Payre, Francois, O'Holleran, Kevin, Kovall, Rhett, and Bray, Sarah J. (2018). Activation of the Notch Signaling Pathway In Vivo Elicits Changes in CSL Nuclear Dynamics. Dev. Cell *44*.5, 611–623.e7.

Gordon, Wendy R., Vardar-Ulu, Didem, Histen, Gavin, Sanchez-Irizarry, Cheryll, Aster, Jon C., and Blacklow, Stephen C. (2007). Structural basis for autoinhibition of Notch. Nat. Struct. Mol. Biol. *14*.4, 295–300.

Gordon, Wendy R., Zimmerman, Brandon, He, Li, Miles, Laura J., Huang, Jiuhong, Tiyanont, Kittichoat, McArthur, Debbie G., Aster, Jon C., Perrimon, Norbert, Loparo, Joseph J., and Blacklow, Stephen C. (2015). Mechanical Allostery: Evidence for a Force Requirement in the Proteolytic Activation of Notch. Dev. Cell *33*.6, 729–736.

Gozalo, Alejandro, Duke, Ashley, Lan, Yemin, Pascual-Garcia, Pau, Talamas, Jessica A, Nguyen, Son C, Shah, Parisha P., Jain, Rajan, Joyce, Eric F, and Capelson, Maya (2020). Core Components of the Nuclear Pore Bind Distinct States of Chromatin and Contribute to Polycomb Repression. Mol. Cell *77*.1, 67–81.e7.

Gu, Bo, Swigut, Tomek, Spencley, Andrew, Bauer, Matthew R., Chung, Mingyu, Meyer, Tobias, and Wysocka, Joanna (2018). Transcription-coupled changes in nuclear mobility of mammalian cis-regulatory elements. Science (80-.). *359*.6379, 1050–1055.

Guilluy, Christophe, Osborne, Lukas D., Van Landeghem, Laurianne, Sharek, Lisa, Superfine, Richard, Garcia-Mata, Rafael, and Burridge, Keith (2014). Isolated nuclei adapt to force and reveal a mechanotransduction pathway in the nucleus. Nat. Cell Biol. *16*.4, 376–381.

Hamouda, Mehdi S., Labouesse, Celine, and Chalut, Kevin J. (2020). Nuclear mechanotransduction in stem cells. Curr. Opin. Cell Biol. *64*, 97–104.

Hampoelz, Bernhard, Mackmull, Marie-Therese, Machado, Pedro, Ronchi, Paolo, Bui, Khanh Huy, Schieber, Nicole, Santarella-Mellwig, Rachel, Necakov, Aleksandar, Andrés-Pons, Amparo, Philippe, Jean Marc, Lecuit, Thomas, Schwab, Yannick, and Beck, Martin (2016).

Pre-assembled Nuclear Pores Insert into the Nuclear Envelope during Early Development. Cell *166*.3, 664–678.

Han, Sisu et al. (2021). Proneural genes define ground-state rules to regulate neurogenic patterning and cortical folding. Neuron *109*.18, 2847–2863.e11.

Herbert, Sébastien, Valon, Léo, Mancini, Laure, Dray, Nicolas, Caldarelli, Paolo, Gros, Jérôme, Esposito, Elric, Shorte, Spencer L., Bally-Cuif, Laure, Aulner, Nathalie, Levayer, Romain, and Tinevez, Jean Yves (2021). LocalZProjector and DeProj: a toolbox for local 2D projection and accurate morphometrics of large 3D microscopy images. BMC Biol. *19*.1, 1–13.

Hong, Joung Woo, Park, Kye Won, and Levine, Michael S. (2013). Temporal regulation of single-minded target genes in the ventral midline of the Drosophila central nervous system. Dev. Biol. *380*.2, 335–343.

Hummel, Thomas, Schimmelpfeng, Kristina, and Klämbt, Christian (1999). Commissure Formation in the Embryonic CNS ofDrosophila. Dev. Biol. *209*.2, 381–398.

Izquierdo, Emiliano, Quinkler, Theresa, and De Renzis, Stefano (2018). Guided morphogenesis through optogenetic activation of Rho signalling during early Drosophila embryogenesis. Nat. Commun. *9*.1, 2366.

Jahed, Zeinab, Soheilypour, Mohammad, Peyro, Mohaddeseh, and Mofrad, Mohammad R.K. (2016). The LINC and NPC relationship - it's complicated! J. Cell Sci. *129*.17, 3219–3229.

Katsani, Katerina R., Karess, Roger E., Dostatni, Nathalie, and Doye, Valerie (2008). In Vivo Dynamics of Drosophila Nuclear Envelope Components. Mol. Biol. Cell *19*.1, 3652–3666.

Kim, Yang Joon, Rhee, Kaitlin, Liu, Jonathan, Jeammet, Paul, Turner, Meghan, Small, Stephen, and Garcia, Hernan G (2021). Predictive modeling reveals that higher-order cooperativity drives transcriptional repression in a synthetic developmental enhancer. bioRxiv, 1–55.

Kolsch, V., Seher, Thomas, Fernandez-Ballester, G. J., Serrano, Luis, and Leptin, Maria (2007). Control of Drosophila Gastrulation by Apical Localization of Adherens Junctions and RhoGEF2. Science (80-.). *315*.5810, 384–386.

Kosman, D and Small, S (1997). Concentration-dependent patterning by an ectopic expression domain of the Drosophila gap gene knirps. Development *124*.7, 1343–54.

Leptin, M. and Grunewald, B. (1990). Cell shape changes during gastrulation in Drosophila. Development *110*.1, 73–84.

Leptin, Maria (1999). Gastrulation in Drosophila: the logic and the cellular mechanisms. EMBO J. *18*.12, 3187–3192.

Liu, Jonathan, Hansen, Donald, Eck, Elizabeth, Kim, Yang Joon, Turner, Meghan, Alamos, Simon, and Garcia, Hernan (2021). Real-time single-cell characterization of the eukaryotic transcription cycle reveals correlations between RNA initiation, elongation, and cleavage. PLoS Comput. Biol. *17*.5, 1–26.

Lloyd-Lewis, Bethan, Mourikis, Philippos, and Fre, Silvia (2019). Notch signalling: sensor and instructor of the microenvironment to coordinate cell fate and organ morphogenesis. Curr. Opin. Cell Biol. *61*, 16–23.

Manning, Alyssa J., Peters, Kimberly A., Peifer, Mark, and Rogers, Stephen L. (2013). Regulation of epithelial morphogenesis by the gprotein-coupled receptor mist and its ligand fog. Sci. Signal. *6*.301, 1–11.

Markstein, Michele, Zinzen, Robert, Markstein, Peter, Yee, Ka-Ping, Erives, Albert, Stathopoulos, Angela, and Levine, Michael (2004). A regulatory code for neurogenic gene expression in the Drosophila embryo. Development *131*.10, 2387–94.

Martin, Adam C. (2020). The Physical Mechanisms of Drosophila Gastrulation: Mesoderm and Endoderm Invagination. Genetics *214*.3, 543–560.

Martin, Adam C., Kaschube, Matthias, and Wieschaus, Eric F. (2009). Pulsed contractions of an actin-myosin network drive apical constriction. Nature *457*.7228, 495–499.

Martín-Bermudo, M D, Carmena, A, and Jiménez, F (1995). Neurogenic genes control gene expression at the transcriptional level in early neurogenesis and in mesectoderm specification. Development *121*.1, 219–224.

Mishchenko, Yuriy (2015). A fast algorithm for computation of discrete Euclidean distance transform in three or more dimensions on vector processing architectures. Signal, Image Video Process. *9*.1, 19–27.

Morel, V, Le Borgne, R, and Schweisguth, F (2003). Snail is required for Delta endocytosis and Notch-dependent activation of single-minded expression. Dev. Genes Evol. *213*.2, 65–72.

Morel, Véronique and Schweisguth, François (2000). Repression by Suppressor of Hairless and activation by Notch are required to define a single row of single-minded expressing cells in the Drosophila embryo. Genes Dev. *14*.3, 377–388.

Muncie, Jonathon M., Ayad, Nadia M.E., Lakins, Johnathon N., Xue, Xufeng, Fu, Jianping, and Weaver, Valerie M. (2020). Mechanical Tension Promotes Formation of Gastrulation-like Nodes and Patterns Mesoderm Specification in Human Embryonic Stem Cells. Dev. Cell *55*.6, 679–694.e11.

Nambu, John R., Franks, Robert G., Hu, Song, and Crews, Stephen T. (1990). The single-minded gene of Drosophila is required for the expression of genes important for the development of CNS midline cells. Cell *63*.1, 63–75.

Nambu, John R., Lewis, Josephine O., Wharton, Keith A., and Crews, Stephen T. (1991). The Drosophila single-minded gene encodes a helix-loop-helix protein that acts as a master regulator of CNS midline development. Cell *67*.6, 1157–1167.

Paolini, Alessio, Fontana, Federica, Pham, Van Cuong, Rödel, Claudia Jasmin, and Abdelilah-Seyfried, Salim (2021). Mechanosensitive Notch-Dll4 and Klf2-Wnt9 signaling pathways intersect in guiding valvulogenesis in zebrafish. Cell Rep. *37*.1.

Parks, Suki and Wieschaus, Eric (1991). The drosophila gastrulation gene concertina encodes a Gα-like protein. Cell *64*.2, 447–458.

Pouille, Philippe-alexandre, Ahmadi, Padra, Brunet, Anne-christine, and Farge, Emmanuel (2009). Mechanical Signals Trigger Myosin II Redistribution and Mesoderm Invagination in Drosophila Embryos. *2*.66, 1–9.

Rauzi, Matteo, Krzic, Uros, Saunders, Timothy E., Krajnc, Matej, Ziherl, Primož, Hufnagel, Lars, and Leptin, Maria (2015). Embryo-scale tissue mechanics during Drosophila gastrulation movements. Nat. Commun. *6*.1, 8677.

Roy, Bibhas, Venkatachalapathy, Saradha, Ratna, Prasuna, Wang, Yejun, Jokhun, Doorgesh Sharma, Nagarajan, Mallika, and Shivashankar, G. V. (2018). Laterally confined growth of cells induces nuclear reprogramming in the absence of exogenous biochemical factors. Proc. Natl. Acad. Sci. U. S. A. *115*.21, E4741–E4750.

Sharrock, Thomas E., Blanchard, Guy B., Evans, Jenny, and Sanson, Bénédicte (2021). Different temporal requirements for the LRR transmembrane receptors Tartan and Toll-2 in 2 the formation of contractile interfaces at compartmental boundaries. bioRxiv.

Shaya, Oren, Binshtok, Udi, Hersch, Micha, Rivkin, Dmitri, Weinreb, Sheila, Amir-Zilberstein, Liat, Khamaisi, Bassma, Oppenheim, Olya, Desai, Ravi A., Goodyear, Richard J., Richard-

son, Guy P., Chen, Christopher S., and Sprinzak, David (2017). Cell-Cell Contact Area Affects Notch Signaling and Notch-Dependent Patterning. Dev. Cell *40*.5, 505–511.e6.

Stathopoulos, Angelike, Van Drenth, Madeleine, Erives, Albert, Markstein, Michele, and Levine, Michael (2002). Whole-genome analysis of Dorsal-ventral patterning in the Drosophila embryo. Cell *111*.5, 687–701.

Supatto, Willy, McMahon, Amy, Fraser, Scott E., and Stathopoulos, Angelike (2009). Quantitative imaging of collective cell migration during Drosophila gastrulation: Multiphoton microscopy and computational analysis. Nat. Protoc. *4*.10, 1397–1412.

Sweeton, D, Parks, S, Costa, M, and Wieschaus, E (1991). Gastrulation in Drosophila: the formation of the ventral furrow and posterior midgut invaginations. Development *112*.3, 775–89.

Uzer, Gunes, Bas, Guniz, Sen, Buer, Xie, Zhihui, Birks, Scott, Olcum, Melis, McGrath, Cody, Styner, Maya, and Rubin, Janet (2018). Sun-mediated mechanical LINC between nucleus and cytoskeleton regulates βcatenin nuclear access. J. Biomech. *74*, 32–40.

Versaevel, Marie, Grevesse, Thomas, and Gabriele, Sylvain (2012). Spatial coordination between cell and nuclear shape within micropatterned endothelial cells. Nat. Commun. *3*.1, 671.

Viswanathan, Ranjith, Hartmann, Jonas, Pallares Cartes, Cristina, and De Renzis, Stefano (2021). Desensitisation of Notch signalling through dynamic adaptation in the nucleus. EMBO J., 1–14.

Wei, Spencer C., Fattet, Laurent, Tsai, Jeff H., Guo, Yurong, Pai, Vincent H., Majeski, Hannah E., Chen, Albert C., Sah, Robert L., Taylor, Susan S., Engler, Adam J., and Yang, Jing (2015). Matrix stiffness drives epithelial-mesenchymal transition and tumour metastasis through a TWIST1-G3BP2 mechanotransduction pathway. Nat. Cell Biol. *17*.5, 678–688.

Wheeler, Scott R., Stagg, Stephanie B., and Crews, Stephen T. (2008). Multiple Notch signaling events control Drosophila CNS midline neurogenesis, gliogenesis and neuronal identity. Development *135*.18, 3071–3079.

Wingen, Almut, Carrera, Pilar, Ekaterini Psathaki, Olympia, Voelzmann, André, Paululat, Achim, and Hoch, Michael (2017). Debris buster is a Drosophila scavenger receptor essential for airway physiology. Dev. Biol. *430*.1, 52–68.

Yu, Jessica C., Balaghi, Negar, Erdemci-Tandogan, Gonca, Castle, Veronica, and Fernandez-Gonzalez, Rodrigo (2021). Myosin cables control the timing of tissue internalization in the Drosophila embryo. Cells Dev. July, 203721.

Zinzen, Robert P., Cande, Jessica, Ronshaugen, Matthew, Papatsenko, Dmitri, and Levine, Mike (2006). Evolution of the Ventral Midline in Insect Embryos. Dev. Cell *11*.6, 895–902.

Zraly, Claudia B., Zakkar, Abdul, Perez, John Hertenstein, Ng, Jeffrey, White, Kevin P., Slattery, Matthew, and Dingwall, Andrew K. (2021). The Drosophila MLR COMPASS complex is essential for programming cis-regulatory information and maintaining epigenetic memory during development. Nucleic Acids Res. *48*.7, 3476–3495.

Figure Supplements

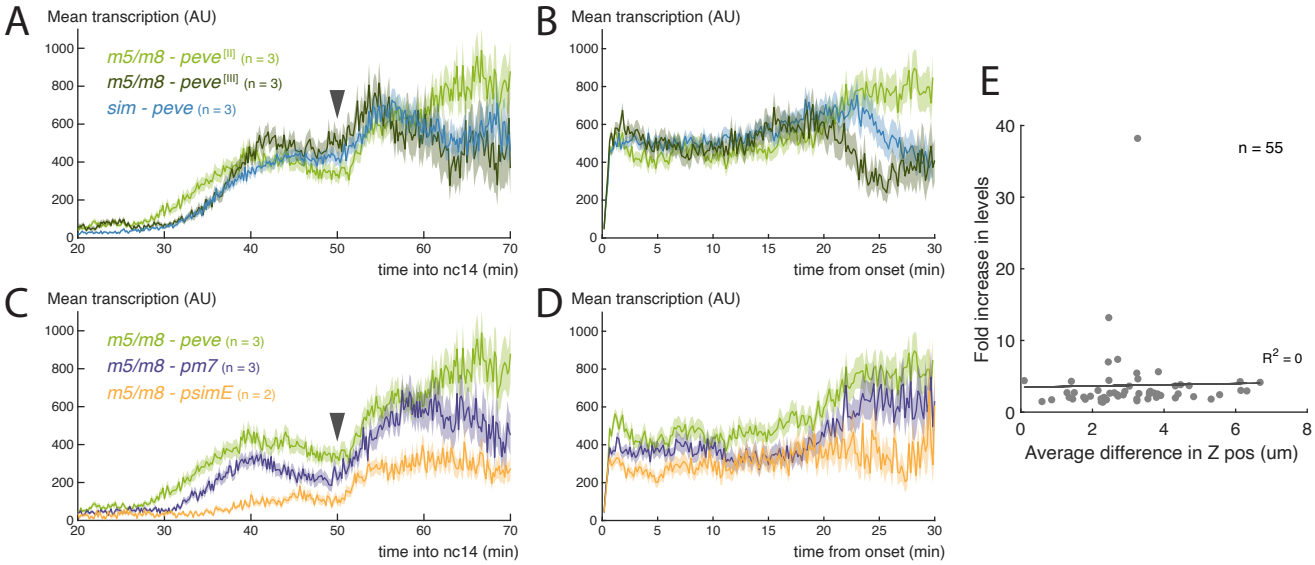

Figure 1 - supplement 1. Increase in Notch dependent transcription at the time of gastrulation. A) Mean profile of activity of the Notch responsive enhancers *sim* and *m5/m8* inserted in landing sites in the second ([II]) and third ([III]) chromosomes. **B**) Mean profile of activity of the Notch responsive enhancers *sim* and *m5/m8* inserted in landing sites in the second ([II]) and third ([III]) chromosomes, aligned by onset times. **C**) Mean profile of activity of *m5/m8* $^{[II]}$ with different promoters (*peve*, *pm7* and *psimE*). **D**) Mean profile of activity of *m5/m8* $^{[II]}$ with different promoters (*peve*, *pm7* and *psimE*), aligned by onset times. Light green plots (*m5/m8-peve* $^{[II]}$) are the same as shown in Figure 1. Mean transcription profiles show mean and SEM (shaded area) of MS2 fluorescent traces from all cells combined from multiple embryos (n embryo numbers indicated in each). **E**) Correlation between the fold increase in transcription levels after gastrulation and the average difference in Z positions before and after gastrulation, which varies depending on the specific orientation each embryo was mounted. Each dot indicates an embryo from a collection of different Notch responsive enhancers, promoters and landing sites (n = 55 videos) All panels were btained by re-analyzing data from ***Falo-Sanjuan et al. 2019.***

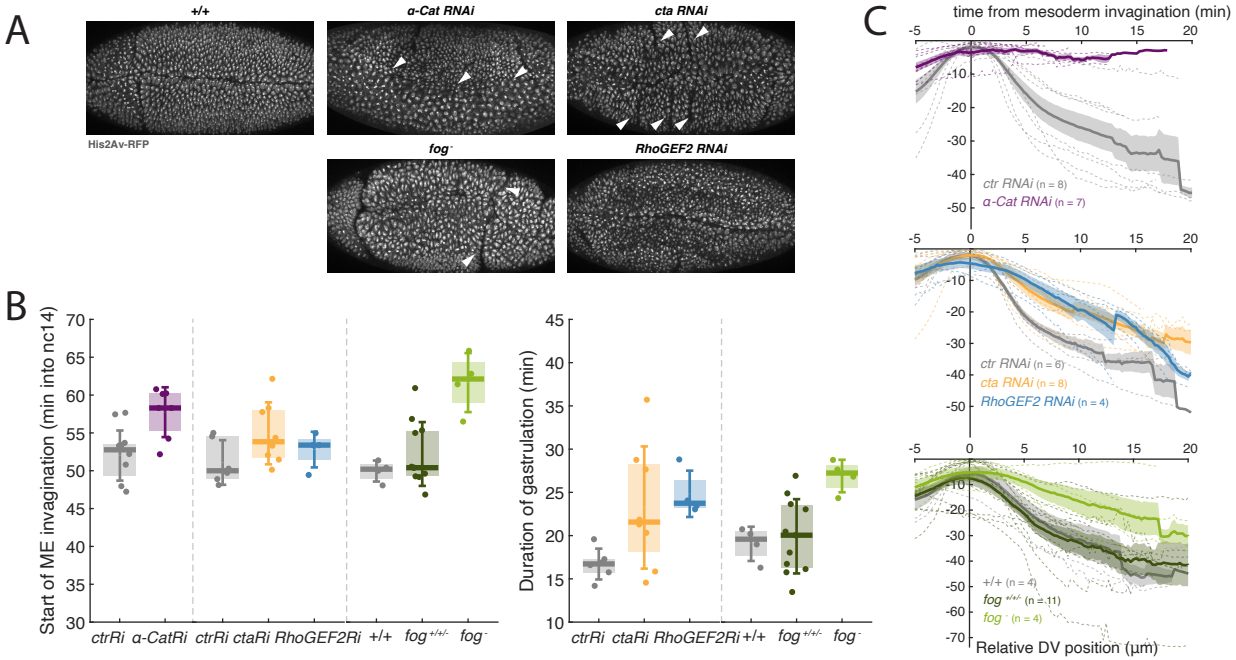

Figure 2 - supplement 1. Genetic disruption of gastrulation. **A**) Still images (maximum projection of the His2Av-RFP channel) of post-gastrulation embryos from the indicated genetic conditions captured after MS2 experiments. Arrowheads indicate ectopic folds and mesoderm cells dividing externally in *α-Cat* RNAi embryos. **B**) Start of ME invagination (left) and total gastrulation length (right) in the indicated genotypes. Boxplots show median, Q1/Q3 quartiles and SD. **C**) Quantification of the movement of MSE nuclei over time in the Y axis (representing movement in the DV axis), aligned by the time of ME invagination, in the indicated genetic conditions. 0 represents the highest (most dorsal) position achieved, therefore during gastrulation MSE nuclei move towards negative positions. Mean and SEM (solid line and shaded area) of multiple embryos shown (n embryo numbers indicated in each). Dashed lines indicate mean profiles for individual embryos. Because *α-Cat* RNAi embryos do not gastrulate, total duration of gastrulation was not quantified, and mesoderm invagination has been defined, based on the overall changes occurring in the embryo, as the time when it would normally initiate.

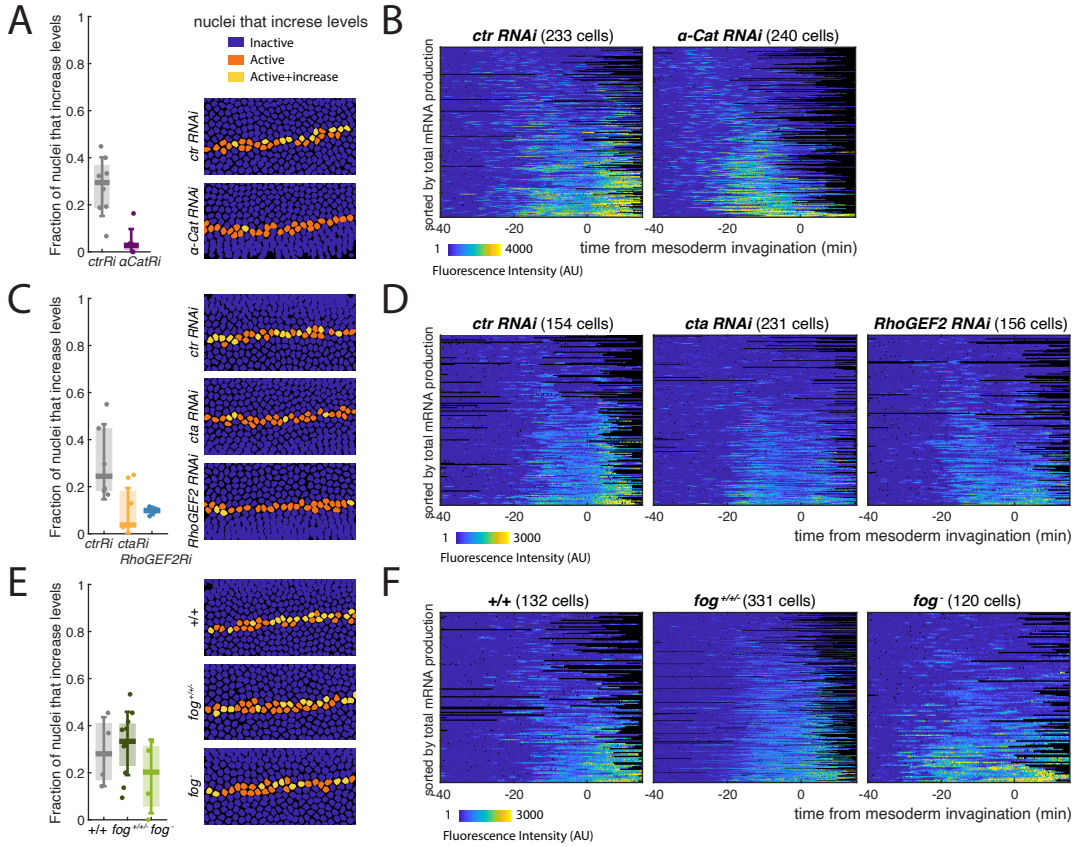

Figure 2 - supplement 2. Effects of genetic manipulations to gastrulation on the increase in *m5/m8* [II] transcription. ACE) Boxplots showing proportion of active cells in each embryo that increase levels of *m5/m8* [II] transcription at the time of gastrulation (left; median, Q1/Q3 and SD shown) and still frame with tracked nuclei color-coded for whether they increase in levels during gastrulation (right), in the indicated genetic conditions: *α-Cat* and control RNAi (**A**), *cta*, *RhoGEF2* and control RNAi (**C**) and *fog*$^{-}$ embryos compared to controls and other non fog hemizygous embryos obtained from the same cross - *fog*$^{+/+/-}$ (**E**). **BDF**) Heatmaps showing *m5/m8* [II] activity in all MSE cells over time, aligned by the time of ME invagination, in the indicated genetic conditions: *α-Cat* and control RNAi (**B**), *cta*, *RhoGEF2* and control RNAi (**D**) and *fog*$^{-}$ embryos compared to controls and other non fog hemizygous embryos obtained from the same cross - *fog*$^{+/+/-}$ (**F**).

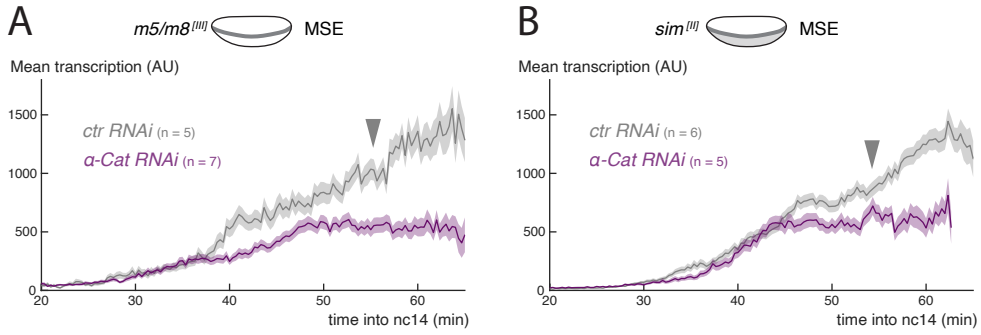

Figure 2 - supplement 3. Gastrulation also influences other Notch responsive enhancers. A) Mean profile of *m5/m8* [III] activity in *α-Cat* RNAi embryos compared to control embryos. **B**) Mean profile of *sim* [III] activity in *α-Cat* RNAi embryos compared to control embryos. Mean transcription profiles show mean and SEM (shaded area) of MS2 fluorescent traces from all cells combined from multiple embryos (n embryo numbers indicated in each).

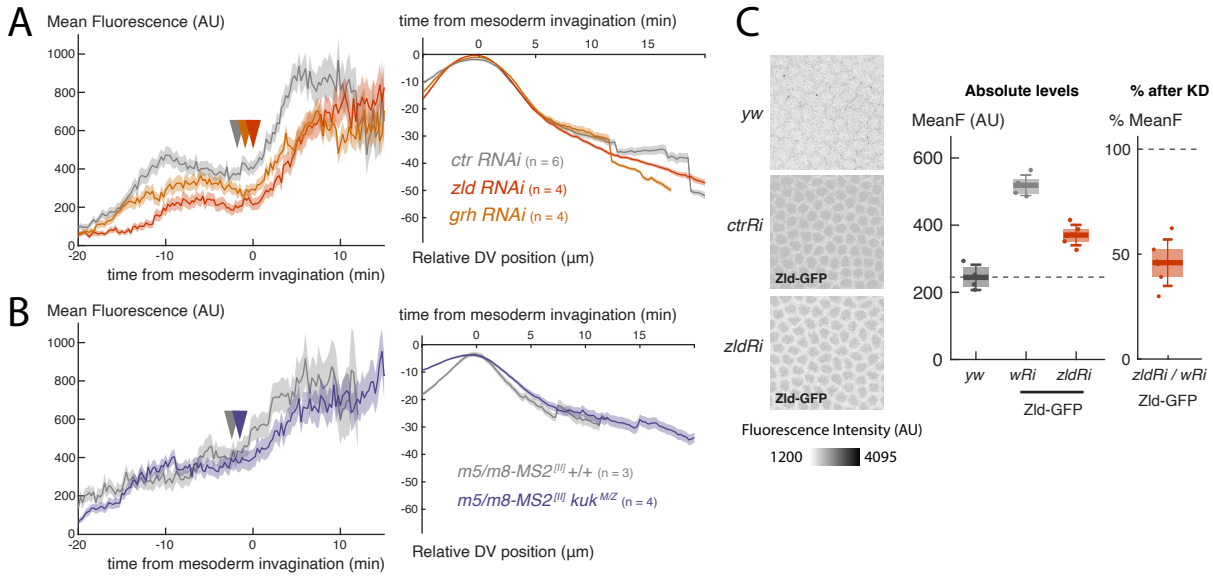

Figure 2 - supplement 4. Other genetic manipulations do not alter transcription profiles during gastrulation. **A**) Mean profile of *m5/m8* [II] activity (left) and movement of MSE nuclei over time in the Y axis (representing movement in the DV axis, right) in *zld* and *grh* RNAi embryos compared to control embryos. **B**) Mean profile of *m5/m8* [II] activity (left) and movement of MSE nuclei over time in the Y axis (representing movement in the DV axis, right) in *kuk* $^{M/Z}$ compared to control embryos. **C**) Quantification of the degree of maternal Zelda KD by quantifying *zld-GFP* fluorescence in embryos in the presence of control and *zld* RNAi. Mean transcription profiles show mean and SEM (shaded area) of MS2 fluorescent traces from all cells combined from multiple embryos (n embryo numbers indicated in each).

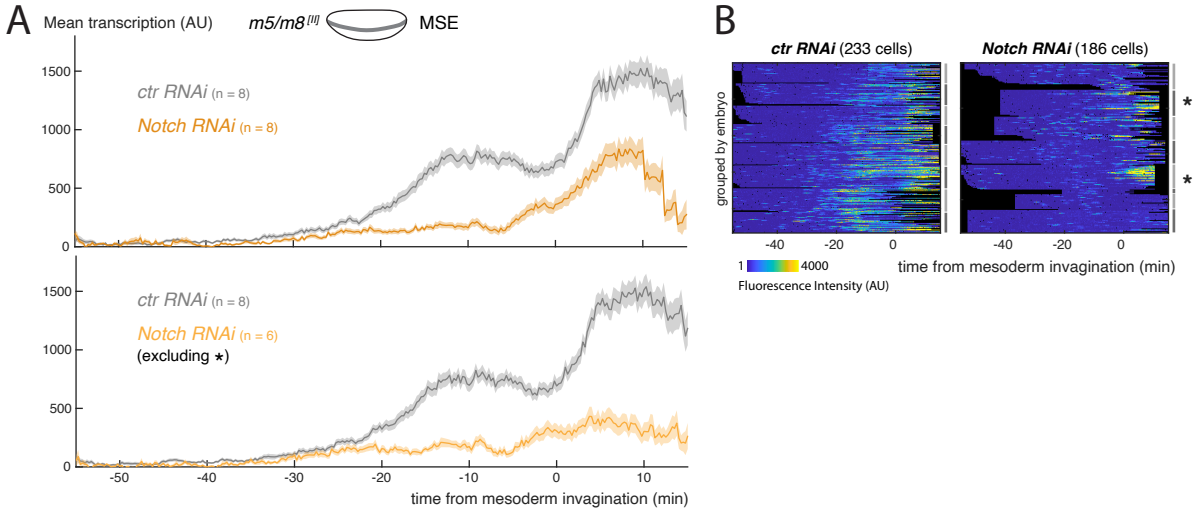

Figure 3 - supplement 1. ***Notch RNAi*** **strongly reduces Notch dependent transcription.** **A**) Mean profile of transcription from *m5/m8* [II] in *Notch RNAi* compared to control RNAi embryos considering all embryos (top) and after removing two embryos in which the levels Notch KD were likely lower (bottom), indicated by the asterisks in **B**. **B**) Heatmaps showing *m5/m8* [II] activity cells over time in *Notch* and control RNAi embryos. Traces have been grouped by embryo (each marked by grey and black lines on the sides) to highlight the degree of embryo-to-embryo variability in transcription, likely arising from differences in the degree of Notch KD. Mean transcription profiles show mean and SEM (shaded area) of MS2 fluorescent traces from all cells combined from multiple embryos (n embryo numbers indicated in each). Control embryos are the same as shown in Figure 2**B** and Figure 2 - supplement 2**B**.

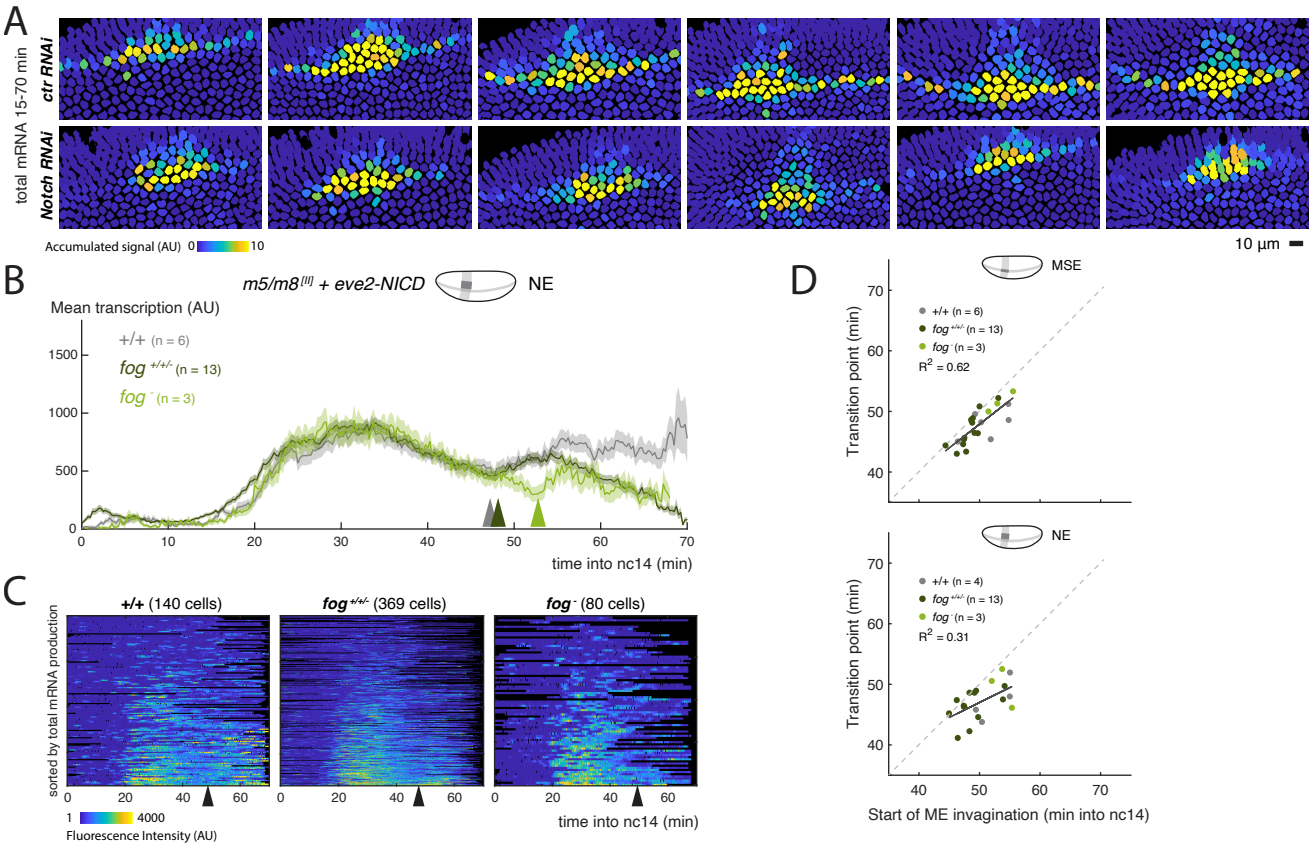

Figure 4 - supplement 1. Modulation of transcription occurs downstream of pathway activation. A) Still frames showing tracked nuclei color-coded for the total transcription produced by each nuclei in all *m5/m8* $^{[II]}$ + *eve2-NICD* control and *Notch RNAi* embryos. Upon Notch KD, *m5/m8* $^{[II]}$ transcription only occurs where *eve2-NICD* is expressed. **B**) Mean profile of transcription from *m5/m8* $^{[II]}$ in NE nuclei expressing ectopic NICD in *fog* mutant embryos compared to controls and to other embryos obtained from the same cross ($fog^{+/+/-}$). **C**) Heatmaps showing *m5/m8* $^{[II]}$ activity over time in all NE cells expressing ectopic NICD in fog^{-} embryos compared to controls and to other embryos obtained from the same cross ($fog^{+/+/-}$). **D**) Correlation between start of invagination and transition in *m5/m8* $^{[II]}$ transcription levels in MSE (top) or NE (bottom) nuclei overlapping with *eve2-NICD* domain in each *fog* mutant embryo compared to control and other non *fog* hemizygous embryos obtained from the same cross. Mean transcription profiles show mean and SEM (shaded area) of MS2 fluorescent traces from all cells combined from multiple embryos (n embryo numbers indicated in each). R^2 coefficients in **D** are calculated after pooling all points shown the same plot together. The transition point was only considered when a clear change in mean levels of transcription in an individual embryo could be observed, therefore the number of points could be smaller than the total number of embryos collected for each condition.

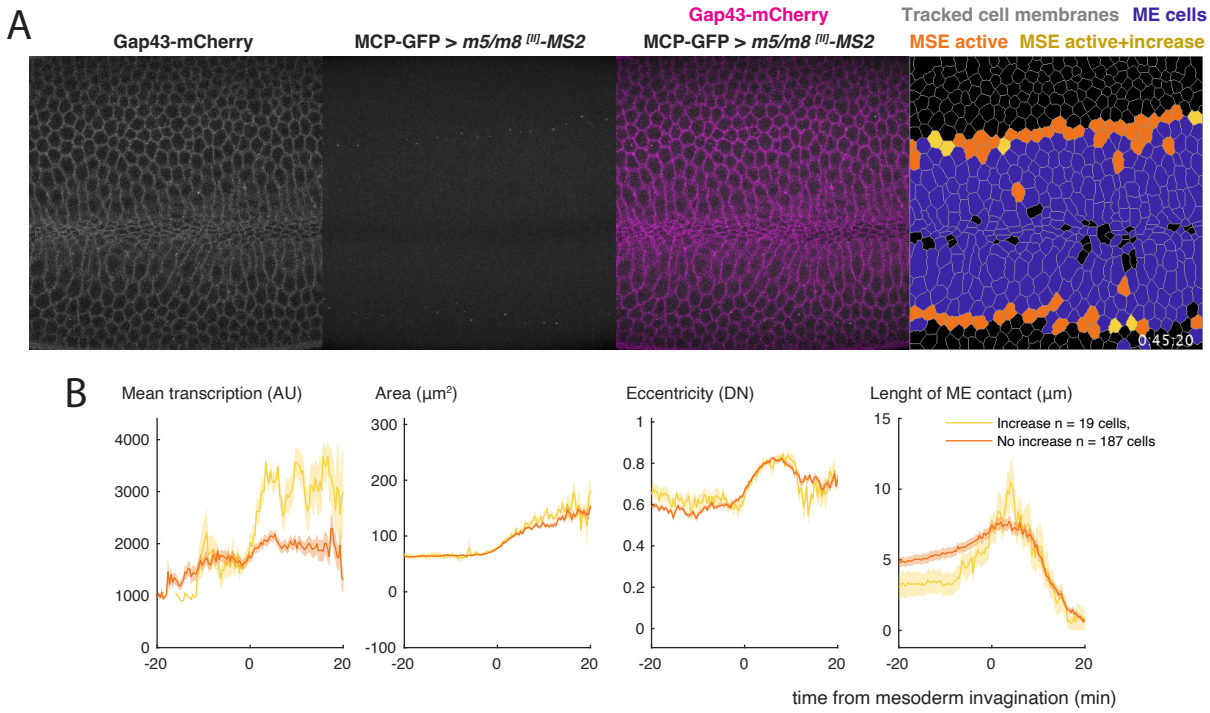

Figure 5 - supplement 1. Changes in cellular morphology during gastrulation do not correlate with cells that increase transcription levels or not. A) Still image of a video of an embryo expressing Gap43-mCherry to label cell membranes and MCP-GFP to detect *m5/m8* ^{II} transcription. From left to right: (i) Projection of 3 µm of the Gap43-mCh channel, (ii) Projection of the whole MCP-GFP channel, (iii) overlay of i in magenta and ii in grey, (iv) tracked cell membranes and cells color coded to indicate mesoderm (purple), active mesectoderm nuclei that increase transcription levels (yellow) and active mesectoderm nuclei that do not increase transcription levels (orange). **B**) Quantification of cellular properties of mesectoderm cells over time grouped by whether they increase transcription levels at the time of gastrulation or not. From left to right: (i) transcription detected in the MCP channel, (ii) cell area, (iii) eccentricity from 0 - fully circular - to 1 - straight line, (iv) length of contact of each mesectoderm cell with mesoderm cells around them. DN: dimensionless number. n = 3 embryos.

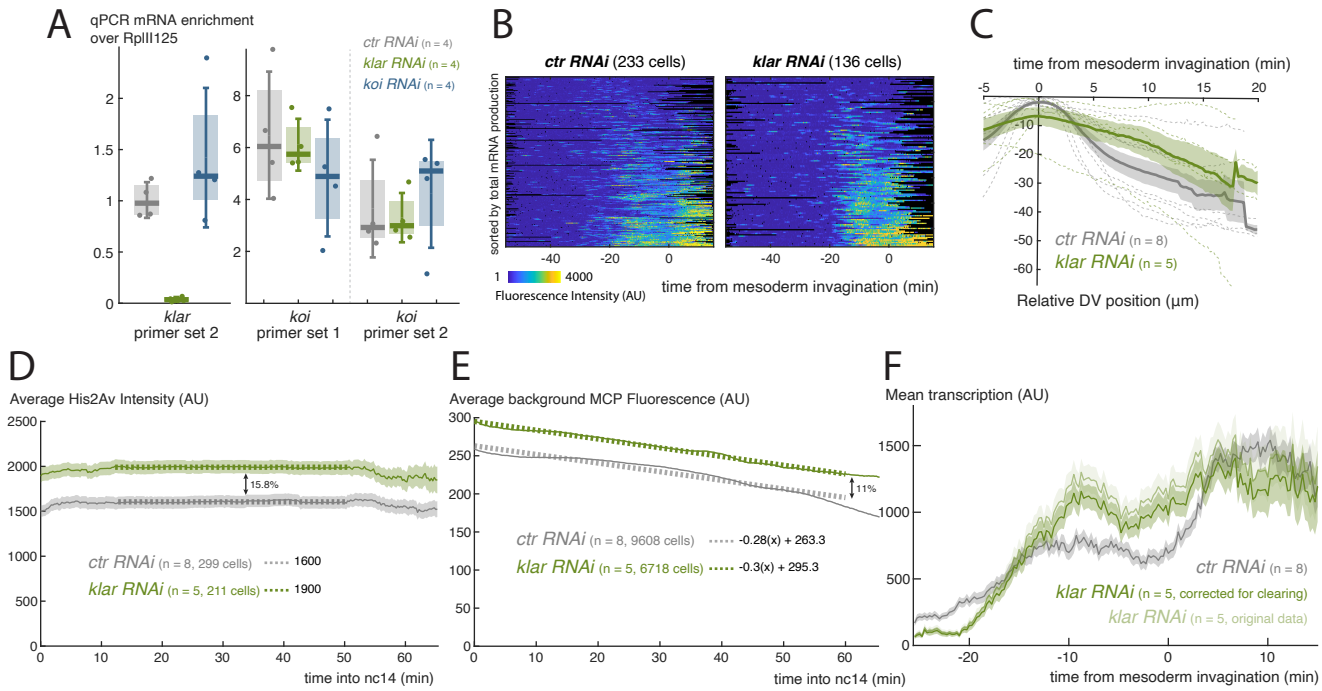

Figure 5 - supplement 2. LINC complex disruption decouples gastrulation progression and changes in transcription. **A**) Quantification of *klar* and *koi* mRNA levels by RT-qPCR in pools of 15-20 eggs and/or pre nc13 embryos following control, *klar* or *koi* germline RNAi expression. n = 4 biological replicates for each. **B**) Heatmaps with *m5/m8* [II] activity, aligned by the time of ME invagination, in *klar* and control RNAi embryos. **C**) Movement of MSE nuclei over time in the Y axis (representing movement in the DV axis), aligned by the time of ME invagination, in *klar* and control RNAi embryos. Mean and SEM (solid line and shaded area) of multiple embryos shown (n embryo numbers indicated in each). Dashed lines indicate mean profiles for individual embryos. **D**) Average His2Av-RFP intensity over time in control and *klar RNAi* embryos. **E**) Average MCP-GFP intensity in nuclei without any MS2 signal over time in control and *klar RNAi* embryos. **F**) Mean profile of transcription from m5/m8 [II] in control and klar RNAi embryos, before and after correction for increased clearing. Control embryos are the same as shown in Figure 2 - supplement 2**B** and Figure 2 - supplement 1**C**.

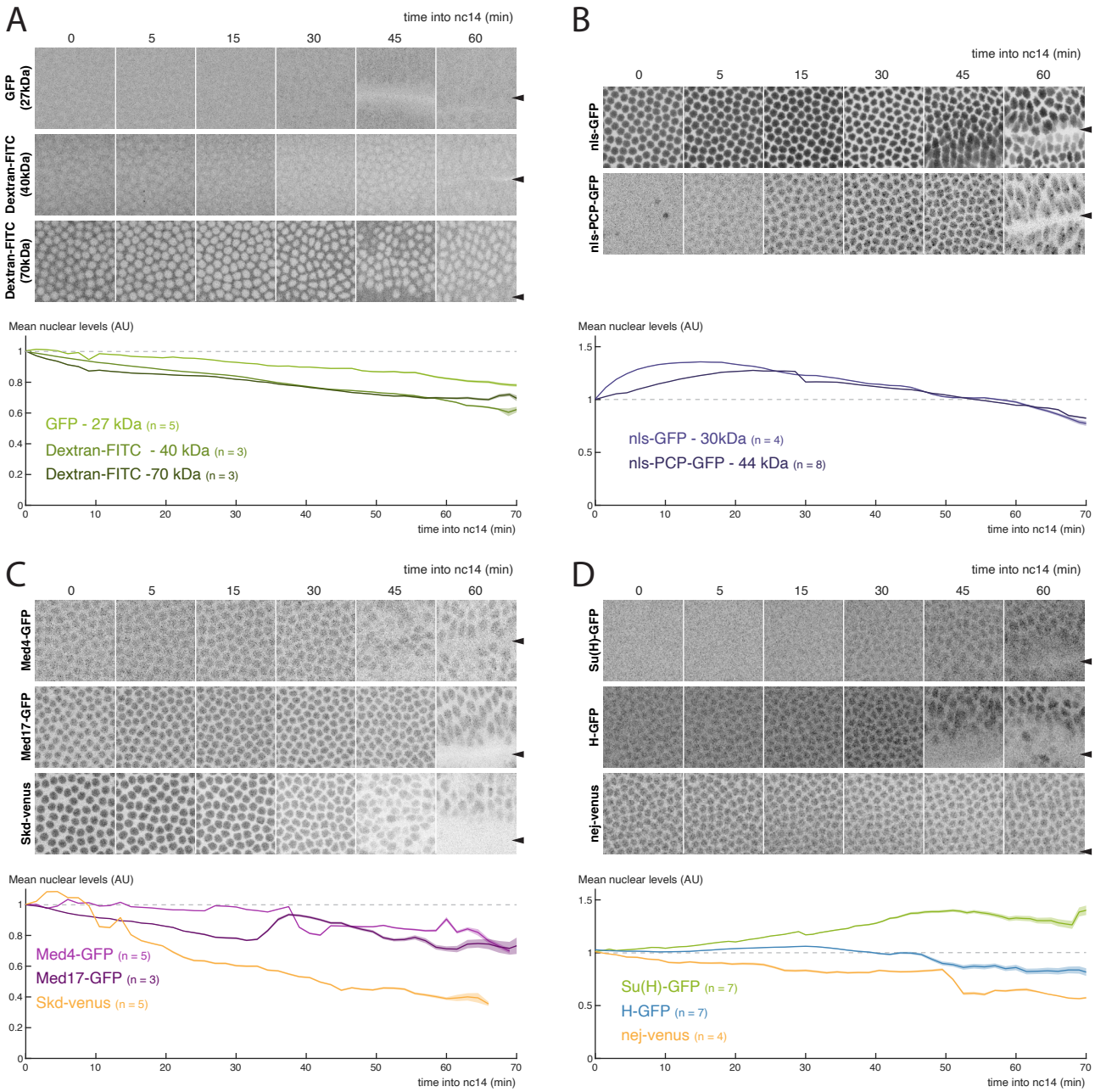

Figure 6 - supplement 1. Nuclear import does not change during gastrulation. Nuclear levels of GFP and fluorescently-tagged dextrans (**A**), nls-containing proteins (**B**), members of the mediator complex (**C**) and regulators of Notch signalling (**D**) during gastrulation. In each panel, top half shows still from videos of the fluorescent factor quantified in each condition (inverted maximum intensity projection). Arrowheads indicate position of the mesoderm invagination furrow. Bottom half shows quantification of the nuclear levels over time, showing mean and SEM (shaded area) of all cells combined from multiple embryos (n numbers shown in each).

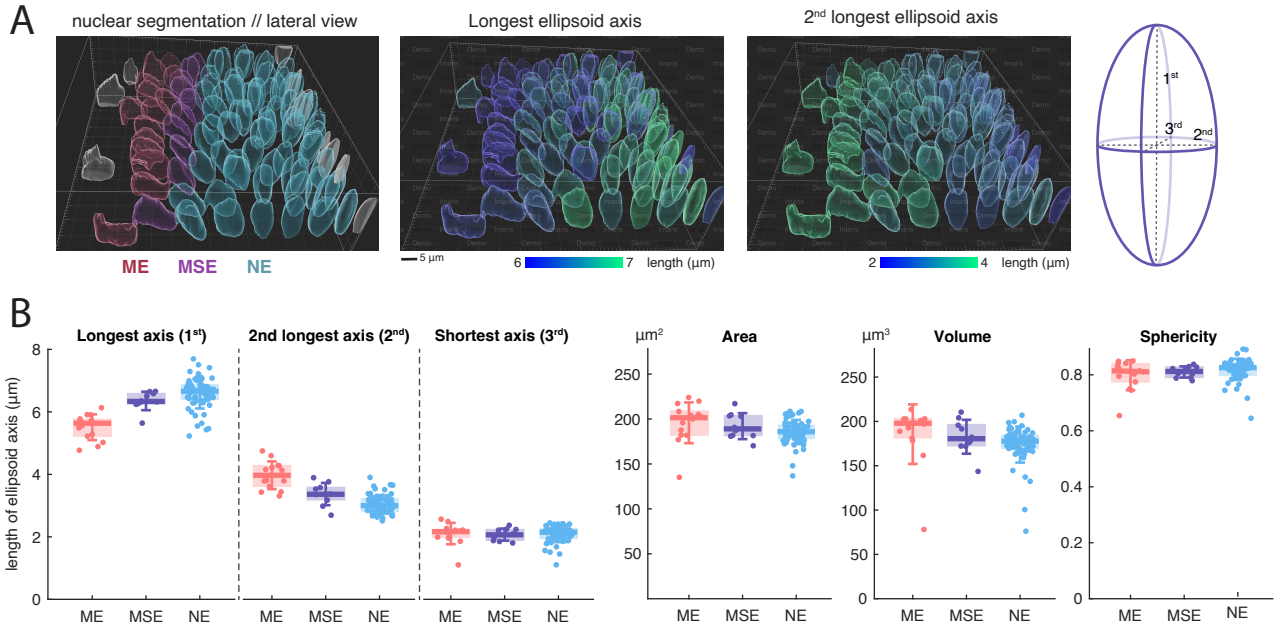

Figure 6 - supplement 2. Quantification of nuclear size and shape during gastrulation. A) Lateral view of segmented nuclei color-coded based on the different cell populations defined from MS2 signal (ME: mesoderm, MSE: mesectoderm, NE: neuroectoderm, left) and color-coded by length of the longest ellipsoid axis (middle) and 2nd longest axis (right). **B**) Quantification of morphological properties of ME, MSE and NE nuclei at the start of mesoderm invagination. Boxplots show median, Q1/Q3 quartiles and SD.

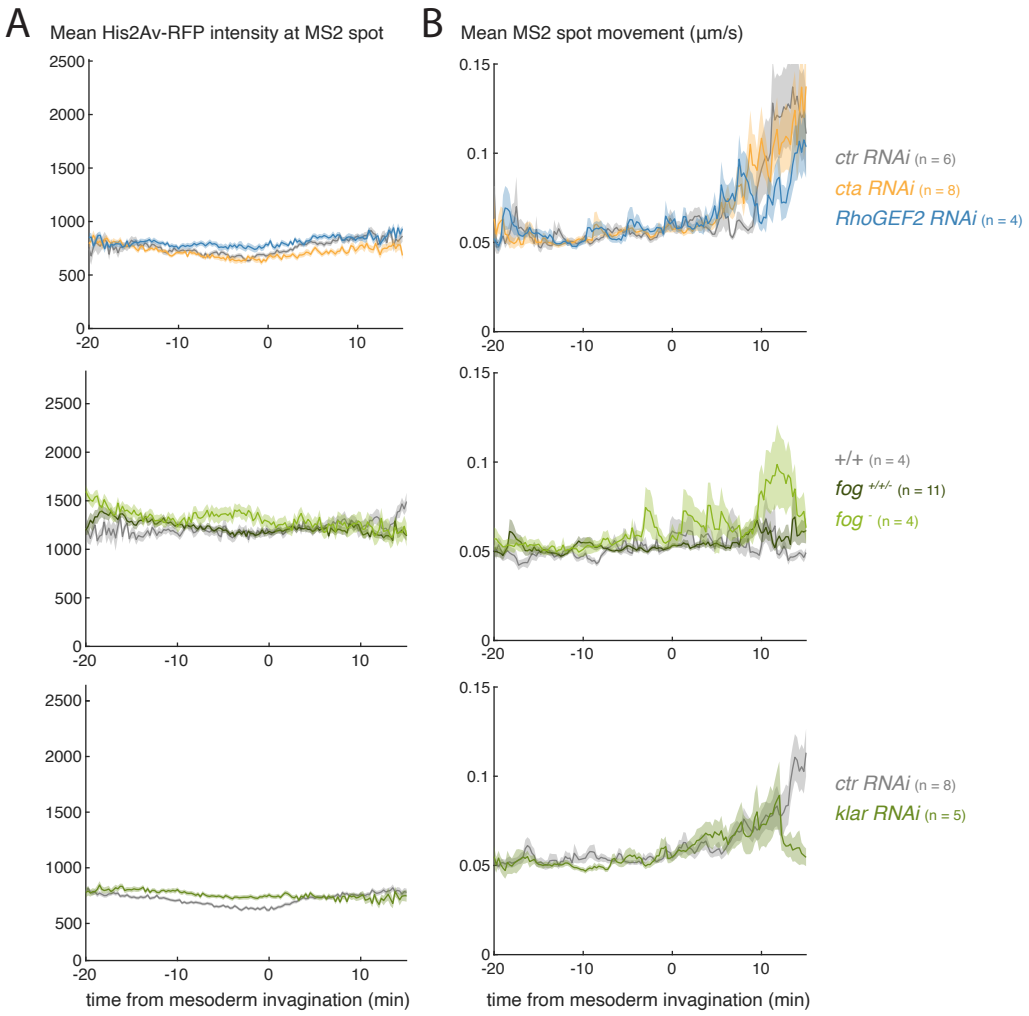

Figure 6 - supplement 3. Quantification of chromatin properties during gastrulation. A) Quantification of average His2Av-RFP intensity around the MS2 spot, as a proxy of chromatin compaction, over time in the indicated genetic conditions. **B**) Quantification of the average MS2 spot movement (distance moved relative to the nucleus centroid / time) over time in in the indicated genetic conditions. Mean and SEM (solid line and shaded area) of multiple embryos shown (n embryo numbers indicated in each). In **B**, values were smoothed over time using a median filter of 8 frames (2 minutes).

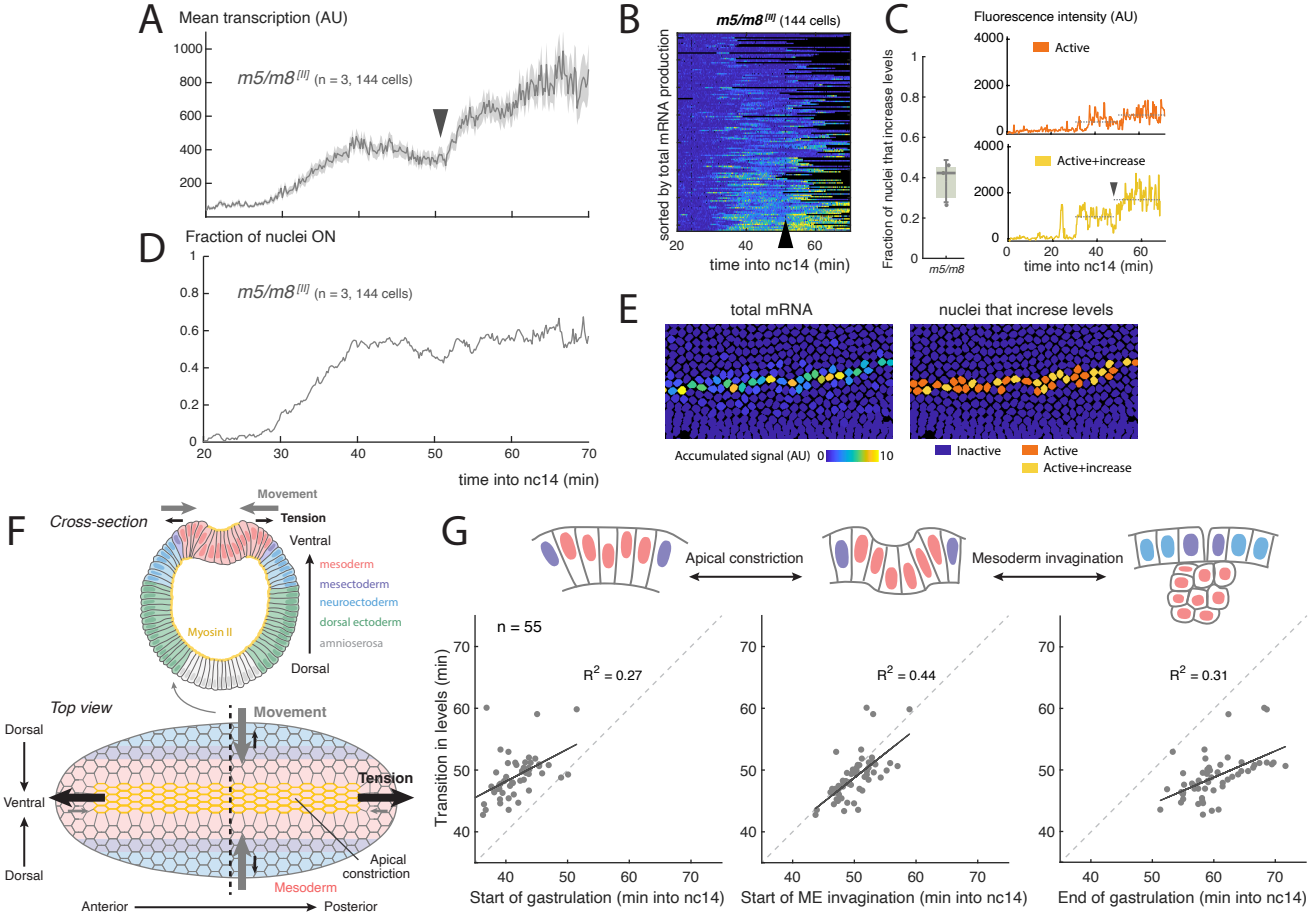
A
Mean transcription (AU)
m5/m8[II] (n = 3, 144 cells)
B
m5/m8[II] (144 cells)
sorted by total mRNA production
time into nc14 (min)
C
Fraction of nuclei that increase levels
m5/m8
Fluorescence intensity (AU)
Active
Active+increase
time into nc14 (min)
D
Fraction of nuclei ON
m5/m8[II] (n = 3, 144 cells)
time into nc14 (min)
E
total mRNA
nuclei that increse levels
Accumulated signal (AU) 0 10
Inactive
Active
Active+increase
F
Cross-section
Movement
Tension
Ventral
mesoderm
mesectoderm
neuroectoderm
dorsal ectoderm
amnioserosa
Myosin II
Dorsal
Top view
Movement
Dorsal
Ventral
Dorsal
Tension
Apical constriction
Mesoderm
Anterior
Posterior
G
Apical constriction
Mesoderm invagination
n = 55
R2 = 0.27
R2 = 0.44
R2 = 0.31
Transition in levels (min)
Start of gastrulation (min into nc14)
Start of ME invagination (min into nc14)
End of gastrulation (min into nc14)

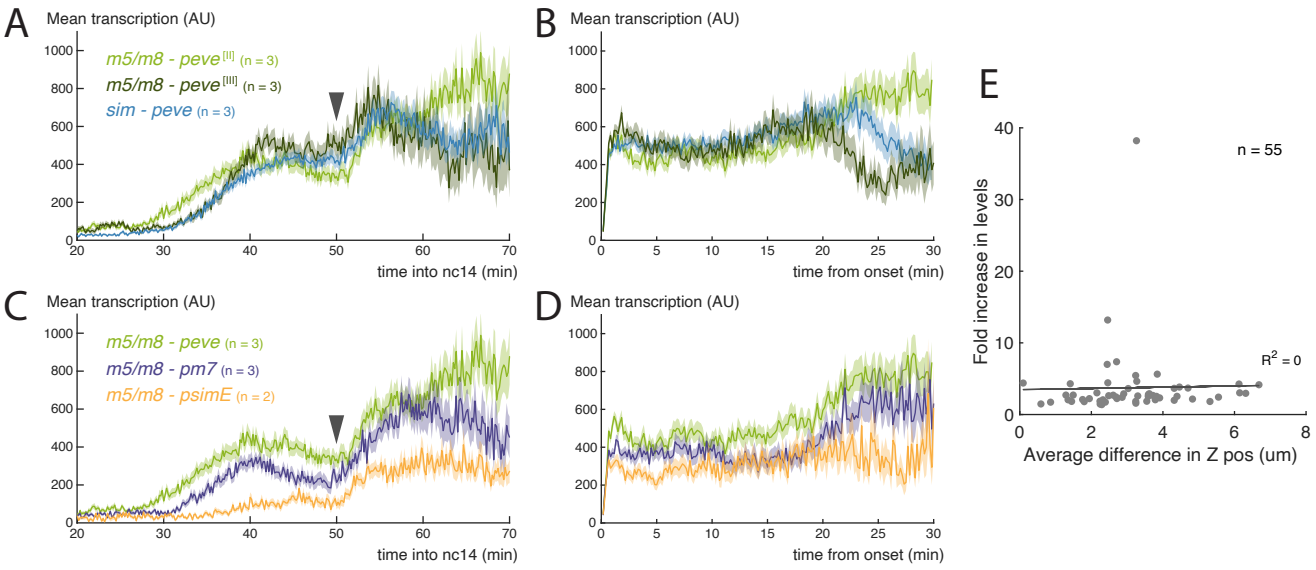
A
Mean transcription (AU)
m5/m8 - peve[II] (n = 3)
m5/m8 - peve[III] (n = 3)
sim - peve (n = 3)
time into nc14 (min)
B
Mean transcription (AU)
time from onset (min)
C
Mean transcription (AU)
m5/m8 - peve (n = 3)
m5/m8 - pm7 (n = 3)
m5/m8 - psimE (n = 2)
time into nc14 (min)
D
Mean transcription (AU)
time from onset (min)
E
n = 55
R2 = 0
Fold increase in levels
Average difference in Z pos (um)

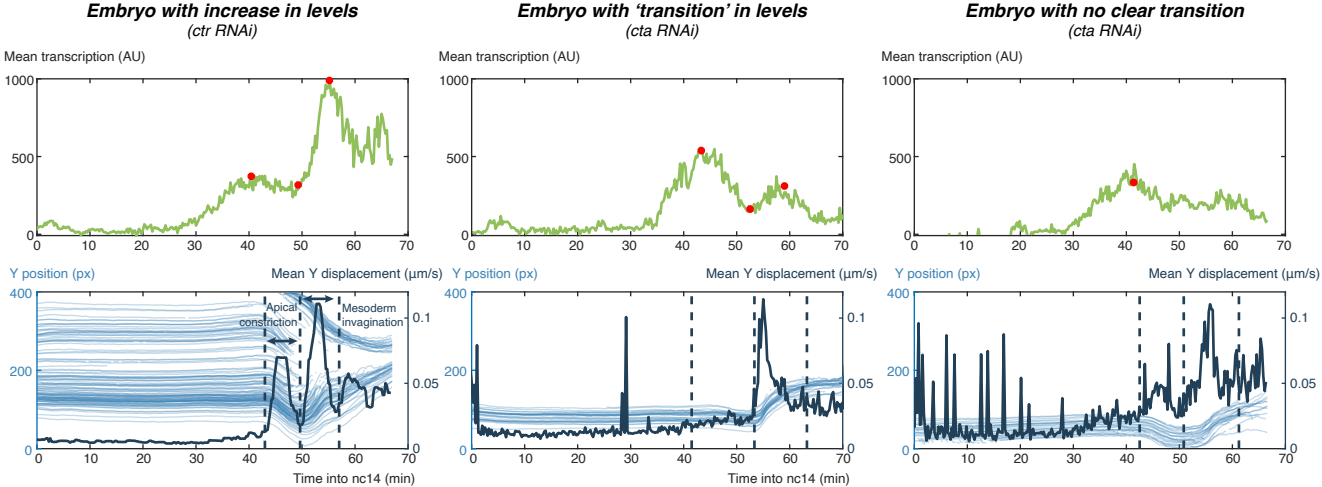
Embryo with increase in levels
(ctr RNAi)
Embryo with 'transition' in levels
(cta RNAi)
Embryo with no clear transition
(cta RNAi)
Mean transcription (AU)
Y position (px)
Mean Y displacement (µm/s)
Apical constriction
Mesoderm invagination
Time into nc14 (min)

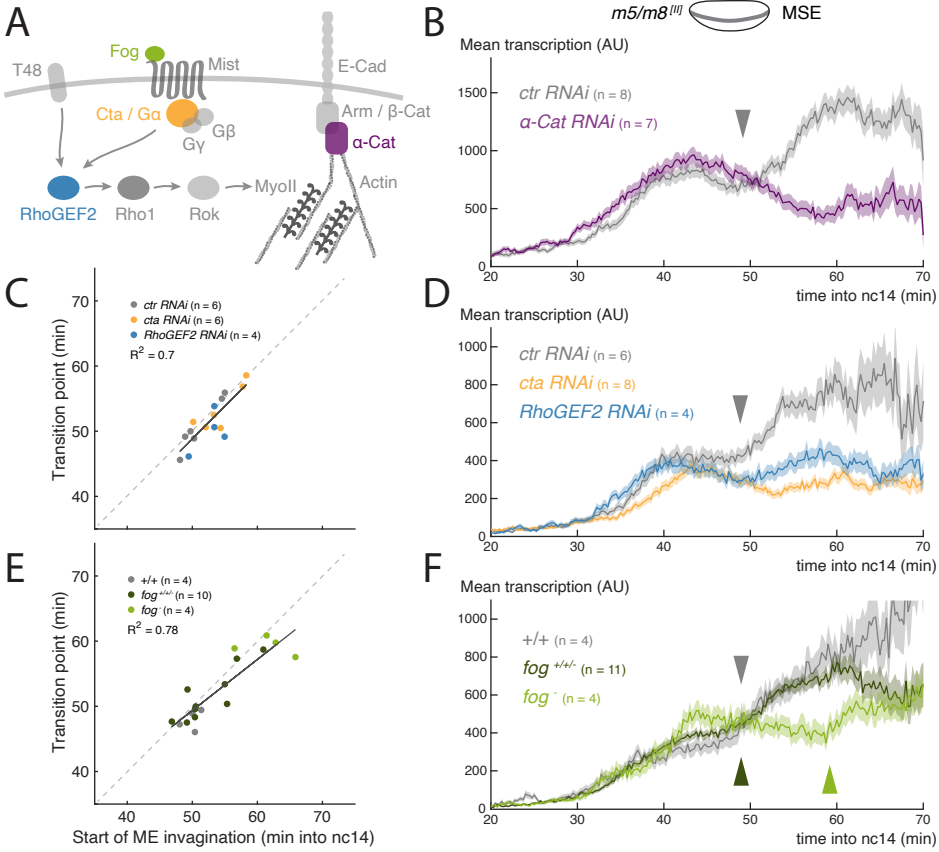
A
Fog
T48
Mist
E-Cad
Cta / Gα
Gβ
Gγ
Arm / β-Cat
α-Cat
Actin
MyoII
RhoGEF2
Rho1
Rok
B
m5/m8[II]
MSE
Mean transcription (AU)
ctr RNAi (n = 8)
α-Cat RNAi (n = 7)
time into nc14 (min)
C
ctr RNAi (n = 6)
cta RNAi (n = 6)
RhoGEF2 RNAi (n = 4)
R2 = 0.7
Transition point (min)
D
Mean transcription (AU)
ctr RNAi (n = 6)
cta RNAi (n = 8)
RhoGEF2 RNAi (n = 4)
time into nc14 (min)
E
+/+ (n = 4)
fog+/+/- (n = 10)
fog- (n = 4)
R2 = 0.78
Transition point (min)
Start of ME invagination (min into nc14)
F
Mean transcription (AU)
+/+ (n = 4)
fog +/+/- (n = 11)
fog - (n = 4)
time into nc14 (min)

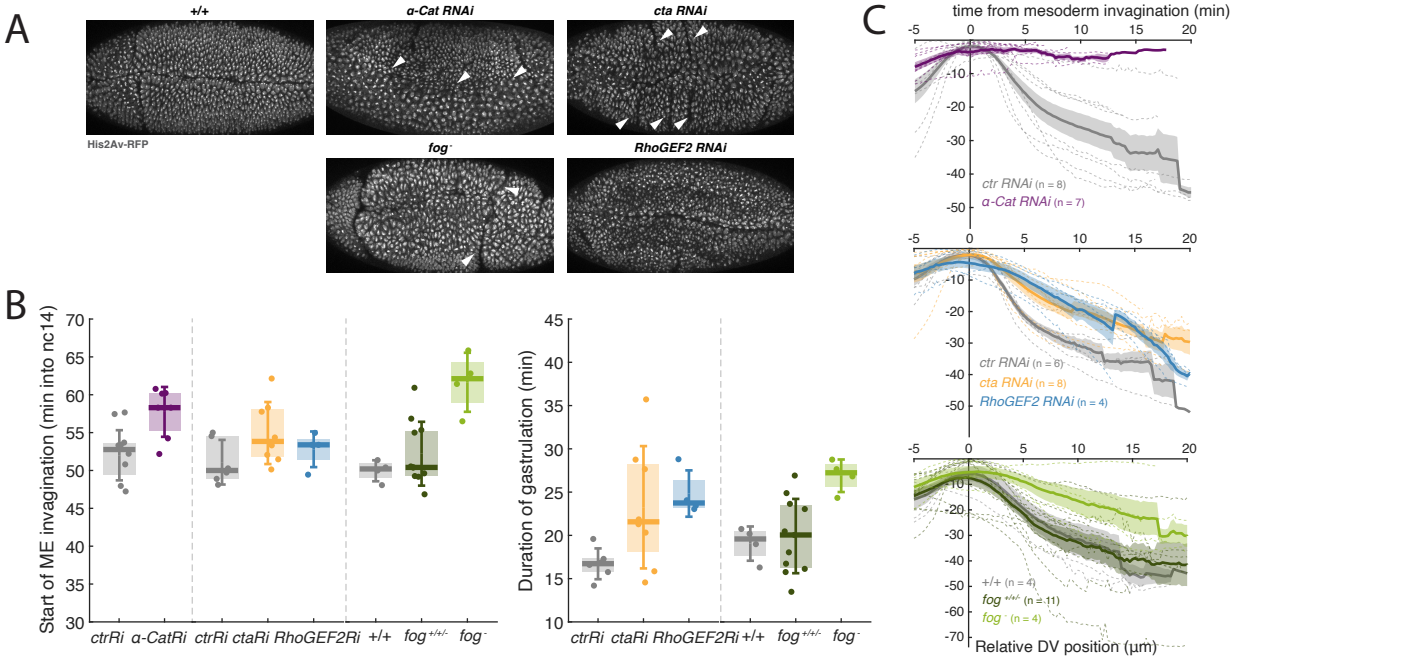
A
+/+
α-Cat RNAi
cta RNAi
His2Av-RFP
fog-
RhoGEF2 RNAi
B
Start of ME invagination (min into nc14)
ctrRi α-CatRi ctrRi ctaRi RhoGEF2Ri +/+ fog+/+/- fog-
Duration of gastrulation (min)
ctrRi ctaRi RhoGEF2Ri +/+ fog+/+/- fog-
C
time from mesoderm invagination (min)
ctr RNAi (n = 8)
α-Cat RNAi (n = 7)
ctr RNAi (n = 8)
cta RNAi (n = 8)
RhoGEF2 RNAi (n = 4)
+/+ (n = 4)
fog+/+/- (n = 11)
fog- (n = 4)
Relative DV position (μm)

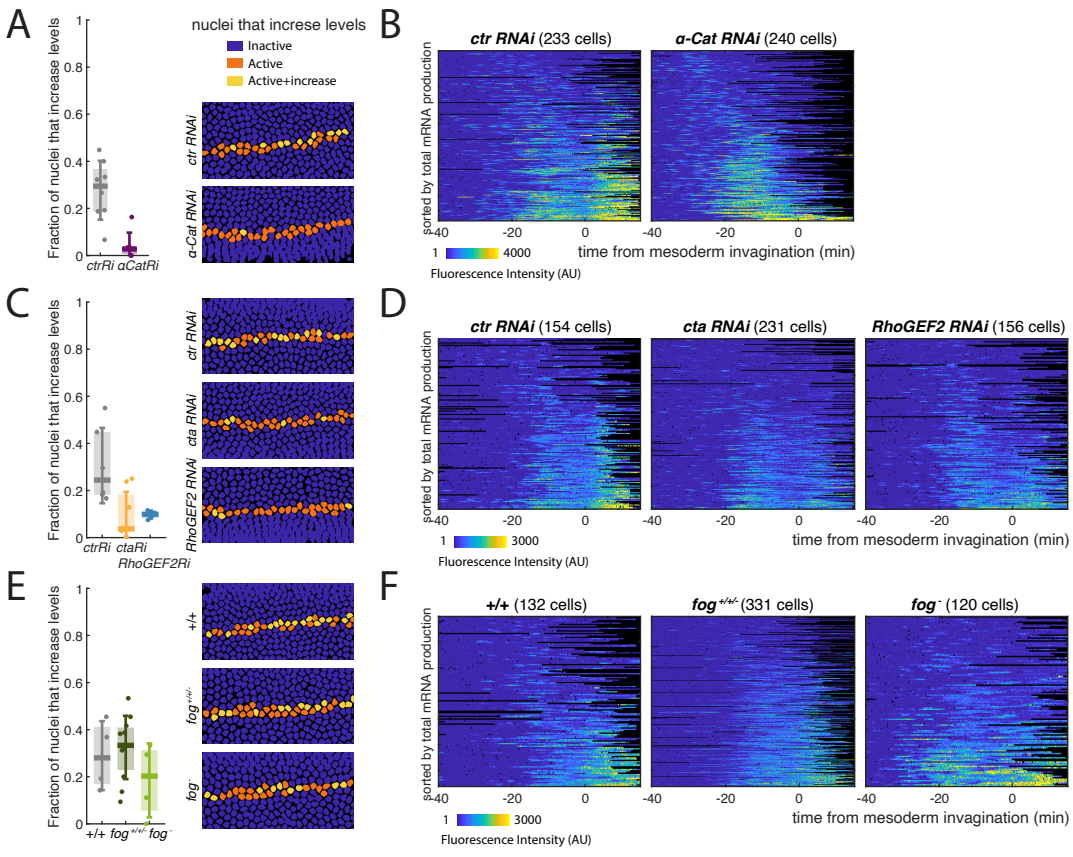
A
nuclei that increse levels
Inactive
Active
Active+increase
Fraction of nuclei that increase levels
ctrRi
aCatRi
ctr RNAi
α-Cat RNAi
B
ctr RNAi (233 cells)
α-Cat RNAi (240 cells)
sorted by total mRNA production
time from mesoderm invagination (min)
Fluorescence Intensity (AU)
C
ctaRi
RhoGEF2Ri
cta RNAi
RhoGEF2 RNAi
D
ctr RNAi (154 cells)
cta RNAi (231 cells)
RhoGEF2 RNAi (156 cells)
E
+/+
fog+/-
fog-
F
+/+ (132 cells)
fog+/- (331 cells)
fog- (120 cells)

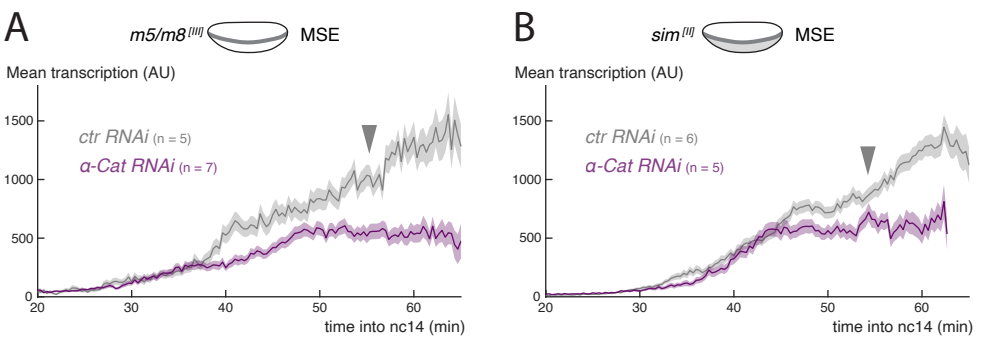
A
m5/m8[III]
MSE
Mean transcription (AU)
1500
1000
500
0
ctr RNAi (n = 5)
α-Cat RNAi (n = 7)
20
30
40
50
60
time into nc14 (min)
B
sim[III]
MSE
Mean transcription (AU)
1500
1000
500
0
ctr RNAi (n = 6)
α-Cat RNAi (n = 5)
20
30
40
50
60
time into nc14 (min)

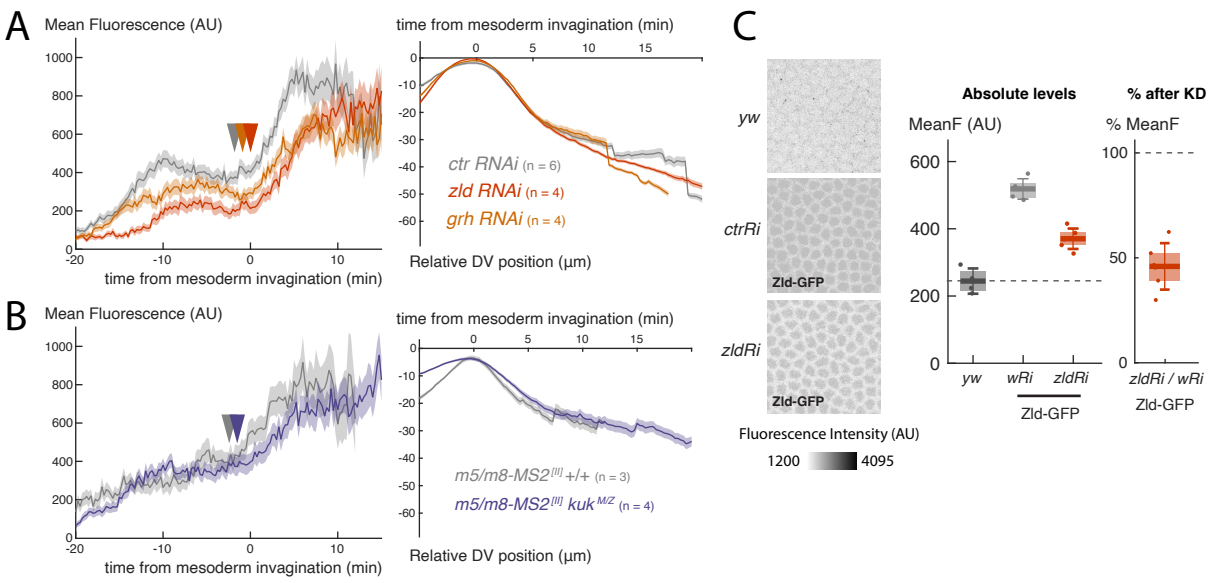
A
Mean Fluorescence (AU)
time from mesoderm invagination (min)
time from mesoderm invagination (min)
ctr RNAi (n = 6)
zld RNAi (n = 4)
grh RNAi (n = 4)
Relative DV position (µm)
B
Mean Fluorescence (AU)
time from mesoderm invagination (min)
time from mesoderm invagination (min)
m5/m8-MS2[II] +/+ (n = 3)
m5/m8-MS2[II] kuk M/Z (n = 4)
Relative DV position (µm)
C
yw
ctrRi
zldRi
Zld-GFP
Zld-GFP
Zld-GFP
Fluorescence Intensity (AU)
1200
4095
Absolute levels
% after KD
MeanF (AU)
% MeanF
yw
wRi
zldRi
Zld-GFP
zldRi / wRi
Zld-GFP

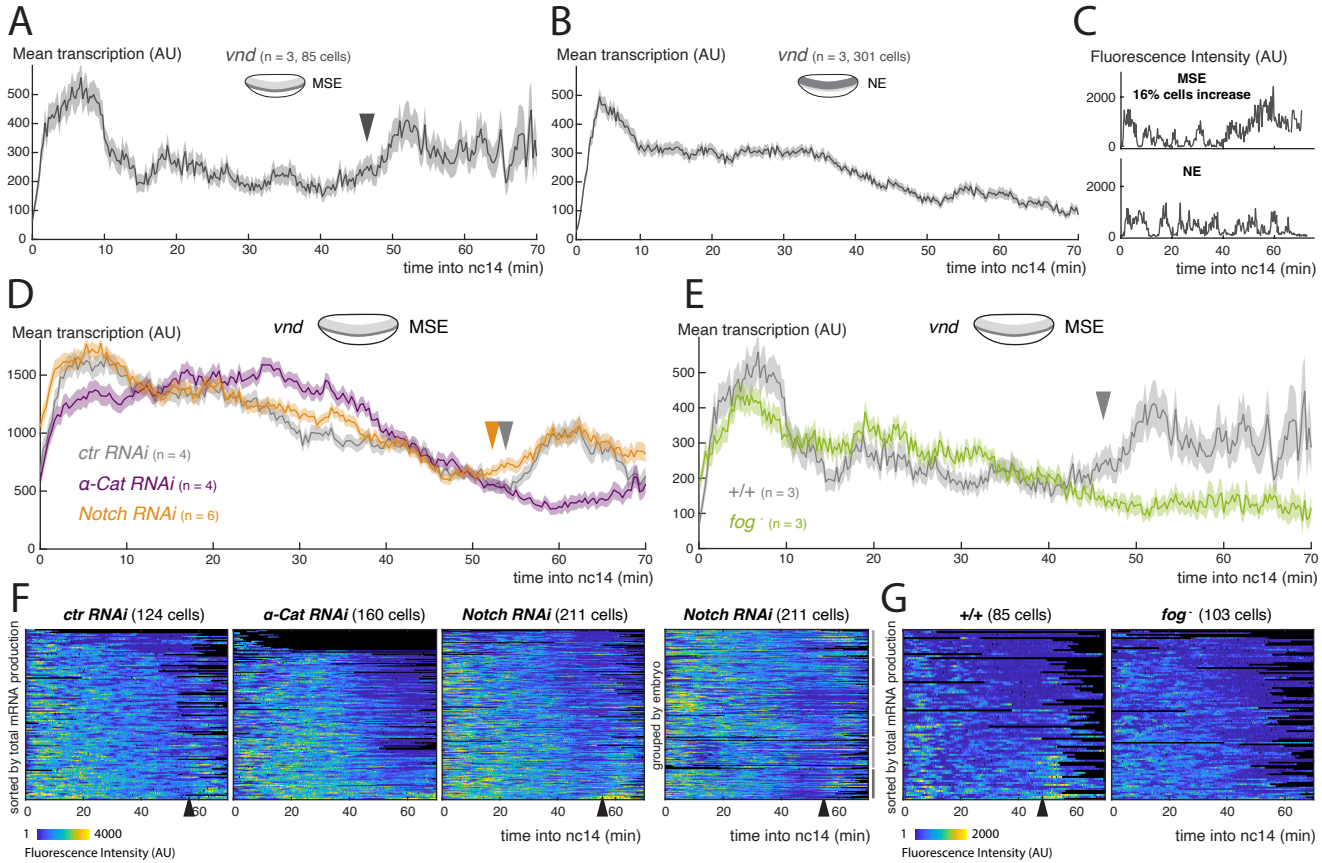
A
Mean transcription (AU)
vnd (n = 3, 85 cells)
MSE
time into nc14 (min)
B
Mean transcription (AU)
vnd (n = 3, 301 cells)
NE
time into nc14 (min)
C
Fluorescence Intensity (AU)
MSE
16% cells increase
NE
time into nc14 (min)
D
Mean transcription (AU)
vnd
MSE
ctr RNAi (n = 4)
α-Cat RNAi (n = 4)
Notch RNAi (n = 6)
time into nc14 (min)
E
Mean transcription (AU)
vnd
MSE
+/+ (n = 3)
fog⁻ (n = 3)
time into nc14 (min)
F
ctr RNAi (124 cells)
α-Cat RNAi (160 cells)
Notch RNAi (211 cells)
Notch RNAi (211 cells)
sorted by total mRNA production
grouped by embryo
time into nc14 (min)
Fluorescence Intensity (AU)
G
+/+ (85 cells)
fog⁻ (103 cells)
sorted by total mRNA production
time into nc14 (min)
Fluorescence Intensity (AU)

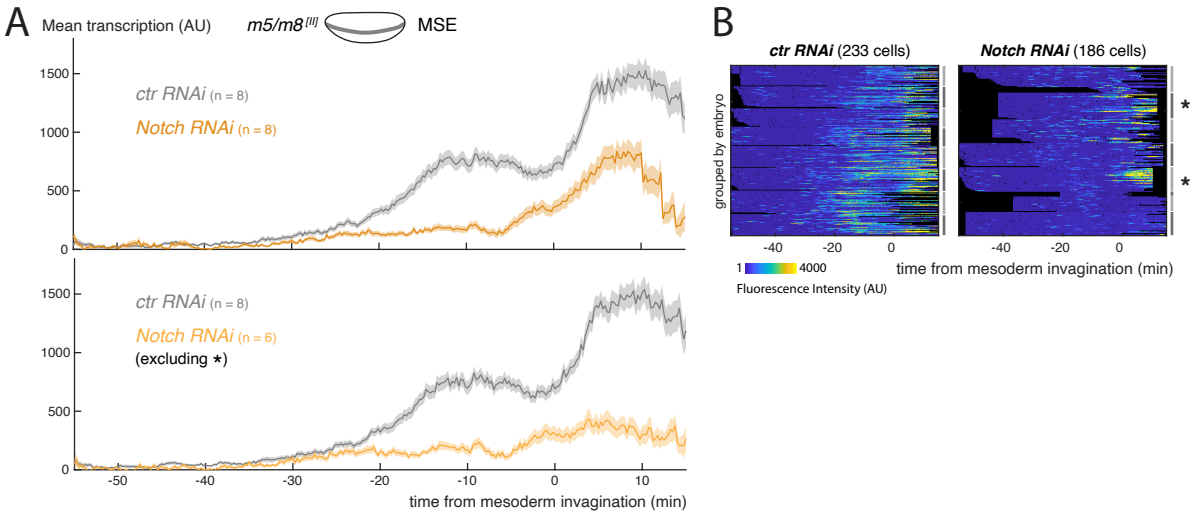
A
Mean transcription (AU)
m5/m8[III]
MSE
1500
1000
500
0
ctr RNAi (n = 8)
Notch RNAi (n = 8)
ctr RNAi (n = 8)
Notch RNAi (n = 6)
(excluding *)
-50
-40
-30
-20
-10
0
10
time from mesoderm invagination (min)
B
ctr RNAi (233 cells)
Notch RNAi (186 cells)
grouped by embryo
*
*
-40
-20
0
1
4000
Fluorescence Intensity (AU)
time from mesoderm invagination (min)

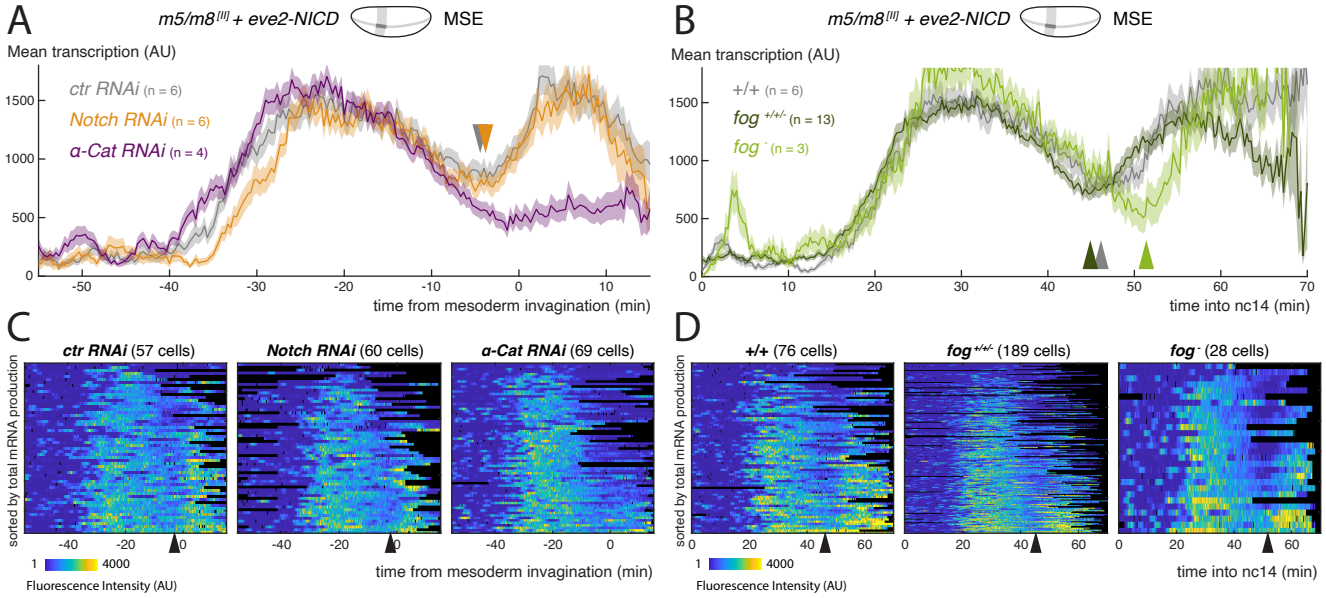
A
m5/m8[II] + eve2-NICD
MSE
Mean transcription (AU)
ctr RNAi (n = 6)
Notch RNAi (n = 6)
α-Cat RNAi (n = 4)
time from mesoderm invagination (min)
B
m5/m8[II] + eve2-NICD
MSE
Mean transcription (AU)
+/+ (n = 6)
fog +/+/- (n = 13)
fog - (n = 3)
time into nc14 (min)
C
ctr RNAi (57 cells)
Notch RNAi (60 cells)
α-Cat RNAi (69 cells)
sorted by total mRNA production
time from mesoderm invagination (min)
Fluorescence Intensity (AU)
D
+/+ (76 cells)
fog +/+/- (189 cells)
fog - (28 cells)
sorted by total mRNA production
time into nc14 (min)
Fluorescence Intensity (AU)

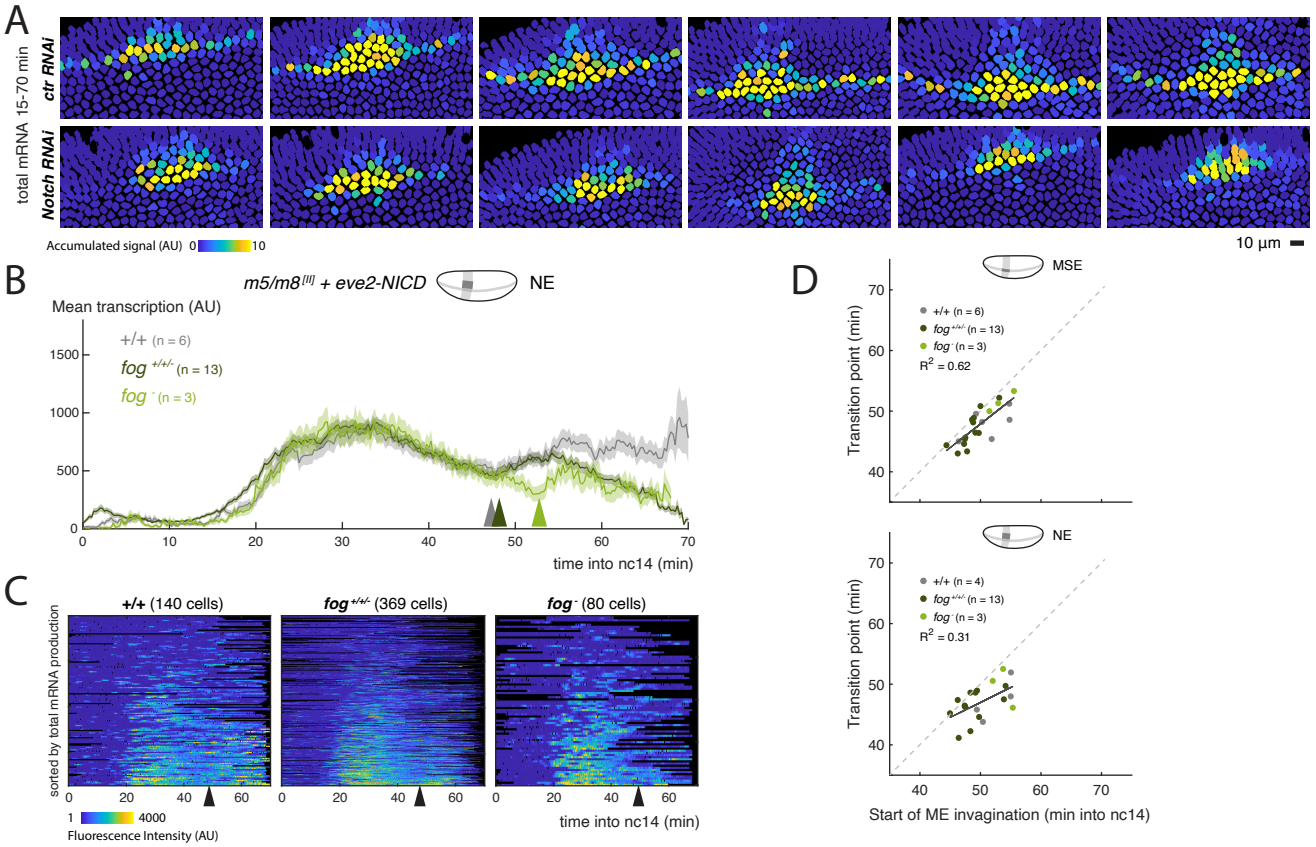
A
total mRNA 15-70 min
ctr RNAi
Notch RNAi
Accumulated signal (AU) 0 10
10 µm
B
m5/m8[II] + eve2-NICD
NE
Mean transcription (AU)
+/+ (n = 6)
fog +/+/- (n = 13)
fog - (n = 3)
time into nc14 (min)
C
+/+ (140 cells)
fog +/+/- (369 cells)
fog - (80 cells)
sorted by total mRNA production
1 4000
Fluorescence Intensity (AU)
time into nc14 (min)
D
MSE
NE
Transition point (min)
+/+ (n = 6)
fog +/+/- (n = 13)
fog - (n = 3)
R2 = 0.62
+/+ (n = 4)
R2 = 0.31
Start of ME invagination (min into nc14)

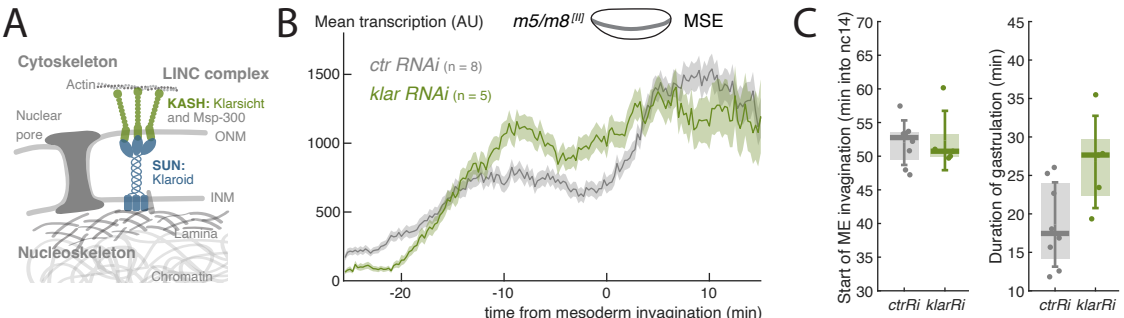
A
Cytoskeleton
Actin
LINC complex
KASH: Klarsicht and Msp-300
Nuclear pore
ONM
SUN: Klaroid
INM
Lamina
Nucleoskeleton
Chromatin
B
Mean transcription (AU)
m5/m8[II]
MSE
ctr RNAi (n = 8)
klar RNAi (n = 5)
1500
1000
500
0
-20
-10
0
10
time from mesoderm invagination (min)
C
Start of ME invagination (min into nc14)
70
65
60
55
50
45
40
35
30
ctrRi
klarRi
Duration of gastrulation (min)
45
40
35
30
25
20
15
10
ctrRi
klarRi

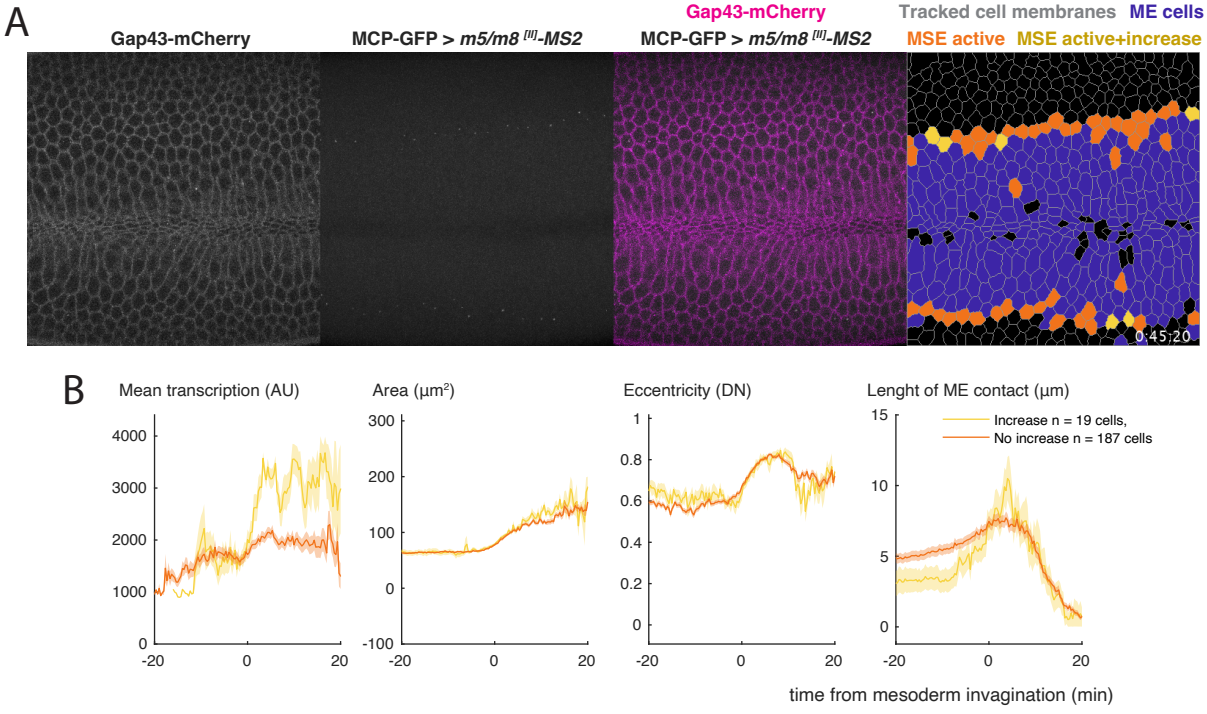
A
Gap43-mCherry
MCP-GFP > m5/m8 [II]-MS2
Gap43-mCherry
MCP-GFP > m5/m8 [II]-MS2
Tracked cell membranes
ME cells
MSE active
MSE active+increase
0:45:20
B
Mean transcription (AU)
Area (µm²)
Eccentricity (DN)
Lenght of ME contact (µm)
Increase n = 19 cells,
No increase n = 187 cells
time from mesoderm invagination (min)

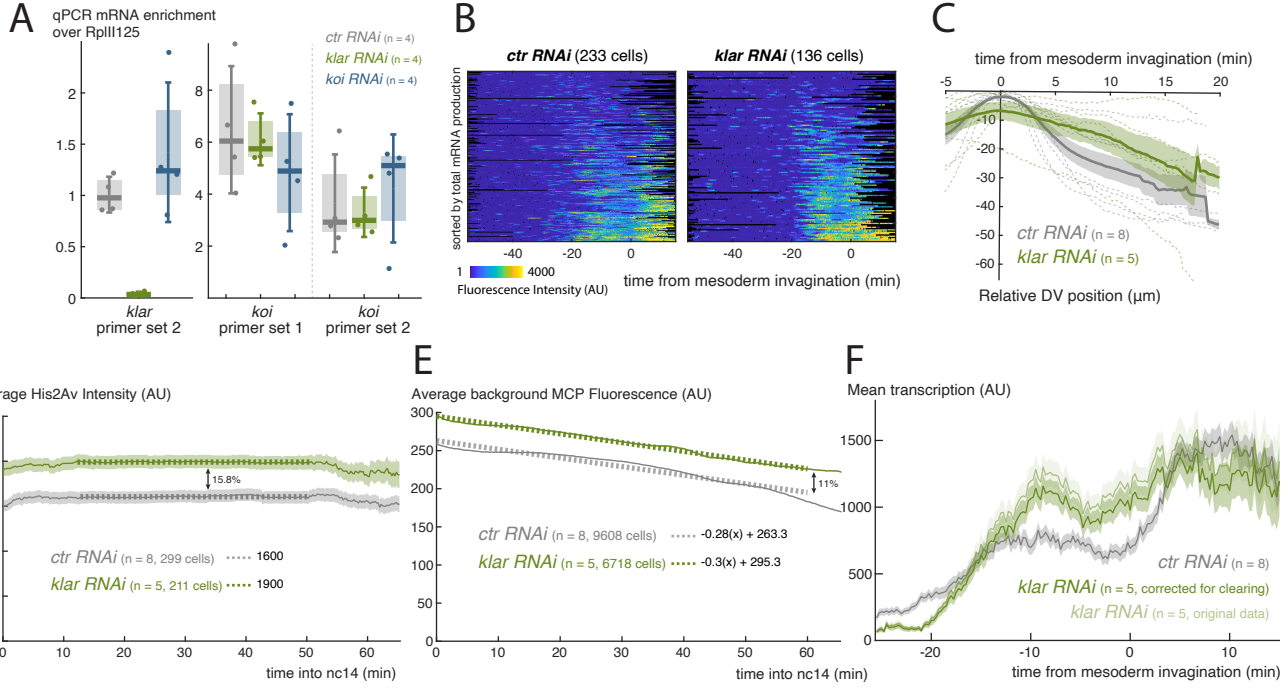
A
qPCR mRNA enrichment over RpIII125
ctr RNAi (n = 4)
klar RNAi (n = 4)
koi RNAi (n = 4)
klar primer set 2
koi primer set 1
koi primer set 2
B
ctr RNAi (233 cells)
klar RNAi (136 cells)
sorted by total mRNA production
1
4000
Fluorescence Intensity (AU)
time from mesoderm invagination (min)
C
time from mesoderm invagination (min)
ctr RNAi (n = 8)
klar RNAi (n = 5)
Relative DV position (μm)
D
Average His2Av Intensity (AU)
15.8%
ctr RNAi (n = 8, 299 cells)
1600
klar RNAi (n = 5, 211 cells)
1900
time into nc14 (min)
E
Average background MCP Fluorescence (AU)
11%
ctr RNAi (n = 8, 9608 cells)
-0.28(x) + 263.3
klar RNAi (n = 5, 6718 cells)
-0.3(x) + 295.3
time into nc14 (min)
F
Mean transcription (AU)
ctr RNAi (n = 8)
klar RNAi (n = 5, corrected for clearing)
klar RNAi (n = 5, original data)
time from mesoderm invagination (min)

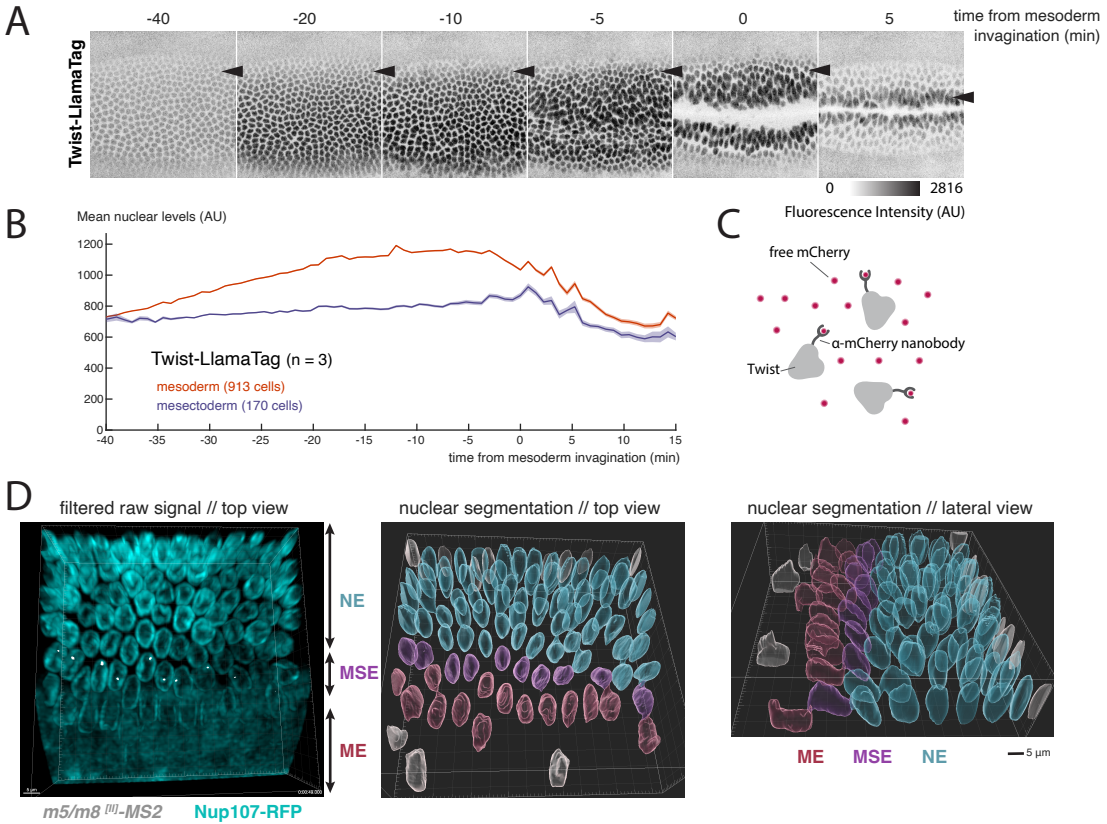
A
-40
-20
-10
-5
0
5
time from mesoderm invagination (min)
Twist-LlamaTag
0
2816
B
Mean nuclear levels (AU)
1200
1000
800
600
400
200
0
Twist-LlamaTag (n = 3)
mesoderm (913 cells)
mesectoderm (170 cells)
-40
-35
-30
-25
-20
-15
-10
-5
0
5
10
15
time from mesoderm invagination (min)
C
Fluorescence Intensity (AU)
free mCherry
α-mCherry nanobody
Twist
D
filtered raw signal // top view
nuclear segmentation // top view
nuclear segmentation // lateral view
NE
MSE
ME
ME
MSE
NE
5 µm
m5/m8 [II]-MS2
Nup107-RFP
E
Mean His2Av-RFP intensity at MS2 spot
2000
1500
1000
500
0
ctr RNAi (n = 8)
α-Cat RNAi (n = 7)
-20
-10
0
10
time from mesoderm invagination (min)
F
Mean MS2 spot movement (µm/s)
0.15
0.1
0.05
0
ctr RNAi (n = 8)
α-Cat RNAi (n = 7)
-20
-10
0
10
time from mesoderm invagination (min)

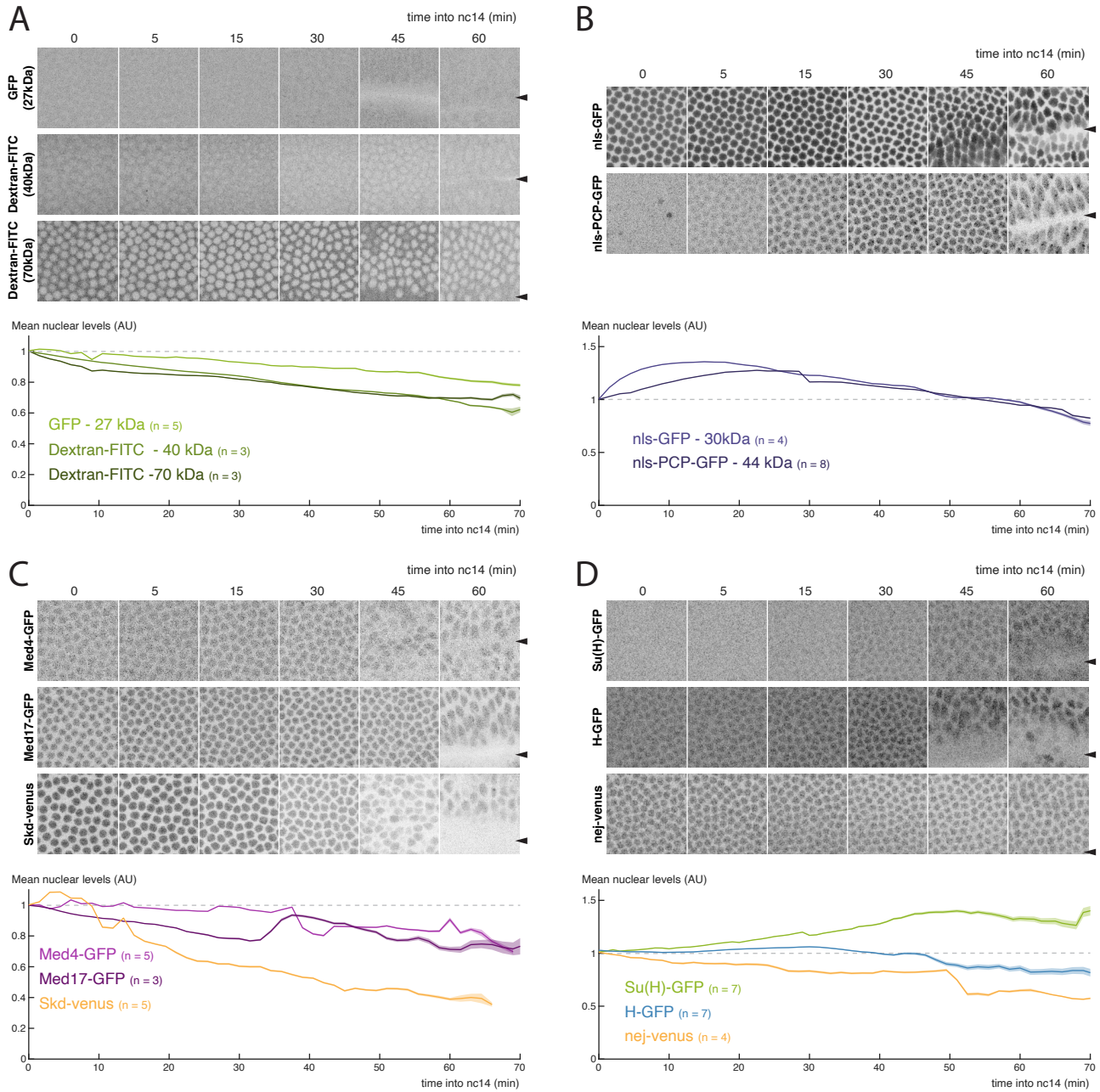
A
time into nc14 (min)
0
5
15
30
45
60
GFP (27kDa)
Dextran-FITC (40kDa)
Dextran-FITC (70kDa)
Mean nuclear levels (AU)
GFP - 27 kDa (n = 5)
Dextran-FITC - 40 kDa (n = 3)
Dextran-FITC -70 kDa (n = 3)
time into nc14 (min)
B
time into nc14 (min)
nls-GFP
nls-PCP-GFP
Mean nuclear levels (AU)
nls-GFP - 30kDa (n = 4)
nls-PCP-GFP - 44 kDa (n = 8)
time into nc14 (min)
C
time into nc14 (min)
Med4-GFP
Med17-GFP
Skd-venus
Mean nuclear levels (AU)
Med4-GFP (n = 5)
Med17-GFP (n = 3)
Skd-venus (n = 5)
time into nc14 (min)
D
time into nc14 (min)
Su(H)-GFP
H-GFP
nej-venus
Mean nuclear levels (AU)
Su(H)-GFP (n = 7)
H-GFP (n = 7)
nej-venus (n = 4)
time into nc14 (min)

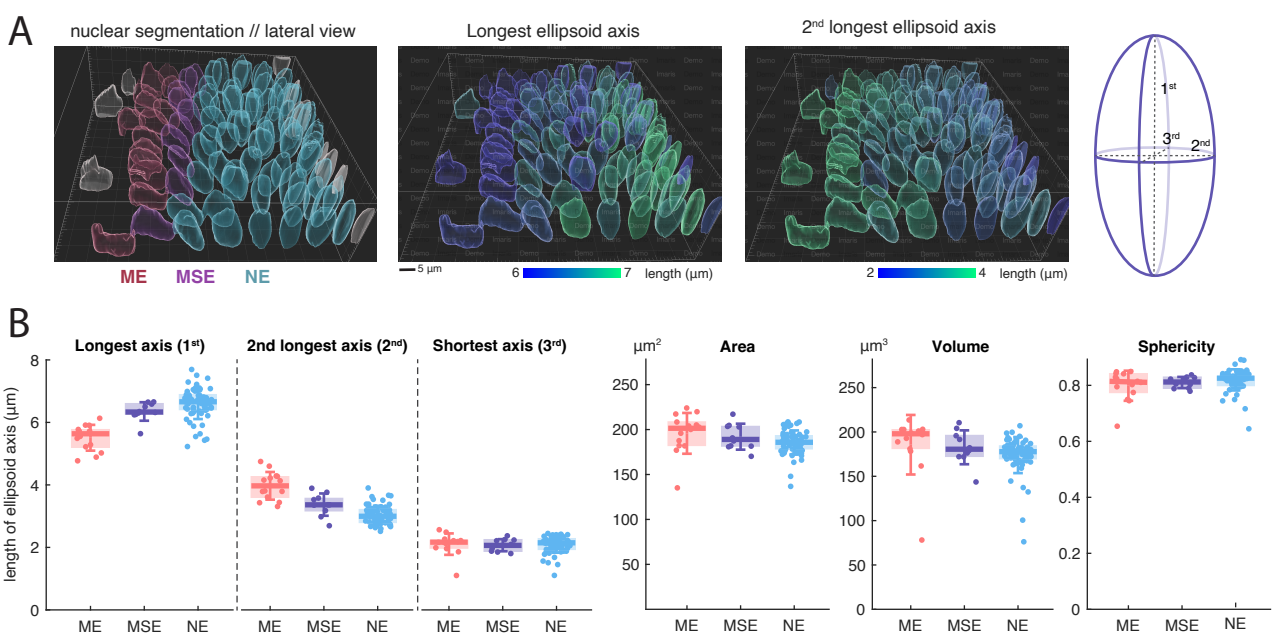
A
nuclear segmentation // lateral view
Longest ellipsoid axis
2nd longest ellipsoid axis
1st
2nd
3rd
ME
MSE
NE
5 µm
6
7
length (µm)
2
4
length (µm)
B
Longest axis (1st)
2nd longest axis (2nd)
Shortest axis (3rd)
length of ellipsoid axis (µm)
µm2
Area
µm3
Volume
Sphericity
ME
MSE
NE

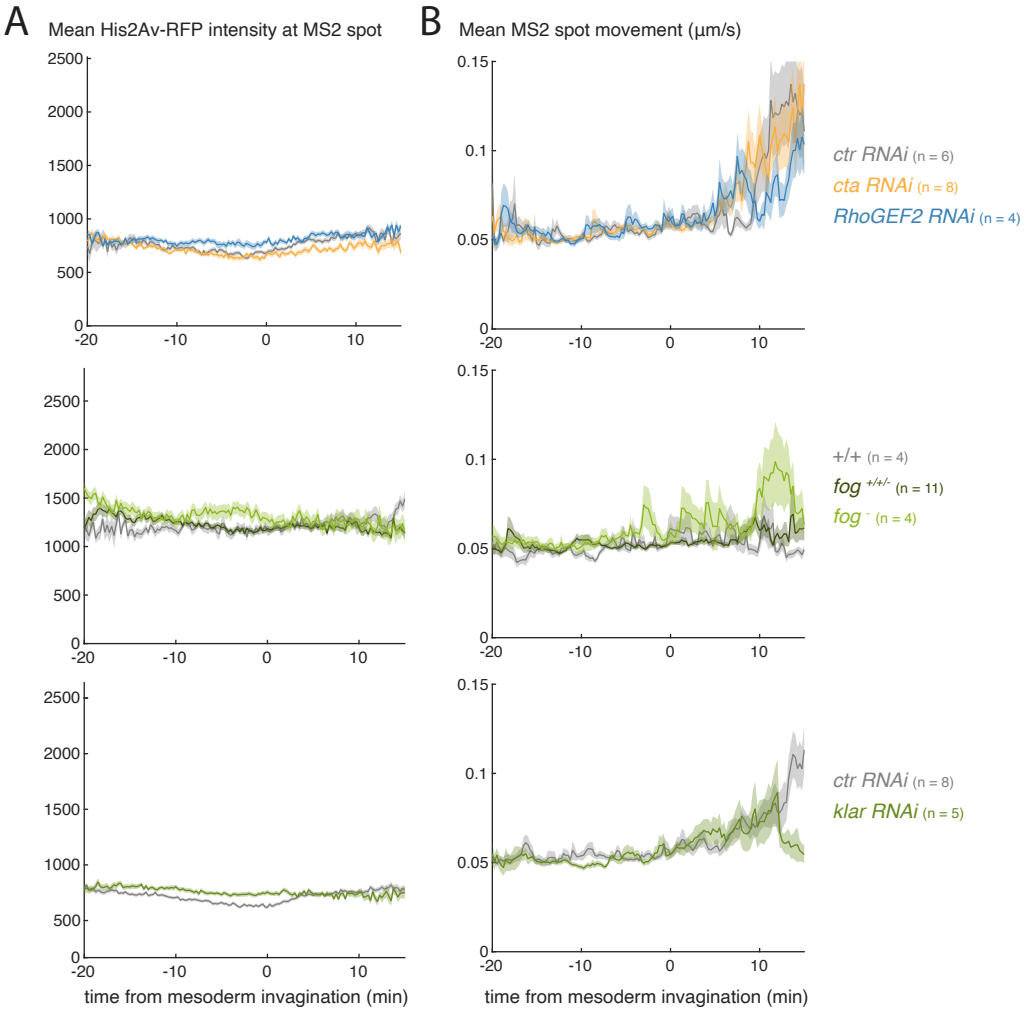
A
Mean His2Av-RFP intensity at MS2 spot
B
Mean MS2 spot movement (µm/s)
ctr RNAi (n = 6)
cta RNAi (n = 8)
RhoGEF2 RNAi (n = 4)
+/+ (n = 4)
fog +/+/- (n = 11)
fog - (n = 4)
ctr RNAi (n = 8)
klar RNAi (n = 5)
time from mesoderm invagination (min)
time from mesoderm invagination (min)